Cloud Radiative impact on Antarctic Ice Shelves

by

M. Izeboud

to obtain the degree of Master of Science
at the Delft University of Technology,
to be defended publicly on Friday March 29, 2019 at 13:00.

Student number:	4220250	
Project duration:	June 1, 2018 – March 8, 2019	
Thesis committee:	Dr. S. Lhermitte,	TU Delft, supervisor
	Dr. J.T.M. Lenaerts,	University of Colorado Boulder, supervisor
	Prof. dr. A.P. Siebesma,	TU Delft
	Dr. M. Vizcaino,	TU Delft

Cover: NASA MODIS image of Enderby Land, Antarctica (2011) by NASA Goddard Space Flight Center (USA)

An electronic version of this thesis is available at `http://repository.tudelft.nl/`.

TU Delft University of Colorado Boulder

Summary

An accurate prediction of global sea-level rise requires that the cause of recent and intensifying glacier acceleration along the Antarctic ice sheet (AIS) coastal margins is understood. Atmospheric and oceanic forcing have the potential to reduce the thickness and extent of floating ice shelves, reducing their ability to buttress the flow of outlet glaciers. Ice shelf thinning and abrupt ice shelf collapse have been linked to surface melt that is prevalent across coastal Antarctica. Primarily, surface melt is determined by the surface energy balance (SEB) which is regulated locally by clouds. Clouds regulate the amount of radiation received by the surface, with competing cloud warming and cloud cooling effects. This triggers feedback mechanisms that induce albedo changes and regulate surface melt. Local, observation based, Antarctic cloud studies on the Larsen C ice shelf have described cloud radiative effects and have linked melt events to clear skies in combination with katabatic wind regimes. However, there is yet no general assessment or quantification of the sensitivity of Antarctic ice shelf surface conditions to (seasonal) cloud forcing.

In this study the impact of seasonal cloud forcing is assessed by performing offline simulations using the snow model SNOWPACK with either all-sky atmospheric conditions or theoretical clear-sky conditions. In the latter scenario, all cloud radiative effects have been removed with the help of neural networks while keeping all other conditions (including precipitation) constant. Simulations are performed on a 1°by 1°grid covering all major ice shelves of the AIS. With satellite remote sensing cloud observations have become available for a large spatial grid, providing an AIS wide observational based dataset. These observations are incorporated in the latest regional climate model RACMO, which is needed to obtain the required high temporal resolution, to improve the modelled cloud physics. Evaluation to automatic weather stations showed that the performance of this constructed hybrid dataset is no improvement compared to the RACMO data and thus has eventually not been used. Hence, simulations performed in this study are not observations based but do provide the best possible representation of AIS conditions on the applied spatial and temporal resolution. This compliments recent improvements in the climate model.

Results show that the cloud radiative effect (CRE), defined as the difference between the net all-sky radiative budget and net clear-sky radiative budget, is positive throughout the year. This indicates a cloud warming effect, which is maximum in fall ($22.2 \pm 4.7 Wm^{-2}$) and minimum in summer ($7.1 \pm 7.7 Wm^{-2}$). The yearly average CRE is $16.5 Wm^{-2}$. Though clouds have a net radiative warming for each season there is a pronounced daily cycle that shows cloud radiative cooling ($CRE < 0$) during spring and summer daytime. This daytime cloud cooling has been shown to have a powerful impact on the surface snow conditions. Spatial variations show a stronger CRE near the coasts of the ice shelves, correlating with higher wind speeds and warmer atmospheric temperatures and thereby agreeing with previous local studies.

Surprisingly, it is shown that melt rates are lower for all-sky conditions, indicating cloud cooling effects instead of warming. This is through a non-linear response of the snow surface to the summer daytime cloud cooling, which triggers a decrease of albedo, resulting in enhanced SW absorption and increased melt rates. This feedback is stronger than the nighttime cloud warming that occurs, resulting in the average cloud cooling effect on melt rates. Not only is this non-linear response to cloud radiative forcing interesting to find, it is also a very strong effect: clear skies result on multiple ice shelves in more than tenfold the amount of liquid water mass. The enhancement of clear-sky melt is shown to be higher for ice shelves that initially have little melt for all-sky conditions. For these ice shelves, clear-sky meltwater provides an additional heat source, warming the snow and increasing its potential for further melt. The simulated values result in an average cloud effect on liquid water mass of $-23.9 \pm 10.3\ Gtyr^{-1}$, which cloud be a significant amount to cause potential hydro-fracturing and ice shelf instability during clear-sky conditions. Furthermore, the cloud radiative effect has a more direct effect on the SMB through sublimation. The seasonal cloud warming results in increased sublimation mass loss. Sublimation is relatively less sensitive to cloud radiative forcing, but as it is more consistent for each season the cloud effect on this mass component is $34.7 \pm 15.6\ Gtyr^{-1}$.

The findings in this study signify the potentially major role clouds have in future AIS conditions. A reduction in cloud cover has the potential to greatly increase the amount of meltwater and thereby ice shelf instability, or in other words clouds have a stabilizing effect on surface melt. On the other hand is the direct effect of clouds on the surface mass balance an increase of the sublimation mass loss. Either way, a better expectation of future cloud regimes is required and should be sought after.

Acknowledgements

With this report I conclude my time a as student at Delft University of Technology by presenting to you my master thesis on “The cloud radiative impact on Antarctic ice shelves”. Looking back, I am happy to finish my master Civil Engineering - Geoscience and Remote Sensing and I am grateful for all the adventures, choices and support that have led me to reach this milestone. I would like to thank my thesis supervisors, Stef and Jan, for their guidance and enthusiasm. By both allowing me to do my own research and providing critical questions and discussions when needed they have not only helped me to develop and improve this thesis but have also inspired me to continue research in this field. I especially want to thank Jan, Lineke and Norah for the amazing time in Boulder and for showing me the wonders of Colorado.

Secondly, I thank Pier and Miren for their feedback and valuable comments on my work during the completion of this thesis. I want to thank Kristof van Tricht for answering my endless questions about his method and Nander Wever for his help with SNOWPACK modelling.

Lastly, I want to appreciate my friends for distracting me, supporting me and understanding me while going through this final challenge of our student life. But mostly I thank them for the time spent not-studying. My parents and sister have always been there for me, and I know they are proud of me. I want to show my gratitude for their unconditional support and their invaluable advice that always kept me close to myself. Let the rest of my life begin!

M. Izeboud
Delft, March 2019

Contents

List of Figures

List of Tables

List of Abbreviations

AIS Antarctic ice sheet.

AS all-sky.

AWS automatic weather station.

CC cold content.

CF cloud enhancement factor.

CRE cloud radiative effect.

CS clear-sky.

CSC CloudSat-CALIPSO.

DJF December, January, February.

GrIS Greenland ice sheet.

IWP ice water path.

JJA June, July, August.

LH latent heat.

liqW liquid water.

LW long wave.

LWP liquid water path.

MAM March, April, May.

NN neural network.

RACMO Regional Atmospheric Climate Model.

RMSE root mean squared error.

SEB surface energy balance.

SH sensible heat.

SMB surface mass balance.

SON September, October, November.

SW short wave.

1 Introduction

1.1. The Antarctic Ice Sheet

1.1.1. Indicator for Climate Change

The global climate has changed relative to the pre-industrial period, with lasting impacts on organisms, ecosystems as well as human systems and well-being [Hoegh-Guldbergand et al., 2018, p.177]. Sea-level rise is an important consequence of global climate warming with potentially very large impacts for the human population [IPCC, 2007, 2014, Vellinga and Leatherman, 1989]. The global mean sea level has been rising throughout the 20th century (sea level rose by 0.19 ± 0.02 m from 1901-2010), with an accelerated rate to the end of this period which is expected to increase further [Clark et al., 2016, IPCC, 2014, Levermann et al., 2013]. The contribution of glacier and ice sheet mass loss together with ocean thermal expansion causes about 75% of the observed global mean sea level rise to present day [IPCC, 2014, p.56]. Current predictions are that by 2100 the global mean sea level will have reached approximately half a meter [Rasmussen et al., 2018]. One of the key reasons the future sea level rise remains uncertain is the role of the Greenland and Antarctic ice sheets, as contributions from only the latter could already come down to one meter by 2100 [DeConto and Pollard, 2016].

The Antarctic ice sheet (AIS) is an important driver of sea-level rise. Ice losses from Antarctica have tripled since 2012, according to the IMBIE assessment in 2018, a joint study from NASA and ESA [The IMBIE team, 2018]. Antarctica's potential contribution to global sea level rise from its land-held ice is almost 7.5 times greater than all other sources of land-held ice in the world combined: the ice sheet holds enough water to raise global sea level by 58 meter [Fretwell et al., 2013]. Understanding how Antarctica loses ice, and how much, is crucial to understanding the impacts of climate change. However, not all processes that influence the AIS are resolved.

1.1.2. Surface Mass and Energy Balance of Antarctic Ice Sheet

Current mass loss of the AIS is mainly a result from acceleration of outlet glaciers and a disintegration of ice shelves [Bindschadler et al., 2011, Pritchard et al., 2012, Vaughan et al., 2013]. Ice shelves help to buttress and restrain flow of the grounded ice, and recent ice-shelf collapse led to retreat and acceleration of several glaciers on the Antarctic Peninsula [Glasser and Scambos, 2008, Scambos et al., 2004]. Thinning and retreat of ice shelves governs the current change of the AIS, but the extend and magnitude of ice-shelf thickness change remain poorly understood and as a result its future impact on the ice sheets is not predicted very well [Holland et al., 2011, Pritchard et al., 2012].

Ice shelf thinning [Holland et al., 2011], outlet glacier dynamics [Miles et al., 2013, Pritchard and Vaughan, 2007], and abrupt ice shelf collapse [Scambos et al., 2000, Van den Broeke, 2005] have all been linked to surface melt that is prevalent across coastal Antarctica [Trusel et al., 2012], which responds to changes in atmospheric conditions. Deciphering surface melt magnitudes and impacts mandates a robust understanding of its dynamics across space and time.

In order to understand the coupling between ice-shelf degradation and atmospheric changes, understanding the contributing factors to surface firn and ice conditions (and subsequently melt rates) is a primary concern. Previous researches agree that observed atmospheric warming [Chapman and Walsh,

2007, Marshall et al., 2006] is a driver to ice-shelf degradation. But primarily, surface melt is determined by the surface energy balance (SEB), the sum of incoming and outgoing energy fluxes at the surface. Differences in the seasonal cycle of the SEB at Antarctica are attributed to different wind climates in combination with overcast or clear-sky conditions [Van Den Broeke et al., 2005].

Generally, clouds are known to play a pivotal role in regulating the local SEB, with competing warming and cooling effects [Curry et al., 1996, Ramanathan et al., 1989, Shupe and Intrieri, 2004]. Arctic clouds trigger feedback mechanisms that induce albedo changes and regulate surface melt principally, because clouds regulate the amount of radiation received by the surface [Bintanja and Van den Broeke, 1996]. However, confidence in the current representation of processes involving clouds an aerosols by models is low [Bony et al., 2006, IPCC, 2014, p.56].

1.1.3. Influence of Clouds on the Surface Energy Balance

Clouds generally limit the daytime surface energy excess by blocking short wave (SW) radiation (cloud cooling effect) or limit nocturnal cooling of the ice by enhanced reflections of long wave (LW) radiation to the surface (cloud warming effect). The dependence of SW and LW radiative surface fluxes on cloud coverage is found to depend chiefly on the cloud microphyscis (temperature, height, emissivity, phase), in addition to the values of the surface albedo and solar zenith angle [Bintanja and Van den Broeke, 1996, Curry et al., 1996, Shupe and Intrieri, 2004, Turner et al., 2007].

Uncertainties in whether clouds induce net radiative warming or cooling remain, firstly due to the uncertain representation of cloud macro- and microphysics in (regional) climate models [Bony et al., 2006, Turner et al., 2007] and secondly due to uncertainties in the feedback response of the snow/ice surface [Kuipers Munneke et al., 2011]. The surface feedbacks have been shown to be of significant influence [Hofer et al., 2017, Kuipers Munneke et al., 2012, Van Den Broeke et al., 2004, Van den Broeke et al., 2006, Van Tricht et al., 2016b]. Possible impacts of cloud radiation on the surface firn conditions is for example a reduction of meltwater refreezing, thereby accelerating bare-ice exposure, decreasing the albedo and enhancing meltwater runoff (determined on the Greenland ice sheet (GrIS) [Van Tricht et al., 2016b]). Contrastingly, clouds reduce downwelling SW radiation, increase the surface albedo and reduce melt. Despite their importance, the precise impact of clouds on the SEB and consequently the surface mass balance (SMB) are poorly understood, especially yet for the AIS.

1.2. Current Methods and Limitations

The distribution of clouds and their precise impact on the SEB and consequently the surface mass balance (SMB) are poorly understood, due to the limited availability of measurements. Studies that are based on observations with automatic weather station (AWS) are limited in spatial coverage, they do not always cover the complete seasonal cycle and do not always incorporate the surface feedbacks. Kuipers Munneke et al. [2012] analysed the summer SEB with observations limited to the Larsen C ice shelf, including a surface model; Van Den Broeke et al. [2005] and Van den Broeke et al. [2006] cover four major regions of the AIS using four weather stations (to determine the daily and seasonal SEB and the influence of clouds) - resulting in an ice sheet wide assessment with very poor resolution, and without surface feedback processes. Bintanja and Van den Broeke [1996] cover four locations spread over both the GrIS and the AIS to determine cloud influence on the SEB, without including surface feedback processes. Conclusively, there is a need to combine all these components for an AIS wide assessment and quantification of cloud radiative effects and their impacts on the SEB and the SMB.

Ice sheet wide (cloud) studies resort to regional climate models, which do incorporate ice and snow processes, but they show large uncertainties in cloud representation. Matus and L'Ecuyer [2017] and Lenaerts et al. [2017] show that the reanalyses climate models typically exhibit significant biases in the simulation of clouds and radiation in the polar regions, and that they disagree widely on the amount of cloud liquid and ice.

Remote sensing technologies have improved our ability to gather cloud observations with higher spatial coverage greatly, mainly with the launch of CloudSat-CALIPSO (CSC) which has a very high resolution in observing cloud properties. However, satellite observations have low temporal resolution and they do not include the sensitivity of the AIS to radiation.

Recently a state-of-the art method was constructed by Van Tricht et al. [2016b] to overcome said problems as much as possible. They combined an atmospheric model with satellite observations at the GrIS to create a hybrid dataset with high spatial coverage and a reduced uncertainty in cloud properties. With this

atmospheric dataset, a snow model can be used to simulate the response of the ice to the forcing. This method provides a workable solution to study both a large spatial area at a high temporal resolution and include cloud observational data. The snow model SNOWPACK [Lehning et al., 2002b] is a sophisticated tool that enables offline simulations with different forcing and is therefore especially suited to study different radiation regimes.

1.3. Research Questions

To strive for a better understanding of the radiative impact of clouds on the conditions of the Antarctic Ice Sheet with a wide spatial coverage, i.e. to better understand the coupling of the cloud radiative effect (CRE) on the SEB to the SMB, the following research question was formulated of this study:

> **What is the cloud radiative effect on the firn conditions and surface mass balance components of Antarctic ice shelves, through the surface energy balance?**

The CRE is defined as the difference between an all-sky scenario that best represents the conditions on the ice shelves and a clear-sky scenario in which all cloud radiative effects are removed. The focus is limited to ice shelves because they are a) the most vulnerable part of the AIS and more sensitive to atmospheric forcing and b) Antarctic mass loss occurs mainly as a result of ice shelf disintegration. Therefore, the drivers of change on ice shelves need to be understood to improve predictions of the AIS in future climate scenarios. An inter-comparison of the ice shelves can potentially reveal the importance of cloud impact with respect to other characteristics that differ for each ice shelf and are not easily resolved for a high spatial resolution with the few available automatic weather stations (such as differences in air temperature, general cloud cover frequency, katabatic winds, etc). It will also shed light on sensitivity of the ice shelves to cloud radiative forcing.

As well as this spatial analysis of sensitivity to cloud radiative forcing, the temporal variability is of interest, as cloud warming and cloud cooling effects are related to the daily and seasonal radiation cycles. The timing and reason for a change from cloud warming to cloud cooling, or vice versa, needs to be determined and coupled to the ice sheet surface properties which is why a high temporal resolution is required. This will improve expectations on what to expect for changing atmospheric conditions.

The main research question can be divided in the following partitions:

1. How strong is the CRE on the Antarctic ice shelves and what is its seasonal variability?
2. What are feedback processes within the firn as response to the CRE?
3. What is the spatial variability of cloud radiative forcing and do ice shelves show different responses?

To this end, the method of Van Tricht et al. [2016b] is applied: high spatial and temporal resolution simulations are performed for different cloud radiative scenarios. The major ice shelves that are included are: the Ross and Filchner-Ronne ice shelves, the Larsen C and Wilkins & George VI ice shelves on the Antarctic Peninsula, the Riiser-Larsen and Fimbull ice shelves near Dronning Maud Land and the Amery, West and Shackleton ice shelves in East Antarctica, see Figure 1.1. Ice shelves in West Antarctica are not included mainly due to their relatively smaller size and because they are subject to fast out-flowing glaciers and oceanic basal warming, overshadowing atmospheric influences [Pritchard et al., 2012].

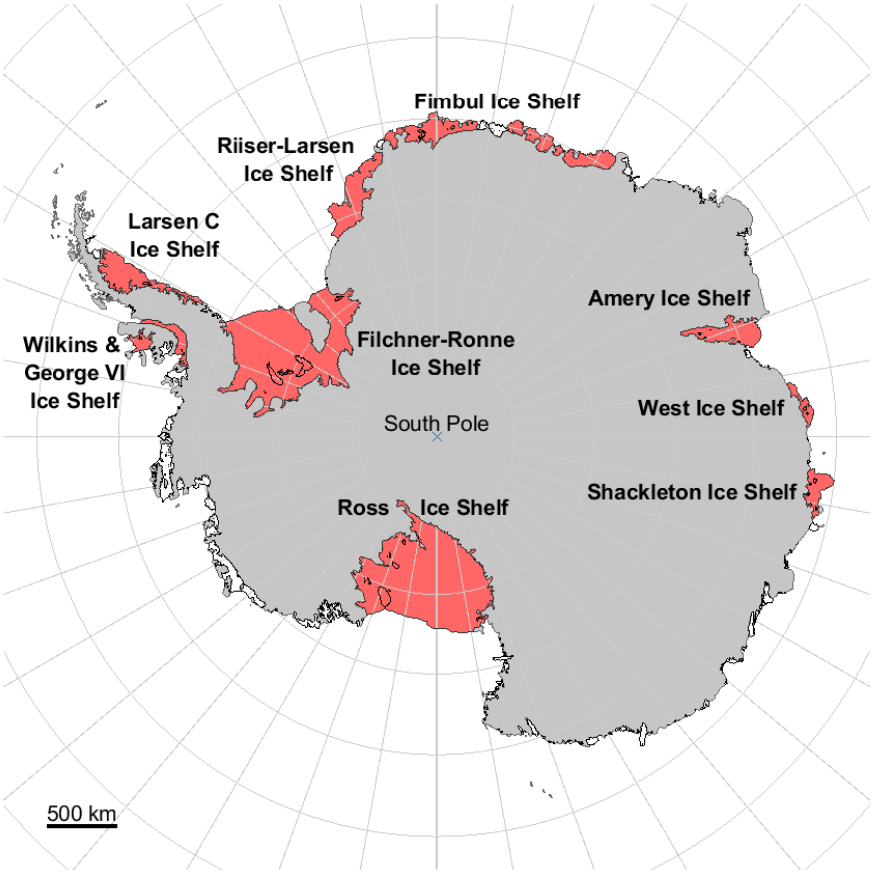

Figure 1.1: All major ice shelves that are accounted for in this study. Figure created with Matlab Antarctic Mapping Toolbox [Greene et al., 2017]

2

Background and Theory

This chapter provides information that is important to understand processes on the Antarctic ice shelves accompanied with relevant previous research. Furthermore, background information is provided on components of the method that is applied in this study. As a result, this chapter is not so much a continuous storyline but more like a patchwork of information.

2.1. Understanding the Antarctic Ice Sheet

2.1.1. Ice shelf vulnerability

Current mass loss of the AIS is mainly a result from acceleration of outlet glaciers and a disintegration of ice shelves [Bindschadler et al., 2011, Pritchard et al., 2012, Vaughan et al., 2013]. Antarctic ice shelves make up almost half of the Antarctic coast line (44%) and over 80% of Antarctica's grounded ice drains through the ice shelves [Pritchard et al., 2012]. Ice shelves help to buttress and restrain flow of the grounded ice. Recent ice shelf collapse has led to retreat and acceleration of several glaciers on the Antarctic Peninsula [Glasser and Scambos, 2008, Scambos et al., 2004].

At the surface, ice shelves are vulnerable to changes in atmospheric conditions and at their bases they are exposed to heat transported through the ocean [Fricker and Padman, 2012, Pritchard et al., 2012, Scambos et al., 2000]. Because of this, ice shelves respond more quickly than ice sheets or glaciers to rising temperatures.

Ice shelves in West Antarctica are currently thinning at a faster rate due to the warmer ocean water below [Pritchard et al., 2012]. Around the Antarctic Peninsula, the reduction in ice-shelf extent has been ongoing for several decades [Cook and Vaughan, 2010, Fricker and Padman, 2012], but here it is mostly attributed to changing atmospheric temperatures [Marshall et al., 2006, Scambos et al., 2000]. While many of the larger ice shelves, and ice shelves in East Antarctica, are thought to exhibit more stable conditions [Gardner et al., 2018, King et al., Shepherd et al., 2010], Miles et al. [2013] have observed changes in outlet glaciers consistent with changes in air temperature, and recent NASA ice velocity maps show that more glaciers in East Antarctica have begun to lose ice over the past decade [NASA's Earth Sciences News Team, 2018], illustrating that these stable conditions might start to change with our changing climate.

The Antarctic Ice Sheet SMB is shown by The IMBIE team [2018] to have lost $2,720 \pm 1,390$ billion tonnes of ice between 1992 and 2017, which corresponds to an increase in mean sea level of 7.6 ± 3.9 millimetres. Over this period, ocean-driven melting has caused rates of ice loss from West Antarctica to increase from 53 ± 29 billion to 159 ± 26 billion tonnes per year; ice-shelf collapse has increased the rate of ice loss from the Antarctic Peninsula from 7 ± 13 billion to 33 ± 16 billion tonnes per year.

2.1.2. Surface melt

Ice shelf thinning [Holland et al., 2011], outlet glacier dynamics [Miles et al., 2013, Pritchard and Vaughan, 2007], and abrupt ice shelf collapse [Scambos et al., 2000, Van den Broeke, 2005] have all been linked to surface melt that is prevalent across coastal Antarctica [Trusel et al., 2012].

On the Antarctic Peninsula (AP), melt-season duration and extend of meltwater ponding have increased due to atmospheric changes. Longer melt-seasons and increased meltwater ponding on the Antarctic

Peninsula coincided with more (frequent) break-up events, whereas areas lacking pond formation were relatively unchanged [Luckman et al., 2012, Scambos et al., 2000]. Summer melt percolation and changes in the stress field due to ice shelf collapse play a major role in glacier dynamics. It also has a coupled role in the Antarctic cryosphere by warming the ice [Phillips et al., 2010], also changing stress fields of the ice, enhancing hydro-fracturing and potentially the propagation of surface crevasses. Conclusively, meltwater has a serious potential to influence mass loss [Luckman et al., 2012, Scambos et al., 2004, Van den Broeke, 2005]. Deciphering surface melt magnitudes and impacts mandates a robust understanding of its dynamics across space and time. For this reason, the driving factors of the surface energy balance, providing energy for melt, are to be understood.

2.2. Cloud Microphysics, Radiation and the Surface Energy Balance

2.2.1. Surface Energy Balance of Antarctic Ice Sheet

The surface energy balance describes the excess energy available for surface melt after all the energy sources and sinks are accounted for. The SEB (Wm^{-2}) is defined as

$$E_M = SW_{in} - SW_{out} + LW_{in} - LW_{out} + SH + LH + G_S, \tag{2.1}$$

in which E_M is the melt energy, SW and LW are net radiative fluxes (incoming and outgoing), SH and LH are the sensible and latent turbulent heat fluxes and G_S is the subsurface heat flux.

Absorbed short wave radiation drives the daily cycle of the SEB, in spite of the high surface albedo (0.84–0.88) at the ice sheet. The dominant heat sink is the cooling by long wave radiation, but this flux is distributed more evenly throughout the day, so that a pronounced daily cycle in net all-wave radiation remains. During the night, heat is re-supplied to the snow surface by the sub-surface heat flux and sensible heat flux, especially in the katabatic wind zone. Daytime radiative energy excess is removed from the surface by sublimation, melt and sub-surface heat transport [Van den Broeke et al., 2006].

Over the AIS the annual mean net radiation is negative. During the short summer, the net radiation budget becomes slightly positive. This positive net radiative flux is compensated by melt and turbulent diffusion of heat and moisture, leading to sublimation and weak convection over the ice shelf [Kuipers Munneke et al., 2012], and otherwise a sub-surface heat transport [Van den Broeke et al., 2006]. In winter, longwave cooling of the surface is compensated by a downward turbulent transport of sensible heat.

Spatial differences in the SEB are largely controlled by differences in cloud cover and wind climates [Van Den Broeke et al., 2005, Van den Broeke et al., 2006]. In the katabatic wind zone, a combination of clear skies and strong winds forces a large wintertime turbulent transport of sensible heat towards the surface, which in turn enhances the longwave radiative heat loss. On the coastal ice shelf and on the plateau, strong winds are associated with overcast conditions, limiting the radiative heat loss and sensible heat exchange [Van Den Broeke et al., 2005].

2.2.2. Influence of Clouds on the Surface Energy Balance

Clouds are known to play an essential role in regulating the local SEB, with competing warming and cooling effects [Curry et al., 1996, Ramanathan et al., 1989, Shupe and Intrieri, 2004]. The dependence of shortwave and longwave radiative surface fluxes on cloud coverage depends chiefly on the cloud microphyscis (temperature, height, emissivity, phase), in addition to the values of the surface albedo and solar zenith angle [Bintanja and Van den Broeke, 1996, Curry et al., 1996, Shupe and Intrieri, 2004, Turner et al., 2007].

Ice clouds are relatively more transparent to SW radiation compared to liquid clouds, because the particles are larger in diameter and fewer in number. Liquid clouds are generally warmer and contain more particles than ice clouds, emitting relatively more LW radiation. In addition to this, the vertical profile of the cloud (or optical depth) and the mixing of the phases determine flux divergence in clouds [Gilbert, 2018, Turner et al., 2007]. In the Arctic, liquid-containing cloud scenes dominate both LW and SW radiative impacts. Overall, low-level stratiform liquid and mixed-phase clouds are found to be the most important contributors to the Arctic surface radiation balance [Shupe and Intrieri, 2004].

Snow aging causes reflectance to vary significantly on timescales of days. This variability influences the strength of snow albedo feedback and can affect the timing of snow melt. Increased incoming SW radiation for clear skies results in relatively warmer snow, which enhances outgoing LW radiation and promotes snow metamorphism, lowering the albedo of the snowpack and enhancing SW absorption (also depending on the sun elevation) [Flanner and Zender, 2006, Shupe and Intrieri, 2004]. Whereas for cloudy conditions multiple

reflections of SW radiation between clouds and the surface generally increase the albedo [Van Den Broeke et al., 2005], decreasing SW absorption.

More specific, downwelling LW and SW radiation can be described by Equations 2.2 and 2.3 [Anthes et al., 1987, Unsworth and Monteith, 1975]. In Equation 2.2, $LW\downarrow$ is the downwelling LW radiation, ϵ is the atmospheric emissivity and T the temperature (K) at a reference height and σ the Stefan-Boltzmann constant ($\sigma = 5.670 \times 10^{-8} Wm^{-2}K^{-4}$). In equation 2.3, S_0 is the solar constant (1362 Wm^{-2}), α the surface albedo (-), τ the shortwave transmissivity (-) and ζ the solar zenith angle (°).

$$LW\downarrow = \epsilon\sigma T^4 \tag{2.2}$$

$$SW\downarrow = S_0\tau cos(\zeta) \tag{2.3}$$

The surface LW radiation is primarily a function of cloud temperature, cloud height and emissivity. Emissivity is mainly determined by the cloud microphysical properties such as phase partitioning: the liquid water and ice content or liquid water path (LWP) and ice water path (IWP). The surface SW radiation depends on cloud microphysical properties (IWP and LWP), surface albedo and solar zenith angle. These properties determine if the dominating cloud effect is either radiative warming or cooling.

Clouds generally limit the daytime energy excess by blocking SW radiation (cloud cooling effect) or limit nocturnal cooling of the ice by enhanced reflections of LW radiation (cloud warming effect). The cloud radiative effect (CRE, Wm^{-2}) is defined as the difference in the surface net radiation budget of an all-sky scenario compared to a clear-sky scenario, defined in Equation 2.4. A positive CRE indicates net cloud warming at the surface; a negative CRE indicates net cloud cooling.

$$CRE = (SW_{net} + LW_{net})_{all-sky} - (SW_{net} + LW_{net})_{clear-sky} \tag{2.4}$$

The CRE varies throughout the day and the seasons, following the cycles of LW and SW radiation [Van Tricht et al., 2016b, Wang et al., 2018]. The annual cycle of Arctic cloud forcing reveals cloud warming through most of the year and a short period of surface cooling in the middle of summer [Hofer et al., 2017, Shupe and Intrieri, 2004].

The net radiation budget is found to increase with cloud coverage (a positive CRE) by observations across the GrIS and AIS [Bintanja and Van den Broeke, 1996], depending on location. Furthermore, the CRE is observed to vary both spatially and seasonally on the GrIS by Wang et al. [2018], with both cloud warming and cooling effects. Bintanja and Van den Broeke [1996] demonstrate that this is due mainly to the fact that the shortwave cloud transmissivity at polar sites is relatively high, which, in turn, is thought to be caused mainly by a low cloud optical thickness and by multiple scattering between surface and cloud-base. Van Tricht et al. [2016b] also showed that, over the Greenland ice sheet, the increase in LW radiation due to clouds dominates the decrease in SW radiation on annual time scales. Izeboud et al. and Van Tricht et al. [2016b] argue that a positive CRE affects the conditions of the GrIS firn, reducing meltwater refreezing and thereby accelerating bare-ice exposure (decreasing the albedo) and enhancing meltwater runoff. However, Hofer et al. [2017] argue that observed decreasing summer cloud cover, i.e. a relative increase in SW radiation (corresponding to a cloud cooling effect), increased the meltwater runoff on the Greenland ice sheet. This discussion gives an example of the complexity of cloud radiative impacts.

Kuipers Munneke et al. [2012] have observed that on the Larsen C ice shelf, under warm and sunny conditions (result of a dry and warm föhn wind) the increase in shortwave and sensible heat fluxes was larger than the decrease of net longwave and latent heat fluxes, providing energy for significant melt. On ice shelves in Dronning Maud land, observations show that clouds limit atmospheric transmissivity for shortwave radiation but also strongly enhance the albedo for the SW radiation that reaches the surface, which is why less radiation (65%) is absorbed relatively to less-cloudy inland areas [Van Den Broeke et al., 2004]; i.e. a cloud cloud cooling effect.

2.3. Remote Sensing of Clouds with CloudSat-CALIPSO

Among the largest uncertainties in quantifying the radiative impacts of clouds are those that arise from the inherent difficulty in precisely specifying the vertical distribution of cloud optical properties using passive satellite measurements [L'Ecuyer et al., 2008]. The launch of CloudSat and Cloud–Aerosol Lidar and Infrared Pathfinder Satellite Observations (CALIPSO) in 2006 provided the first opportunity to retrieve profiles of liquid and ice cloud microphysical properties [Henderson et al., 2013].

CloudSat and CALIPSO (CSC) fly in The Afternoon Train or 'A-Train' satellite formation. The A-Train provides coordinated science observations of the Earth and its atmosphere. The CloudSat and CALIPSO satellites [Stephens et al., 2002, Winker et al., 2009] have significantly improved our ability to quantify vertical profiles of cloud occurrence and water content [Boucher et al., 2013, p.579], with their co-located and combined observations.

The purpose of the CloudSat mission was to measure the vertical structure of clouds from space, for the first time using a millimeter wavelength cloud radar. Retrieved profiles of liquid and ice cloud microphysical properties from this Cloud Profiling Radar (CPR) form the basis of the CloudSat's fluxes and heating rates algorithm, 2B-FLXHR, a standard product that provides high vertical resolution profiles of radiative fluxes and atmospheric heating rates on the global scale. CloudSat observations have been used to improve on our ability to predict where and why clouds and precipitation form, to learn how much water condenses in clouds, and to gain a better understanding of how the water cycle works [CloudSat DPC].

The primary CloudSat instrument is a 94-GHz, nadir-pointing, CPR which measures the power backscattered by clouds as a function of distance from the radar. See Table 2.1 for specific characteristics. The overall design of the CPR is simple, well understood, and has strong heritage from many cloud radars already in operation in ground-based and airborne applications [Cooperative Institute for Research in the Atmosphere, 2008]. It is a first-of-a-kind satellite-based radar system, equipped with a millimeter-wavelength cloud radar; a radar that is more than 1000 times more sensitive than existing weather radars. Unlike ground-based weather radars that use centimeter wavelengths to detect raindrop-sized particles, CloudSat's radar is able to detect the much smaller particles of liquid water and ice that constitute the large cloud masses.

CALIPSO provides a unique perspective on the amount, height, phase and type of aerosols and thin clouds. CALIOP, Cloud-Aerosol Lidar with Orthogonal Polarization, is a two-wavelength polarization-sensitive lidar that provides high-resolution vertical profiles of aerosols and clouds [Winker et al., 2009]. See Table 2.1 for specific characteristics. Observations from CALIPSO are, for example, used to observe the vertical layering of clouds and aerosols with a high level of detail and to study where thin clouds occur and why, how they form and how they affect the climate [CloudSat DPC].

The formation of CloudSat with CALIPSO is such that the lidar footprint trails the radar footprint by approximately 15 seconds and the radar and lidar footprints are offset in the cross-track direction by no more than 2 km. As a result, observations are at near-same time. The combined product of CloudSat's CPR and CALIPSO's CALIOP, known as 2B-FLXHR-LIDAR, provides a nearly complete depiction of the cloud and aerosol properties that are essential for deriving high vertical resolution profiles of LW and SW radiative fluxes and heating rates throughout the atmosphere [Henderson et al., 2013]. The product significantly reduces errors for CloudSat's flux estimates that were caused by the poor detection of thin high clouds and low clouds by the CPR [L'Ecuyer et al., 2008]. The method used to retrieve the broadband radiative fluxes from the component multisensor cloud and aerosol properties is described in Henderson et al. [2013]. The output is constructed using vertical distributions of liquid and ice cloud effective radii and water contents, ancillary temperature and humidity profiles from the ECMWF analysis and surface albedo and emissivity data from the International geosphere-Biosphere Programme global land surface classification. Reflectance, transmission and radiative characteristics are then described with a broadband radiative flux model, BugsRad, inlcuding molecular scattering, gaseous absorption and absorption and scattering by both liquid and ice.

A modified version of release 04 (R04) of the 2B-FLXHR-LIDAR product has been constructed with specific adaptations for the polar atmosphere by Van Tricht et al. [2016a], including diagnostic integrated cloud ice and water content. The performance of this product over polar regions has been positively evaluated by statistical comparison with AWS measurements both in the Arctic as well as in the Antarctic [Van Tricht et al., 2016a,b] and for release 05 these adaptions will be incorporated in the standard product.

CloudSat		
CPR nadir-looking radar		
nominal frequency	94	GHz
nadir angle	0.16	deg
vertical resolution	240	m
antenna size	1.85	m
footprint	1.4 x 1.7	km
sample freq	625	Hz
Pulse Repetition Frequency	4300	Hz
Burst rate	0.16	sec/burst
CALIPSO		
CALIOP two-wavelength polarization-sensitive lidar		
wavelengths	532;1064	nm
pulse energy	110	mJ/channel
polarization	532	nm
vertical resolution	30-60	m
receiver telescope diameter	1	m
footprint	100/130	m/μrad
CloudSat-Calipso		
timelag between satellites	15	sec
along-track velocity	7	km/sec
inclination angle	89	$\circ$
altitude	750	km

Table 2.1: Summary of characteristics CloudSat CPR and CALIPSO CALIOP. Obtained from `https://www-calipso.larc.nasa.gov/about/atrain.php` (12 January 2019)

2.4. The Regional Climate model RACMO2.4

The Regional Atmospheric Climate Model (RACMO), version 2, combines the hydrostatic dynamical core of the High Resolution Limited Area Model (HIRLAM) with the physics package of the European Centre for Medium-range Weather Forecasts (ECMWF) Integrated Forecast System. RACMO2 has been specifically adapted for use over the Antarctic continent, by using a multilayer snow model [Ettema et al., 2010] that calculates melt, refreezing, percolation and run-off of meltwater, uses a prognostic scheme that calculates surface albedo [Kuipers Munneke et al., 2011] and incorporates a drifting snow routine [Lenaerts et al., 2012].

In recent years, the RACMO2 model version has made significant progress and improvements. Since RACMO2.1, RACMO2.3 (2014) contained several improvements in the representation of atmospheric physics to reduce significant biases in radiation and snowfall values [King et al., 2015, Van Wessem et al., 2014]. In particular, changes were introduced in the cloud scheme, which newly included a new ice super-saturation parameterisation, improving the representation of supercooled liquid-bearing clouds and also in the turbulence and radiation parameterisation schemes. Since, further progress has been made to reduce discrepancies in SEB and SMB properties, which have been attributed to shortcomings in the cloud microphysics (simulating too-thin clouds with too little snowfall, too little downwelling LW and too much downwelling SW radiation), that has been related to an unrealistic partitioning of ice and water content in these clouds [King et al., 2015, Van Wessem et al., 2014, 2018]. Updates are implemented in a new RACMO2.3p2 version (2018), also referred to as RACMO2.4.

Updates for RACMO2.4 included additional upper-air relaxation by ERA-Interim reanalyses data, a revised topography, tuned parameters in the cloud scheme that generate more precipitation towards the AIS interior and modified snow properties reducing drifting snow sublimation and increasing simulated surface snowmelt. The critical cloud water and cloud ice content threshold has been increased; leading to both ice and water clouds lasting longer in the atmosphere before precipitating. A significant improvement in simulated SEB and SMB over the ice sheet is found, in particular at lower elevations. However, even though the simulation of the radiative fluxes has improved at the surface, RACMO2.4 still considerably overestimates cloud ice and cloud water (up to a bias of 18 gm^{-2} for IWP and 60 gm^{-2} for LWP). This remaining bias suggests that compensating errors exist due to a cloud radiation scheme that is not active enough [Van Wessem et al., 2018].

2.5. Shallow Neural Networks

Artificial neural networks are computing systems inspired by the processing of the brain as a basis to develop algorithms. The neural network itself is not an algorithm, but rather a framework for many different machine learning algorithms to work together and process complex data inputs. A shallow neural network (NN) is used to fit data. The neural network approximates a function between a set of input variables and a corresponding set of output variables [Heaton, 2008]. The NN starts out blank with an input layer, hidden layer and output layer. The layers are composed of simple nodes that operate in parallel. The connections between the nodes are weights that will determine the network function. See Figure 2.1 for a schematic representation of the neural network structure used in this study.

During training, the network starts out with a guess for the output (target) with certain initial weights, and adjusts these weights to improve its performance. This process is repeated and eventually results in the approximation function for the targets, depending on the inputs. See Figure 2.2 for a schematic representation. Weights are adjusted with a backpropagation (backward propagation of errors) algorithm: this algorithm determines how strongly certain weights influence the error in the target guess and then adjusts them accordingly. Backpropagation takes the error associated with a wrong guess and uses that error to adjust the neural network's parameters in the direction of less error. In this way, weights that influence a bad outcome are punished and adjusted, weights that have a good influence are rewarded and kept. The backpropagation technique works in two stages. In the first stage the error function is propagated backward through the network to evaluate the derivatives such as Jacobian and Hessian matrices, whereas in a second stage the weight adjustment is done using the calculated derivatives and an optimization schemes such as steepest-descend or Newton's method.

To create the network, MATLAB's Neural Network Fitting Tool is used to train a two-layer feed forward network, consisting of a hidden layer that has a linear combination function and sigmoid transfer function for each node (Figure 2.2b) and an output layer with a linear combination and linear output transfer

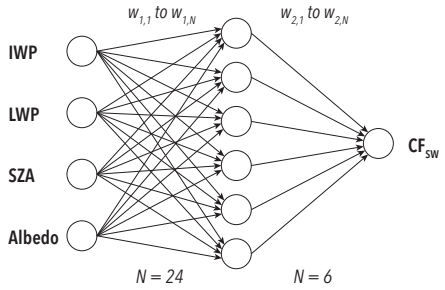

(a) SW-NN with 6 nodes in the hidden layer. Input for the network is cloud ice and liquid water path (IWP and LWP), solar zenith angle (SZA) and albedo.

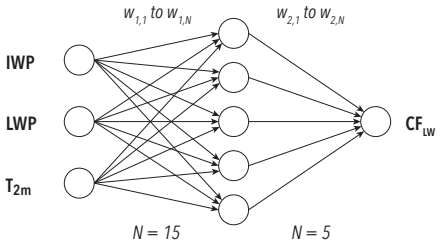

(b) LW-NN with 5 nodes in the hidden layer. Input for the network is cloud ice and liquid water path (IWP and LWP) and near-surface atmospheric temperature (T_{2m})

Figure 2.1: Schematic representation of the structure of the shortwave neural network (SW-NN) and longwave neural network (LW-NN) that give an estimation for the cloud factor (CF_{SW} and CF_{LW}). Each connection between nodes ($1:N$) is accompanied with a weight factor w, which is determined during training.

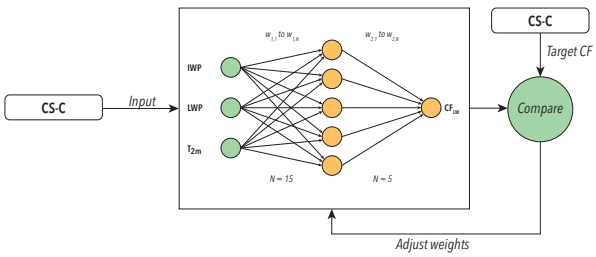

(a) Schematic overview of training the shallow feed forward network to determine longwave radiative cloud factors. Green indicates known parameters during training, yellow indicates the nodes where weights are updated every iteration. Input and target data is provided by the CloudSat-CALIPSO (CS-C) 2B-FLXHR-LIDAR product.

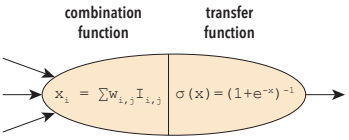

(b) Schematic representation of a neuron in the hidden layer: all input parameters ($I_{i,j}$) are weighted ($w_{i,j}$) and combined, then passed through a (nonlinear) sigmoid transfer function. For each neuron $w_{i,j}$ is different. For the output layer, the transfer function is linear.

Figure 2.2: Schematic representation of neural network training with (a) the overall structure of the neural network and flowchart during training and (b) the processing within each node of the network.

function. Most neural networks use the Levenberg-Marquardt backpropagation algorithm to update and minimize the errors, which is fast and has an efficient implementation in MATLAB [Hagan and Menhaj, 1994]. The Levenberg-Marquardt algorithm combines two minimization methods: the gradient descent method and the Gauss-Newton method. In the gradient descent method, the sum of the squared errors is reduced by updating the parameters in the steepest-descent direction. In the Gauss-Newton method, the sum of the squared errors is reduced by assuming the least squares function is locally quadratic and finding the minimum of the quadratic. The Levenberg-Marquardt method acts more like a gradient-descent method when the parameters are far from their optimal value and acts more like the Gauss-Newton method when the parameters are close to their optimal value [Gavin, 2019]. The Levenberg-Marquardt function uses the Jacobian matrix for calculations ($J = \nabla \mathbf{e}$; matrix containing first derivatives of the network errors with respect to the weights and biases) to approach the Hessian matrix ($H = \nabla^2 \mathbf{e}$; matrix containing the second-order derivatives).

The Hessian matrix is approximated as:

$$\mathbf{H} = \mathbf{J}^T \mathbf{J} + \mathbf{S} \tag{2.5}$$

where $\mathbf{S}$ is assumed to be approximately zero for the Gauss-Newton method. The gradient can then be computed as

$$\mathbf{g} = \mathbf{J}^T \mathbf{e} \tag{2.6}$$

with $\mathbf{H}$ the Hessian and $\mathbf{J}$ the Jacobian matrices, and $\mathbf{e}$ the vector of network errors [Hagan and Menhaj, 1994]. The Levenberg-Marquardt algorithm applies this approximation in the following Newton-like update:

$$\mathbf{w}_{k+1} = \mathbf{w}_k - \left[\mathbf{J}^T \mathbf{J} + \mu \mathbf{I}\right]^{-1} \mathbf{J}^T \mathbf{e} \tag{2.7}$$

When μ is zero, this is just Newton's method using the approximated Hessian matrix. When μ is large, this becomes gradient descent with a small step size. Newton's method is faster and more accurate near an error minimum, so the aim is to shift toward Newton's method as quickly as possible. Thus, μ is decreased after each successful step and is increased only when a tentative step would increase the performance function. In this way, the performance function is always reduced at each iteration of the algorithm [Hagan and Menhaj, 1994].

3

Methods

3.1. General approach

To couple the effect of clouds on the SEB to the SMB, simulations have been performed with the physically based snow model SNOWPACK [Lehning et al., 2002b]. Meteorological data is used to force the model, resampled to a 1°by 1°grid for three consecutive hydrological years, from March 2007 to March 2010 (starting and ending in fall). Two scenarios are simulated: an all-sky (AS) and a clear-sky (CS) scenario. The all-sky scenario provides the best estimate of the actual AIS cloud radiative forcing. In the clear-sky scenario, all clouds and their radiative effects are removed. Precipitation (both solid and liquid) is left unchanged to exclude other changes in the atmosphere and snowpack.

Both CloudSat-Calipso satellite retrievals and data from the regional climate model RACMO2.4 are used to obtain meteorological data. The satellite product provides detailed information on the cloud properties above the AIS, whereas the regional climate model provides data with a high temporal resolution.

A state-of-the-art hybrid dataset is created by combining both datasets, aiming to reduce model errors in cloud properties and resulting in a one of a kind observation-based dataset that has both high spatial and high temporal resolution. The hybrid dataset is evaluated to automatic weather stations (AWS) of the World Radiation Monitoring Center-Baseline Surface Radiation Network (BSRN), which determines the performance of the hybrid dataset. It is shown that the performance of the hybrid dataset is not better than the RACMO2.4 dataset, mainly due to a decrease in cloud liquid water path (LWP) with respect to RACMO2.4. As this discrepancy is found to be persistent on most of the ice shelves, it is concluded to work solely with RACMO2.4 data.

Radiative effects of clouds in the all-sky scenario are removed with the aid of neural networks (NN), to obtain the clear-sky radiative fluxes. Neural networks are required as there is no analytical solution to scale the fluxes with the available vertically integrated cloud data. CSC data is used to train the neural network, which thereafter enables the NN to scale the RACMO2.4 all-sky radiative fluxes to clear-sky fluxes.

The cloud radiative effect (CRE, $[Wm^{-2}]$) is defined as the difference in net radiation fluxes of the all-sky scenario to the clear-sky scenario simulation, defined in Equation 2.4. A positive CRE indicates net cloud warming at the surface; a negative CRE indicates net cloud cooling. The magnitude of the CRE is intimately connected to the amount of ice and liquid water in the cloud, its temperature, solar zenith angle and surface albedo. Before performing the simulations, the snowpack model has also been used to create initial snow profiles by conducting spin-up simulations. Simulations are done for each season during the three hydrological years defining summer as December, January, February (DJF), fall as March, April, May (MAM), winter as June, July, August (JJA) and spring as September, October, November (SON).

Finally, two sensitivity tests are conducted on the Larsen C ice shelf to gain more insight in uncertainties of output parameters. One sensitivity simulation is performed with a lower initial albedo, to assess the sensitivity to cloud radiative forcing on different snow conditions. A second sensitivity test carried out with simulations for perturbed LW and SW radiation values in the all-sky scenario, to assess sensitivity of the AIS to uncertainty in radiative forcing.

3.2. Data Sources

3.2.1. CloudSat-CALIPSO

The modified CloudSat-CALIPSO (CSC) product 2B-FLXHR-LIDAR R04 [Henderson et al., 2013] is used. The data is available from 2007 to 2010 and is used for three hydrological years: from March 2007 to March 2010. The product provides vertical profiles of radiative SW and LW fluxes and the respective no-cloud SW and LW fluxes at the same epoch that are retrieved from the broadband radiative transfer model. Only the surface fluxes are used for this study. The modified product adds retrieved integrated cloud ice and water content: the ice water path (IWP) and liquid water path (LWP) [Van Tricht et al., 2016b].

For the training of the neural networks only a subset of the CSC data is used to reduce computational power. An arbitrary choice is made to use CSC data of 2009. Only CSC observations that are above the 1°by 1°latitude-longitude grid of all ice shelves are included in the subset without further adaptations. For the construction of the hybrid dataset, the CSC has been assembled to the 1°by 1°latitude-longitude grid and each overpass is averaged to obtain one observational epoch on that gridpoint.

3.2.2. Regional Climate Model RACMO2.4

The RACMO2.4 data at a 27 km grid resolution is resampled to the 1°by 1°latitude-longitude grid, including only data that has an icemask of 1 (indicating year-round ice and thereby excluding sea ice) and including only data with elevations below 100 meter. As a result, not every simulation gridpoint includes as many RACMO data samples. All samples that fall within one grid box are averaged to obtain a representative value for the whole area. For the FilchnerRonne ice shelf the height threshold was set to $H < 150$ meter, as otherwise half of the ice shelf would have been excluded. For the Ross ice shelf, which is located closest to the South Pole, the latitude-longitude grid is set to a 1°by 2°grid due to the convergence of the longitude coordinates. RACMO data is equally spaced over the AIS and therefore the 1°by 1°would contain too few RACMO samples. By increasing the grid at the Ross ice shelf, the number of samples per gridpoint and the area it represents is increased and more comparable to other ice shelves. Another important consequence is that the number of simulation points at the Ross ice shelf is greatly reduced, from more than 250 to 148.

3.2.3. Automatic Weather Stations

Available ground-based observations from BSRN AWSs are used to evaluate the hybrid dataset that is constructed. The spatial coverage is very limited, with only 4 stations on the AIS. Of these, only the Georg von Neumayer station (GVN) is situated on an ice shelf (the Fimbull ice shelf) [König-Langlo, 2008, 2009, 2010]. The possibilities for evaluation are very limited because of this. Atmospheric conditions on the high plateau of the AIS are very different than at the Antarctic coasts and are not regarded as suitable for evaluation of the hybrid dataset, which is only located above ice shelves. BSRN South Pole (SPO) and Concordia (DOM) station are situated on the (inland) accumulation zone of AIS [Dutton, 2008, 2009, 2010, Vitale, 2009, 2010] and do not provide representative in-situ measurements for ice shelf conditions. BSRN Syowa station (SYO) is situated on sea ice [Yamanouchi, 2010].

3.3. Neural Networks

3.3.1. General

Radiative effects of the all-sky scenario are removed with the aid of neural networks (NN), to obtain the theoretical clear-sky radiative fluxes. CSC data provides both all-sky and clear-sky fluxes, retrieved with the 2B-FLXHR-LIDAR algorithms [Henderson et al., 2013], including a radiative transfer model for each slab in the vertical profile. Applying a radiative transfer model to obtain RACMO clear-sky fluxes would be possible but computationally very expensive, especially as it is not an option to process the standard output of RACMO, which only provides a vertically integrated value. Moreover, the hybrid dataset provides vertically integrated values of cloud properties and determining the corresponding fluxes with a radiative transfer model would not work. The application of neural networks to obtain a relationship between the necessary variables provides a very workable alternative, replacing a radiative transfer model altogether. CSC data is used to train the neural network, as it provides both input and desired output (targets). The NN thereafter enables the option to scale the RACMO2.4 all-sky radiative fluxes to clear-sky fluxes.

Downwelling LW and SW radiation are described by Equations 2.2 and 2.3. The emmissivity and transmissivity are complex to determine, especially for all-sky conditions, as they vary strongly in height

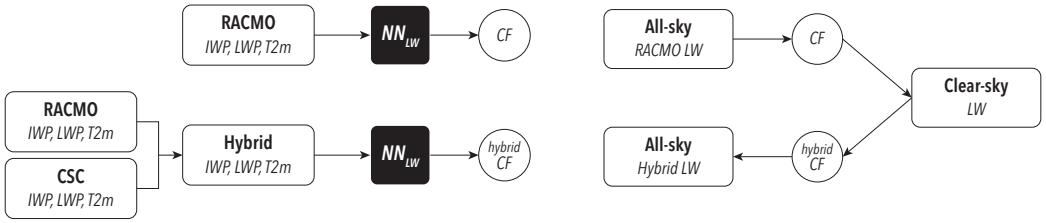

(a) Cloud properties of either original RACMO2.4 dataset (top) or constructed hybrid dataset cloud properties (bottom) provide input for the NN. The neural network then estimates the LW CF for the respective cloud properties.

(b) All-sky LW fluxes are scaled to clear-sky LW fluxes using obtained CF and equation 3.1. Then, clear-sky LW fluxes are re-scaled to all-sky fluxes using the hybrid CF and therefore result in hybrid all-sky LW fluxes.

Figure 3.1: Schematic representation of how longwave (LW) clear-sky and hybrid all-sky radiation fluxes are retrieved with the aid of neural networks (NN). The LW-NN estimates the cloud enhancement factor (CF) with given cloud properties of RACMO2.4: cloud ice water path (IWP) and liquid water path (LWP) and atmospheric temperature 2 meter above the surface (T2m). The hybrid cloud properties are a combination of RACMO2.4 and CloudSat-CALIPSO (CSC) data. This representation is for scaling LW fluxes, but is analogous for shortwave (SW) fluxes. The SW-NN depends on IWP, LWP, solar zenith angle and albedo.

(e.g. below cloud base and above cloud base height and within the clouds depend on the drop-size distribution). Alternatively, the translation from an all-sky to a clear-sky scenario can be described by the cloud enhancement factor (CF), defined in Equation 3.1. For LW radiation, the cloud enhancement factor describes an increase of the LW radiation and therefore CF_{LW} is greater than or equal to 1, whereas the cloud enhancement factor describes a decrease in downwelling SW radiation due to clouds and CF_{SW} is less than or equal to 1.

$$\begin{aligned} CF_{LW} &= \frac{LW_{AS}\downarrow}{LW_{CS}\downarrow}, \quad CF_{LW} \geq 1 \\ CF_{SW} &= \frac{SW_{AS}\downarrow}{SW_{CS}\downarrow}, \quad CF_{SW} \leq 1 \end{aligned} \tag{3.1}$$

The purpose of the neural networks is to generate a relation between the cloud properties that accompany LW or SW all-sky radiation values and the cloud enhancement factors. To provide optimal estimations for both CF_{LW} and CF_{SW}, two separate neural networks are trained. With the obtained relation, estimates of the CF can be made for any conditions. Then, having both all-sky fluxes and the CF, clear-sky fluxes can be resolved using Equation 3.1. In the creation of the hybrid dataset, first hybrid cloud properties are determined and secondly the clear-sky fluxes that have been obtained are scaled back to hybrid all-sky fluxes using these new cloud properties and corresponding new cloud enhancement factors. Figure 3.1 gives a schematic representation of the implementation of the neural networks by (a) providing estimations for the CF and (b) using the CF to scale and re-scale fluxes to obtain clear-sky and hybrid all-sky radiation values. The figure provides an example for LW radiation CF estimations and flux computations; SW radiation fluxes are re-scaled similarly but with the relevant cloud properties.

The CF_{LW} is primarily a function of cloud temperature, cloud height and emissivity. Emissivity is mainly determined by the cloud LWP and IWP. Cloud temperature is often approximated by cloud base temperature. However, this is not readily available from the 2B-FLXHR-LIDAR product or the ECMWF-AUX product that is used in the 2B-FLXHR-LIDAR product and neither is it available in the RACMO2.4 data. Therefore the atmospheric temperature 2 meter above the surface (T2m) is used from ECMWF ERA-Interim reanalysis data in the training stage of the NN, such that RACMO2.4 T2m values can be used when applying the NN. Van Tricht et al. [2016b] have investigated the relationship between the near-surface temperature and cloud base temperature on the GrIS and found high correlation (r = 0.83) for cases with IWP + LWP $\geq$ 10 gm^{-2}. It is expected that for the AIS this correlation is similarly high and that T2m is a good proxy to predict LW cloud radiation effects.

The CF_{SW} depends on cloud microphysical properties (IWP and LWP), surface albedo and solar zenith angele. IWP, LWP and albedo are available in both datasets. The solar zenith angle is provided in the CSC dataset, but not in RACMO2.4. For the latter, the solar zenith angle is computed depending on location, time and altitude and including the orbital elements for the sun.

3.3.2. Training the Neural Networks

A shallow neural network is used, as described in section 2.5. MATLAB's Neural Network Fitting Tool is used, which applies the Levenberg-Marquardt backpropagation algorithm to update and minimize errors during training of the network.

Two neural networks are trained: one for the cloud enhancement factor on LW radiation depending on IWP and LWP from CSC observations and T2m from ECMWF ERA-Interim, and one NN for the CF on SW radiation depending on IWP, LWP, solar zenith angle and albedo. For both, the CSC all-sky and no-cloud fluxes are used to determine the target CF data using Equation 3.1.

The NN training was conducted with CSC data of 4 months in 2009: January, April, July and October. This has been done to reduce data sizes but to still capture seasonal variations within the parameters. For the LW-NN, the performance was not satisfactory, and this dataset has been expanded to all CSC data in 2009. Only data above the ice shelves has been included in these datasets, to best capture their properties and preventing the NN to be tuned to other areas (for example the high plateau) that are not needed and might influence the resolution in which the NN can resolve CF.

The CSC data has been assembled on the 1°by 1°grid on all the ice shelves: of each overpass the data is stored when flying over one of the defined gridpoints. The ECMWF data has a lower spatial resolution than the defined grid boxes. Therefore for each lat/lon gridpoint the nearest ECMWF-T2m value (smallest Pythagorean distance) of the ECMWF grid is stored.

The input and target data are filtered to remove outliers and create a well-adjusted NN. Firstly, data that has been flagged erroneous is removed and negative downwelling SW radiation values between -1 and 0 Wm^{-2} are set to 0 Wm^{-2}. The largest 1% of IWP and LWP is removed due to possible groundclutter [L'Ecuyer et al., 2008] of CloudSat observations and observations with IWP or LWP larger than 2500 gm^{-3} are removed. Both these eliminations reduce the maximum IWP and LWP that the NN is trained with and thereby indirectly they limit the CF that can be resolved by the NN but this is expected to only influence outlier data. There is no real need to be able to resolve clouds that are exceptionally thick; for large outlier values of IWP and/or LWP the effect on radiation and thus the CF will be saturated. Therefore it is better to focus the resolving capacity of the NN for IWP/LWP values that a) occur frequently and b) for which the CF is still sensitive.

Furthermore, observations with an albedo < 0.5 are removed from the training data as these are not on an ice shelf. Cloud enhancement factor thresholds are forced. For the SW-NN, the CF ≤ 1 threshold is applied and values larger than 1 are set to 1. For the LW-NN, the threshold for the CF is CF ≥ 1.

To be able to match ECMWF-T2m to CSC observations, ECMWF-T2m values have been interpolated from 3-hourly values to a 1 minute resolution. For this, the spline interpolation method is used with Matlab's $interp1$ function: a piece-wise polynomial interpolation which bases interpolated values on the values at neighboring grid points. This interpolation is a better approximation for a temperature profile than linear interpolation, and does not introduce extra oscillations as is often the case with a polynomial fit. Values for T2m values interpolated linearly differ from -1 to 1 K with respect to the spline interpolated values (95 percentile 0.29 K).

The dataset is divided in 70% training, 15% validation and 15% testing data groups. The training dataset is used to identify and generate the fitting relations between the input and target data. The training dataset is adjusted using the validation dataset, stopping only when the stopping criteria is reached. The testing dataset is independent from all this, and is used to give insight in the level of over- or underfitting of the data.

The number of nodes in the shallow neural network determines the complexity of the relations that can be resolved. There is no definite approach to determine the best number of nodes for a data-fitting problem, but there are a few rules of thumb [Heaton, 2008] which provide a starting point, and then by trial and error a choice can be made. First rule of thumb: the number of hidden neurons should be 2/3 the size of the input layer, plus the size of the output layer. Second rule of thumb: the number of hidden neurons should be less than twice the size of the input layer. After trial and error, the best number of neurons for the SW-NN resulted in six hidden neurons, and for LW-NN five hidden neurons. Training of the NN using Levenberg-Marquardt backpropagation stops when the performance function is not reduced in six consecutive validation checks, or is minimized to the goal; an error of zero. For the SW-NN best performance is reached after 181 iterations, for LW-NN this is 661.

3.3.3. Assessment

The neural networks need to be able to give an accurate value for the prescribed targets. During training the NN is shaped to fit these outcomes. The testing subset of the data is independent from the training set and can provides a measure for how well the NN works.

If the neural network does a poor job predicting the targets in the testing dataset, this can be due to either over- or underfitting. In the case of overfitting, the network fits the training dataset too well, which disables it to perform for slightly different conditions. This can be improved by stopping the training earlier, or by reducing the number of nodes. In the case of underfitting, the network is not sophisticated enough yet. This can be improved by adding more neurons in the hidden layer or by using more data to train the network.

Analysing the regression of the NN predicted CF target values and the prescribed target values give an indication of the measure of over- or underfitting. If the regression for the validation subset is very near to 1 but the test-set is far from 1, there is a case of overfitting. If both are low, the NN underfits the data and not all features can be resolved.

See Figure 3.3 for the regression values of both the SW-NN and LW-NN. The SW-NN performs very well, with a regression of $r = 0.978$ for the independently tested dataset. The regression for the validation-set and the training set are also very similar, which indicates that there is no overfitting. Note that overfitting could still occur if properties were to be very different than what the NN is trained for, but as all seasons of all ice shelves are included, this is not expected; the dataset should enclose all conditions that will be encountered. It can be seen that the boundary value of a target CF ≤ 1 is difficult to resolve with the SW-NN, as values deviate furthest from the target fit (y=t). This is also the case for very low target values: the SW-NN does not resolve a CF below 0.5. This is not problematic since these values are very exceptional and possibly not realistic. The error between the supplied CF targets and NN CF output at the boundaries is larger with respect to other CF target values, but not that large that it is problematic. Of the independent testing dataset, the root mean squared error is 0.029. The error histogram, Figure 3.4a shows that the majority of errors for the testing dataset are 0.1 or less. The performance of the SW-NN is acceptable.

The regression values for LW-NN are also very good (Figure 3.3b): the independent test dataset has a regression $r = 0.984$, and like the SW-NN, this is similar to the validation dataset. Note that for the LW-NN CSC data of all 2009 was needed to obtain a well performing NN, whereas the SW-NN complied for one month of each season. When training the LW-NN with only 4 months of data, the NN was not able to resolve CF higher than 1.4; values that did occur regularly and can be resolved with the NN that is shown in Figure 3.3b. The Figure also shows that low CF target values can result in large over-estimations. This means that for thin, warm or cold clouds the radiative effect can be estimated higher than it should be, resulting in a much lower clear-sky flux value. The root mean squared error between the CF target and estimated CF by the LW-NN is small, 0.035. Similar to the SW-NN, the error histogram in Figure 3.4 shows that the majority of errors are 0.1 or less, which is satisfactory.

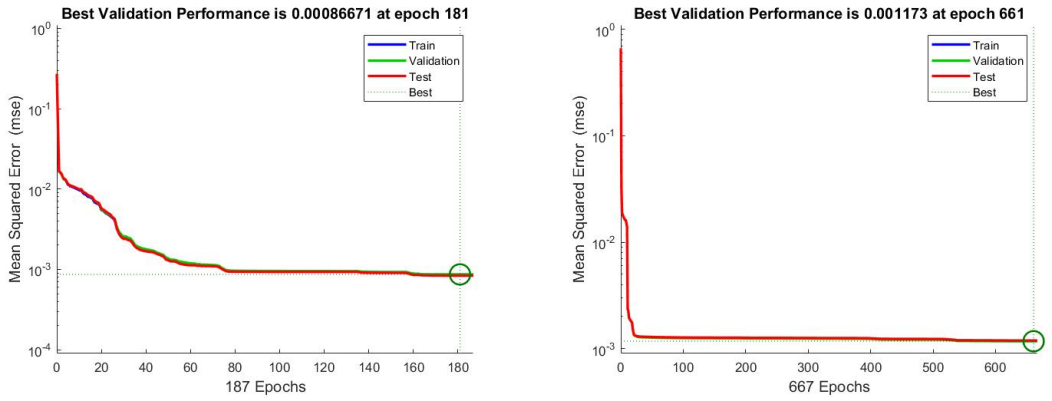

(a) SW-NN (b) LW-NN

Figure 3.2: Validation performance of (a) shortwave radiation neural network (SW-NN) and (b) longwave radiation neural network (LW-NN) during training of the networks. Training is stopped when the mean squared error, determined between validation and training data sets, has not reduced for 6 consecutive epochs. The testing dataset is independent from training and validation.

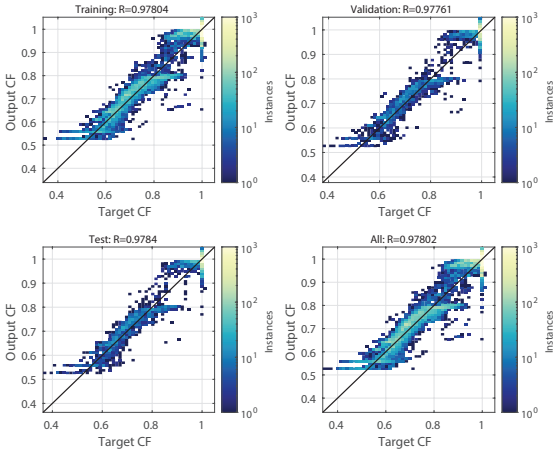

(a) SW-NN. Trained with CloudSat-CALIPSO data of 4 months in 2009 (January, April, July and October).

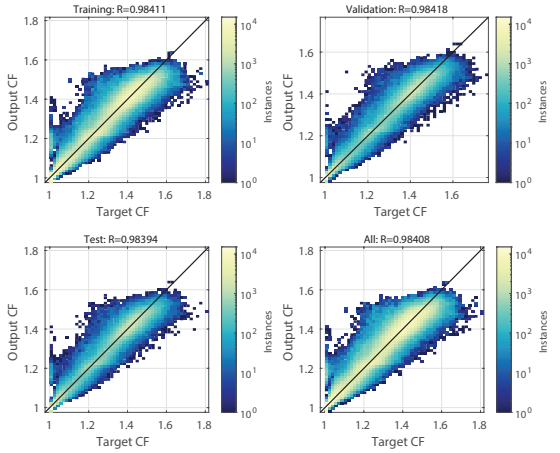

(b) LW-NN. Trained with CloudSat-CALIPSO data of all months in 2009.

Figure 3.3: Regression for trained (a) shortwave radiation neural network (SW-NN) and (b) longwave radiation neural network (LW-NN) between known target cloud enhancement factor (CF) and estimated CF by the networks. Each figure gives the regression for the training, validation and independent testing data subset and all of them combined. Colors indicate the sample count in the binned values.

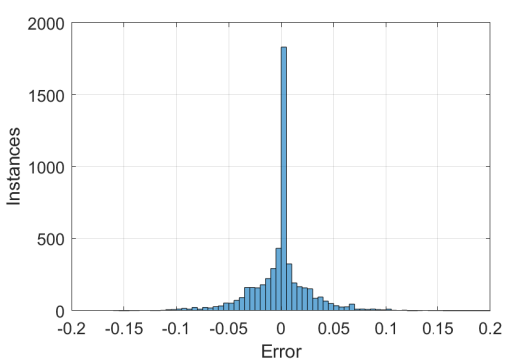

(a) SW-NN

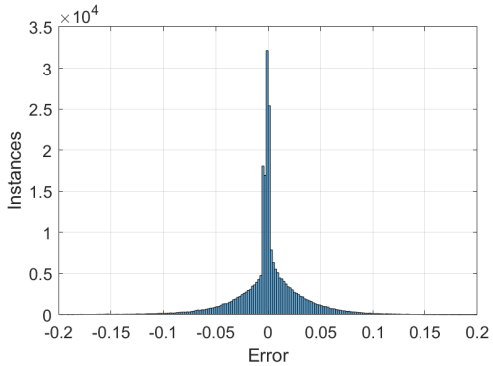

(b) LW-NN

Figure 3.4: Error histograms for the independent test data subset after training of (a) shortwave radiation neural network (SW-NN) and (b) longwave radiation neural network (LW-NN).

3.4. Hybrid dataset

3.4.1. General

Ideally the accuracy of the satellite observations and high temporal resolution of RACMO2.4 are combined to a state-of-the-art hybrid dataset. With the clear-sky fluxes and neural networks readily available, the procedure can be made backwards with new cloud enhancement factors and rescaling the clear-sky fluxes back to all-sky fluxes. For this, integrated hybrid ice water path (IWP) and liquid water path (LWP) values are needed, to calculate the new hybrid cloud factors. This method is preferred over directly combining LW and SW fluxes of both datasets, because that disables the link of the fluxes to the cloud properties.

The datasets are combined by fitting a moving average through both datasets at one location. The difference between these moving averages is the correction factor, which is exponentially weighted and added or subtracted to the RACMO2.4 data values at each timestep (see next section 3.4.2). After constraining the original model LWP/IWP by satellite retrievals, the trained neural networks were used to scale the modelled radiative fluxes accordingly. This was done by first converting the original RACMO fluxes to clear-sky fluxes and subsequently converting these clear-sky fluxes to radiative fluxes that match the hybrid LWP/IWP data set. This has been shown schematically in Figure 3.1

3.4.2. Combination of datasets

Both datasets are resampled to and averaged on the 1°by 1°grid boxes on the ice shelves, for all time steps. The RACMO2.4 data is a daily timeseries at each gridpoint, whereas the CSC are sampled every few days. During a CSC overpass multiple observations are taken within the same grid box, which do not have a sampling time difference more than a minute. These observations are averaged to one value at the epoch (day) of the overpass.

Next, a central moving average window is fitted through both datasets. The CSC data is first interpolated linearly before applying the moving average, to fill the missing data values. Tests have been performed without this interpolation, but resulted in either too much missing data and very little conversion of RACMO2.4 to CSC, or either the need of a extremely large moving average to reduce the missing data. Also, partly by the irregular sampling of CSC, the widths of the moving average window for both datasets are not the same. Multiple window widths have been tested and eventually this has been set to $M = 5$ days The central moving average window is defined in Equation 3.2 and 3.3, for the IWP or LWP of either dataset and using corresponding window width M. n is the data sample epoch on which the moving average is computed. The correction factor (C) is defined as the difference between the moving averaged values of IWP and LWP, given in Equation 3.4 and 3.5.

$$\overline{IWP} = \frac{1}{M}\sum_{k=0}^{M-1} IWP_{n-(M-1)/2+k}, \qquad n = 0,1,...,N \tag{3.2}$$

$$\overline{LWP} = \frac{1}{M}\sum_{k=0}^{M-1} LWP_{n-(M-1)/2+k}, \qquad n = 0,1,...,N \tag{3.3}$$

$$C_{IWP} = \overline{IWP}_{CSC} - \overline{IWP}_{RAC} \tag{3.4}$$

$$C_{LWP} = \overline{LWP}_{CSC} - \overline{LWP}_{RAC} \tag{3.5}$$

This correction factor is exponentially weighted and added or subtracted from the RACMO2.4 data, as described by Equations 3.6 and 3.7. The factor p determines the shape of the exponential function. Both the width of the moving average window and the exponential factor p were chosen in such a way that the resulting hybrid radiative fluxes resemble the satellite-retrieved radiative fluxes as closely as possible. The factor p varies from 0.01 to 1000 between the epochs; a small p corresponds to less correction. Adjustments always stop when IWP_{hybrid} or LWP_{hybrid} is larger than 1.5× the original IWP/LWP value to avoid that too much IWP/LWP is added or removed.

$$IWP_{hybrid} = IWP_{RAC} + C_{IWP}\left(1 - exp(-p_n IWP_{RAC})\right) \qquad p_n = 0.01,...,1000 \tag{3.6}$$

$$LWP_{hybrid} = LWP_{RAC} + C_{IWP}\left(1 - exp(-p_n LWP_{RAC})\right) \qquad p_n = 0.01,...,1000 \tag{3.7}$$

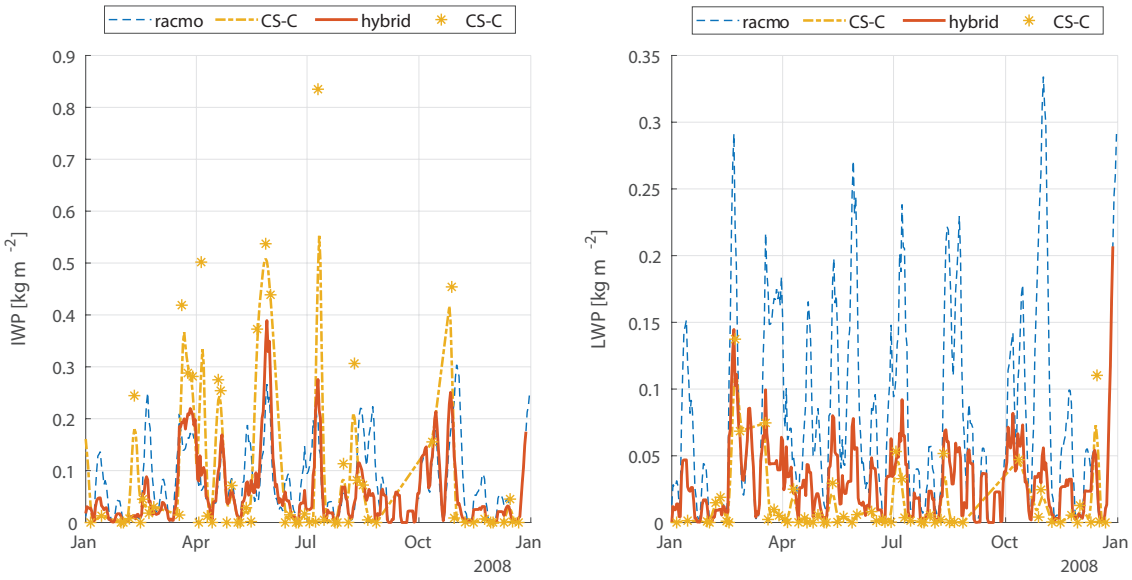

Figure 3.5: Example of hybrid dataset correction at Georg von Neumayer (GVN) automatic weather station for 2008 for cloud ice water path (IWP, left figure) and cloud liquid water path (LWP, right figure). RACMO2.4 data (blue, dashed) is plotted with 5-day moving average through its respective IWP and LWP values. CloudSat-CALIPSO (CSC) samples (yellow star markers) have been linearly interpolated and visualized with a 5-day moving average (yellow line). The constructed hybrid data, a weighted adjustment of the difference between RACMO and CSC is visualized with the solid orange line.

3.4.3. Assessment and Considerations

The hybrid dataset is assessed to the BSRN Georg von Neumayer (GVN) automatic weather station, which is the only BSRN AWS that is located on an ice shelf. In Figure 3.5 both datasets and the hybrid data values after the correction procedure are shown for the year 2008, to give an indication of the changes. It can be seen that IWP values of the two datasets agree better than LWP values. The correction is therefore more pronounced for LWP values. The resulting median difference between hybrid and original model IWP values is 0.004 kgm^{-2} (99 percentiles: -0.14 to 0.33 kgm^{-2}), whereas the median difference in LWP values is 0.025 kgm^{-2} (99 percentiles: -0.07 to 0.55 kgm^{-2}).

Figure 3.6 shows that the hybrid dataset SW fluxes are reasonably similar to the original RACMO fluxes, and that both have a good regression to the observed fluxes at GVN. An overview is given in Table 3.1, including daily and monthly mean bias and root mean squared error (RMSE). The RMSE is 8.8Wm^{-2} for the original RACMO SW fluxes to GVN (monthly average values) and 11.2Wm^{-2} for the hybrid fluxes compared to GVN, showing an increase in error. The mean bias is for original and hybrid $-4.8Wm^{-2}$ and $-7.3Wm^{-2}$ respectively.

Figure 3.6 also shows that the LW fluxes are underestimated at GVN, which is noticeably enhanced in the hybrid dataset instead of decreased. This is attributed to reduced LWP values in the hybrid dataset which correspond to lower LW flux values. The mean bias in the data (monthly values) is increased from 11.1Wm^{-2} to 19.3Wm^{-2} in the hybrid dataset. The original RMSE to GVN was 13.3Wm^{-2} for RACMO LW fluxes whereas the RMSE for the hybrid fluxes is increased to 20.8Wm^{-2}. Conclusively, the performance of the hybrid dataset is less than the original RACMO data, for both SW and LW fluxes but with the largest errors due to the underestimation of LW fluxes. Thus, the hybrid dataset does not reach its goal to provide the best estimates of atmospheric conditions.

Considering conditions at all ice shelves and comparing the IWP and LWP values, it is found that the LWP bias between RACMO and CSC is present at all ice shelves. Such that RACMO consistently provides higher LWP values. The mean difference for IWP ($IWP_{RAC} - IWP_{CSC}$) is 0.0082 kgm^{-2} (median: 0.007 kgm^{-2}, 99 percentile: -0.45 to 0.24 kgm^{-2}) and the median difference for LWP ($LWP_{RAC} - LWP_{CSC}$) is 0.0429 kgm^{-2} (median: 0.013 kgm^{-2}, 99 percentile: -0.07 to 0.357 kgm^{-2}). Van Wessem et al. [2018] also show this systematic bias, Figure 3.7, but with larger values for this LWP bias at the coastal bins: up to 0.060 kgm^{-2}. This discrepancy in bias could be because a) their coastal bins include elevations up to 200 meter instead of 100 meter, b) the aggregation of values to the 1°by 1°grid reduces the bias. In any case, RACMO

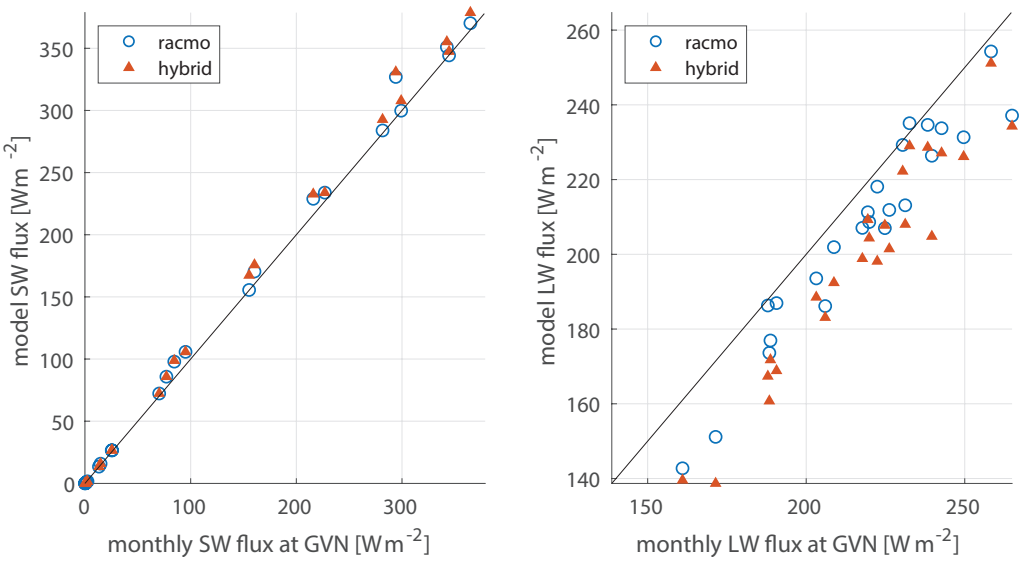

Figure 3.6: Regression between Georg von Neumayer (GVN) automatic weather station monthly averaged observed shortwave (SW) radiation fluxes (left figure) and longwave (LW) radiation fluxes (right figure) compared the original RACMO2.4 model data (orange circles) and the hybrid data (blue traingles) in 2008-2009.

2008&2009	Mean bias daily (Wm^{-2})	RMSE daily (Wm^{-2})	Mean bias monthly (Wm^{-2})	RMSE monthly (Wm^{-2})
SW: GVN - racmo	-4.6	28.5	-4.8	8.8
SW: GVN – hybrid	-6.9	29	-7.3	11.2
LW: GVN - racmo	11.1	28.8	11.1	13.3
LW: GVN – hybrid	19.2	35.4	19.3	20.8

Table 3.1: Biases and root mean squared error (RMSE) between Georg von Neumayer (GVN) automatic weather station observed shortwave (SW) and longwave (LW) radiation fluxes to either original RACMO2.4 (racmo) modeled radiative fluxes or hybrid fluxes.

LWP values are higher than CSC retrievals and therefore the hybrid dataset will inevitably provide lower LWP values and lower LW fluxes compared to RACMO, which subsequently increases the flux bias.

The only option to improve result of the hybrid dataset is by changing the moving average window width M and exponential weight p during the combination procedure. Because of the systematic LWP bias of the datasets, improvements for the hybrid dataset by changes in M or P are not feasible: whichever choice for M and p, the LWP of the hybrid dataset will be lower than the original RACMO values. A reduction of LWP will reduce the downwelling LW flux, increasing the flux bias compared to AWS. Conclusively, the best performance of the hybrid dataset is achieved when LWP is *not* reduced, i.e., the hybrid dataset is not constructed.

3.5. Simulating the Surface Mass Balance using SNOWPACK

3.5.1. The Snow Model SNOWPACK

SNOWPACK [Lehning et al., 2002b] is a one-dimensional physical snow and land-surface model, which focuses on a detailed description of the mass and energy exchange between the snow and the atmosphere. SNOWPACK models the snow micro-structure, snow metamorphism and macroscopic properties of the snowpack. SNOWPACK is based on a Lagrangian finite element implementation and solves the in-stationary heat transfer and settlement equations. Phase changes and transport of water vapor and liquid water are included. Special attention is paid to the metamorphism of snow and its connection to mechanical properties such as thermal conductivity and viscosity. SNOWPACK is a sophisticated snow cover model in terms of microstructural detail [Lehning et al., 2002b]. The output of the model is a set of timeseries that describe the snow profile (albedo, temperature, grain size, density and water content) and its processes (refreezing, water retention). SNOWPACK was developed for seasonal snow, but it has been successfully

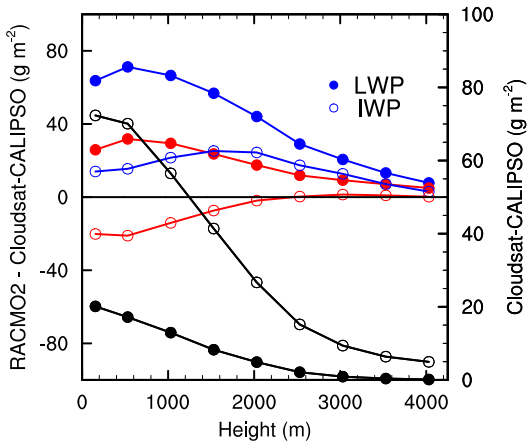

Figure 3.7: Figure from Van Wessem et al. [2018]: Absolute bias (left axis) in average (2007–2010) cloud ice water path (IWP) (open circles) and cloud liquid water path (LWP) (closed circles) for RACMO2.3p2 (blue) and RACMO2.3p1 (red) compared to the CloudSat–CALIPSO product [Van Tricht et al., 2016b]. Also shown are the observational data (black circles, right axis). The data are binned in 500m surface elevation intervals (0–250, 250–750, etc.). RACMO2.3p2 is otherwise referred to as RACMO2.4

applied to Antarctica as well [Groot Zwaaftink et al., 2013]. SNOWPACK is used in this study to incorporate the response of the AIS surface to different radiative forcing schemes in offline simulations, which is not easily done with regional climate models.

A constraint due to SNOWPACK modelling in 1D is that the spatial resolution of the study depends on the number of simulation points. Each point simulation is computationally expensive and consequently the number of simulation points is constrained by the available computation time. This led to the choice to resample data to the 1°by 1°grid boxes, where each grid box is one point simulation. Simulations have been performed locally with parallel processing [Arrow et al., 1961].

SNOWPACK's energy balance is conform Equation 2.1: incoming and outgoing SW and LW radiation, Latent and Sensible heat flux, Ground heat flux and in which the internal energy change (cold content and phase change) are included. Required meteorological input for SNOWPACK is: air temperature T (K), relative humidity RH (-), wind velocity VW (m/s), incoming SW and LW radiation (Wm^{-2}), precipitation (mm) and the cloud optical depth τ (m/m). τ is only required when the Gardner and Sharp [2010] albedo parameterization is used. The meteorological forcing are provided by the RACMO2.4 data, resampled to the defined grid.

If no initial snow profile is provided for the start of the simulation, SNOWPACK assumes a surface without snow or ice. Therefore, to perform a snow profile time evolution study, vertical snow profiles at each simulation gridpoint are required. These are obtained by performing spin-up simulations, discussed in section 3.5.6.

3.5.2. Model Settings

For each gridpoint simulation the same model settings are used, of which a few are discussed here. See also Table 3.2. First of all, the *default* variant of the model is used. There is a specific variant available for Antarctica, but this has been developed specifically for the high plateau which is not necessarily suited for simulations on the ice shelves. Testing both variants during the spin-up phase of simulations showed that the Antarctic variant had a higher number of layers for the same profile depth, i.e. a higher vertical resolution, but otherwise similar profiles as the *default* variant (in terms of grain size and shape, temperature, etc.) and thus was not used. Spin-up simulations have been performed with a timestep of 30 minutes to increase calculation speed; the simulations for 2007-2010 are performed at 15 minute temporal resolution. Input and output values, however, have a 3-hr resolution. Input values are linearly interpolated by the model to obtain the 15 minute or 30 minute temporal resolution. Output values are the modelled value at that epoch. Output of SMB components are cumulative values at each epoch.

Temperature, relative humidity and wind speed are given at fixed height above the surface (at 2 meter for temperature and relative humidity, at 10 meter for wind speed) at all times. This means that if the elevation of the surface changes due to precipitation, these values are kept aligned above the new surface elevation at their respective heights. Neumann boundary conditions are maintained at the surface throughout the

Modelling time step	15 min
Atmospheric stability correction model	Monin-Michlmayr
New snow density model	Zwart [2007]
Albedo parameterization	Gardner and Sharp [2010]
SW radiation penetration	Multi-band
Boundary conditions	Neumann
Geothermal heat flux	0 Wm^{-2}
Ground Temperature (constant)	yearly average air temperature
Height of meteo values	2 m
Height of wind values	10 m
Aerodynamic roughness length	0.001 m
Temperature threshold for rain/snow transition	1.2 °C
New snow grain radius (geometric)	11 μm
New layer height	0.01 m
Minimum layer height	0.005 m
Soot concentration	0 ppmv

Table 3.2: Summary of essential model settings in SNOWPACK. Documentation of the model can be found at `https://models.slf.ch/docserver/snowpack/html/`

simulation, which specifies boundary flux values described in Equation 3.8 instead of constant values (a Dirichlet boundary condition, Equation 3.9) [Cheng and Cheng, 2005]:

$$\frac{\partial y}{\partial n} = f(x) \tag{3.8}$$

$$y = g(x) \tag{3.9}$$

At the bottom of the snow profile, however, the ground temperature is used as a Dirichlet boundary condition instead of the geothermal heat flux. As this study focuses on surface processes, the influence of ground fluxes is eliminated by padding the snow profile with a lot of ice layers at the bottom. The ground temperature is set to the yearly averaged air temperature, as is often done for unknown ice profiles.

Lastly, the Zwart snow density model is used within SNOWPACK, preferred over Lehning snow density model as it is better suited for the AIS: Zwart better includes wind effects, can resolve higher densities and is less sensitive for the surface temperature compared to Lehning [Zwart, 2007].

3.5.3. Albedo parameterization

The albedo parameterisation used by RACMO2.4, described in section 2.4, has been implemented in SNOWPACK as well, to best represent AIS conditions: the prognostic broadband snow surface albedo parameterization based on snow grain size evolution (r_e), cloud optical depth (τ), solar zenith angle (u) and concentration of light-absorbing impurities at the surface. The parameterization is provided by Gardner and Sharp [2010]:

$$\alpha = \alpha_S + d\alpha_u + d\alpha_c + d\alpha_\tau. \tag{3.10}$$

In this formulation, α_S is a base albedo due to snow grain size, increased by contributions due to the zenith angle ($d\alpha_u$), impurities ($d\alpha_c$), and clouds ($d\alpha_\tau$). Assuming that impurity content is negligible on the AIS, the relevant equations for α become

$$\alpha_S = 1.48 - 1.27048 r_e^{0.07} \tag{3.11}$$

$$d\alpha_u = 0.53\alpha_S(1-\alpha_S)(1-0.64x-(1-x)u)^{1.2} \tag{3.12}$$

$$d\alpha_c = 0 \tag{3.13}$$

$$d\alpha_\tau = \frac{0.1\tau\alpha_S^{1.3}}{(1+1.5\tau)^{\alpha_S}}, \tag{3.14}$$

where $x = \min(\sqrt{\tau/2u}, 1)$. This albedo parameterization has been validated against field observations of albedo for the period 1995 – 2004 by Kuipers Munneke et al. [2011] and proved to exhibit the expected behaviour over the Antarctic continent well.

SNOWPACK calculates the albedo per snow layer. This is important, as the albedo of a thin layer of snow is influenced by the albedo of the underlying surface. It is assumed that the effect of an underlying layer decreases exponentially with depth below the surface [Oerlemans and Knap, 1998]. When performing sensitivity simulations to the initial albedo, the 20 top layers of the snow profile have been adjusted to a new, larger grain size (adjusting α_S in Equation 3.10 accordingly, while keeping α_u and α_τ the same) to decrease the albedo.

3.5.4. Cloud Optical Depth

The Cloud Optical Depth (τ) is calculated seperately for ice (subscript *i*) and water (subscript *w*) using the parameterization provided by Stephens [1978a]:

$$\tau_i = \frac{3}{2}\frac{IWP}{\rho_i R_{eff,i}} \tag{3.15}$$

$$\tau_w = \frac{3}{2}\frac{LWP}{\rho_w R_{eff,w}}, \tag{3.16}$$

And the total cloud optical depth is

$$\tau = \tau_i + \tau_w. \tag{3.17}$$

The effective particle radius used for ice is $R_{eff,i} = 30\mu m$ and for water $R_{eff,w} = 13\mu m$, which are the same values applied for IWP and LWP retrievals in the 2B-FLXHR-LIDAR product [Henderson et al., 2011]. The respective densities are $\rho_i = 916.7 kgm^{-3}$ and $\rho_w = 1000 kgm^{-3}$. IWP and LWP (kgm^{-2}) are integrated cloud ice/water content over cloud depth z under the assumption that the cloud is vertically uniform with respect to the drop-size distribution, i.e. well-mixed. This assumption is not accurate and influences the radiative flux divergence of the cloud [Shupe and Intrieri, 2004, Stephens, 1978b], but neither CSC nor RACMO provide a vertical profile of ice and liquid cloud content. Though mixed clouds are shown to have a strong contribution to the the SEB in the Arctic [Shupe and Intrieri, 2004] and it can be expected that simulations will therefore not severely underestimate cloud radiative effects. IWP and LWP are included in the RACMO dataset as daily values and therefore τ is calculated as a daily averaged value and applied to each epoch at that day.

3.5.5. Cold Content

The cold content of the snow is the amount of energy (Jm^{-2}) required to warm the snowpack to 0°C [Marks et al., 1999]. It is a description of the thermal state of dry snow. This is a useful parameter to interpret the delay between air temperature and surface temperature raising above melting point and the actual melt of a snowpack. Surface temperatures quickly respond to atmospheric forcing whereas the sub-surface layers respond more slowly. For the comparison between the all-sky and clear-sky scenarios, the thermal state of both the surface and sub-surface layers is a more useful parameter to determine if the different atmospheric forcing induces changes in the snowpack than the surface temperature of the snow.

The cold content (CC) is based on the heat capacity (cp) and temperature of each SNOWPACK output layer *i* with height *h*, given as

$$CC = \sum_{i=-z}^{0} cp_(i)T(i)h(i). \tag{3.18}$$

The CC is usually determined for the total depth of the snow profile, but due to the isolation layers used in this study this is not a representative value to analyze surface properties. Instead, the CC is calculated over the top 0.1 meter of snow ($z = 0.1m$). This has been chosen by testing multiple values for z. A thicker layer obscured important seasonal values: it is of interest to see if and when the near-surface layers reach (approximately) 0°C.

The heat capacity cp ($Jkg^{-1}K^{-1}$) of each layer *i* is calculated under the assumption that only ice and air is present. If water is present, the snow is melting and $T = 0°C$. The heat capacity is given as

$$cp(i) = \frac{(1-\rho(i)/\rho_{ice})\cdot cp_{air}\rho_{air} + \rho(i)\cdot cp_{ice}}{\rho(i)}. \tag{3.19}$$

The heat capacity of ice is $cp_{ice} = 2100 Jkg^{-1}K^{-1}$, the heat capacity of air is $cp_{air} = 1004.67 Jkg^{-1}K^{-1}$, $\rho_{air} = 1.1 kgm^{-3}$ and $\rho(i)$ is the density of the layer, as used by SNOWPACK [Lehning et al., 2002b].

Modelling time step	30 min
Time period	2×(1 Mrt 2001 - 1 Mrt 2016)
Grain radius	2 mm
Starting snowpack profile depth	60m
Isolation layers	50×1 m
Top layers	10×0.1m
Snow temperature at isolation layers	2001-2016 mean surface temperature
Snow temperature at top layers	Linear increase from 2001-2016 mean surface temperature to 1 March 2001 surface temperature

Table 3.3: Information on spin-up simulations performed by SNOWPACK.

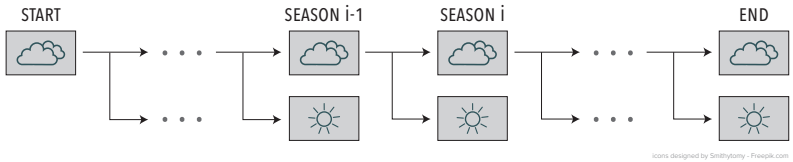

Figure 3.8: Schematic representation of the simulation procedure that starts and ends at each season of the year for the simulation period of March 2007 - March 2010. Each season i is simulated for both all-sky (cloud icon) and clear-sky (sun icon) scenarios. Both scenarios use the snow profile output from the previous all-sky simulation as initial snow profile.

3.5.6. Spin-up Simulations

Initial snow profiles are needed to perform an accurate snow profile time evolution study. These profiles are created by performing a 30-year spin-up simulation. This is a good and available method to create profiles with the needed high vertical resolution for all grid points and is a better option than only using initial surface values based on output of a regional climate model. The result of the spin-up simulation is the initial snow profile on which the scenario simulations are performed. These profiles are different for each location, depending on the respective meteorological conditions at those locations.

As stated before, the snow profiles also need to include isolation layers to eliminate effects from the bottom of the ice shelf. Thus, the spin-up simulations start with these isolation layers, in total 60 meter thick. During the spin-up simulation the surface layers are refined and adjusted to more realistic and representative snow profile layers occurring at each 1°by 1°gridbox. At the start of the spin-up simulation, the snow profile consists of 50 bottom ice layers with a height of 1 meter and 10 top layers of 0.1 m; providing an initial guess of the profile parameters. The temperature of this snow profile is set to the yearly averaged air temperature in the bottom (isolation) layers and increases linearly in the top layers to the air temperature at the start of the spin-up simulation. It is expected that the guesses for the snow profile properties at the start will be of no influence for the values at the end of the 30-year spin-up simulation. Nevertheless, an effort is made to make these plausible. See Table 3.3 for a summary. The spin-up simulation time is 30 years, to capture any climatological cycle that might occur and to diminish the influence of the initial snow property guesses. Available RACMO meteorological data from 2001-2016 is repeated twice to reach this timespan. Note that because of this, the spin-up simulation is not used to create the actual snow profiles at each location but to create representative and detailed snow profiles.

3.5.7. Simulation Scenarios

To create insight in the temporal variability of the CRE, each season in the three hydrological years is simulated individually. This approach enables the quantification of the CRE per season, as each season can be initialized on the same snow profile. Each season is initialized with preceding all-sky conditions. Then, each season is simulated twice: once for all-sky conditions (AS) and once for clear-sky (CS) conditions. This means: March-April-May (MAM) in 2007 (first season that is simulated) is initialized with the spin-up snow profile, then simulated for both AS and CS conditions. The next season, June-July-August (JJA) is initialized on the snow profile that is output of the MAM all-sky simulation, then simulation for both AS and CS conditions, and so on. The result of this is a continuous all-sky simulation (output from one all-sky simulation is input for the next all-sky simulation) and a clear-sky simulation that has a 'reset' of snow conditions at the start of every season (output from the previous all-sky simulation is used as input for a clear-sky simulation). This procedure is schematically shown in Figure 3.8.

Conclusively, there are two scenarios using this approach:

1. All-sky (AS) scenario: simulation of a season with all-sky forcing and all-sky initialisation (i.e. preceding all-sky conditions). This scenario is closest to reality and includes all clouds that have occurred. Note that it is not necessarily always overcast in this scenario.

2. Clear-sky (CS) scenario: simulation of a season with clear-sky forcing and all-sky initialisation.

3.5.8. Sensitivity Simulations

There is no uncertainty directly derivable from SNOWPACK, as the model includes many different schemes. For this reason, sensitivity simulations are performed to gain a level of insight in the fluctuations of output. These sensitivity simulations are performed only on the Larsen C ice shelf to limit computational time.

The AS and CS scenario are both initialized on the same (AS) snow profile each season and diverge from there on. For the cumulative SMB output parameters, there is an obvious reset to baseline values each season because of this. However, for the periodical fluctuating parameters, this reset will only slightly be noticeable, if at all. To investigate the sensitivity of the simulation to the initial surface albedo value, AS and CS simulations have been performed with lower initial albedo. For this, the upper 20 layers of the snow profile used to initialize each season are set to have a larger grain size, decreasing α_S in equation 3.10.

To investigate the sensitivity of the simulations to perturbations in LW and SW input, each season is forced with +10 Wm^{-2} LW or SW radiation and with -10 Wm^{-2} LW or SW radiation. Perturbations are applied on each timestep of the AS input dataset. This results in 4 additional simulation outputs: $LW_{enhanced}$, $LW_{reduced}$, $SW_{enhanced}$ and $SW_{reduced}$. These simulations are only performed for the AS scenario.

4

Results

To analyze the impact of the cloud radiative effect (CRE) on the Antarctic Ice Shelves, first the CRE is quantified and secondly the response of snow surface parameters is analyzed. This chapter structurally regards the LarsenC ice shelf first and thereafter regards all other ice shelves. This has been done to be able to analyze each parameter in detail and to keep inter-comparisons between ice shelves on a more general level. This way, the report is kept as compact as possible without losing analysis quality. For some parameters, depending on their importance for the main results, the figures for each ice shelves are added only in appendix A. The results are of most significance for the summer (DJF). Therefore, quantification of parameters are mostly given for this season only. In appendix B values for all seasons are included.

4.1. Quantification of the Cloud Radiative Effect

4.1.1. Shortwave Radiation

As expected, SW radiation shows a strong seasonal and daily cycle. See Figure 4.1 for (a) incoming SW radiation (SW_{in}), (b) outgoing SW radiation (SW_{out}) and (c) net SW radiation (SW_{net}) at the surface of the Larsen C ice shelf for both all-sky (AS) and clear-sky (CS). For all SW_{in}, SW_{out} and SW_{net} the values are highest in summertime when the sun's energy reaches the polar hemisphere. It is evident that clear-sky SW fluxes are consistently higher for SW_{in}, SW_{out} and SW_{net}. The cloud radiative effect on the net SW radiation budget (CRE-SW) is a negative effect, i.e. a reduction: CRE-SW < 0. A noticeable peak can be found in the all-sky simulation for SW_{in} around December 2007, due to a cloud-free period (not shown). The peak is less pronounced in SW_{out} (SW_{out} naturally being influenced less by clouds) and consequently is pronounced in SW_{net}. In the clear-sky timeseries this temporal variation due to cloud cover is of course not present and therefore the CRE-SW is significantly smaller during that time period in 2007. Similarly, in other years, the summer CRE-SW shows a higher spatial variation regarding the cloud cover fluctuations of the AS scenario.

The cloud effect on net SW radiation (CRE-SW) at the Larsen C ice shelf is on average: $-36.2 \pm 2.2 Wm^{-2}$ in DJF, $-5.1 \pm 0.8 Wm^{-2}$ in MAM, $-0.6 \pm 0.6 Wm^{-2}$ in JJA, $-22.5 \pm 1.1 Wm^{-2}$ in SON. Uncertainties are derived from the sensitivity simulations. It is evident that the strongest cloud radiative cooling occurs in spring and summer. Variations within each season are very high due to the strong seasonal cycle of the SW radiation (and partly due to spatial variations).

The described seasonal cycle in SW radiation is similar for all ice shelves (Appendix A.1), where the winter SW budget approaches zero and the budget is maximal in summer. Qualitatively the CRE-SW is also the same for the ice shelves: clouds reduce the net SW budget. In Table 4.1 the values for DJF are summarized. The averaged ice shelf wide CRE-SW is $-39.2 Wm^{-2}$ in DJF, $-2.7 Wm^{-2}$ in MAM, $-0.1 Wm^{-2}$ in JJA and $-16.9 Wm^{-2}$ in SON. This amounts to a yearly ice shelf wide cloud SW cooling of CRE-SW $= -14.6 Wm^{-2}$. It is obvious that the cloud effect on SW radiation is largest in summer and also very large in spring. The large difference between spring and fall cloud effects is somewhat unexpected, though easily explained by the solar cycle that is not equally distributed over the assigned seasons; SW radiation is roughly available through the months September-April. The SW_{net} radiation budget is much higher in spring than in fall and therefore all-sky and clear-sky values can diverge more: the ice shelf wide average SW_{net} values for spring and fall respectively are 23.3 Wm^{-2} compared to 4.3 Wm^{-2} for all-sky conditions and 40.2 Wm^{-2} compared to 7.0 Wm^{-2} in clear-sky conditions.

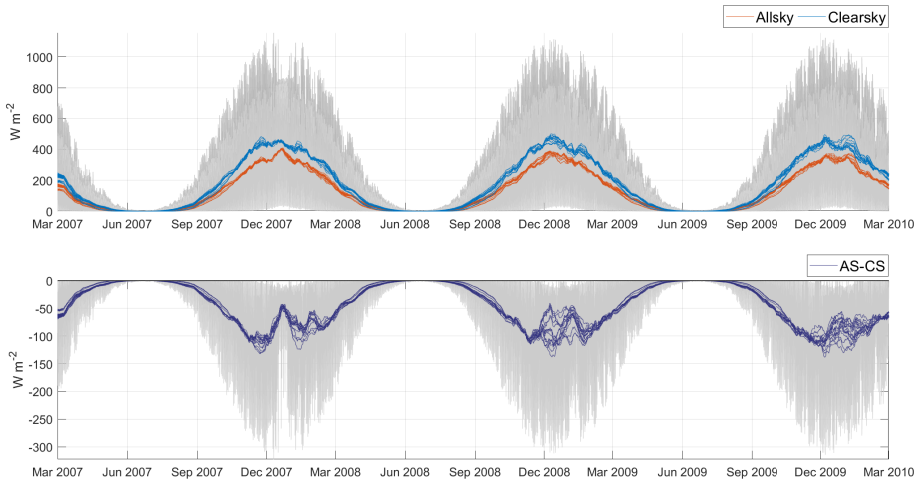

(a) Incoming SW radiation, SW_{in} at Larsen C ice shelf

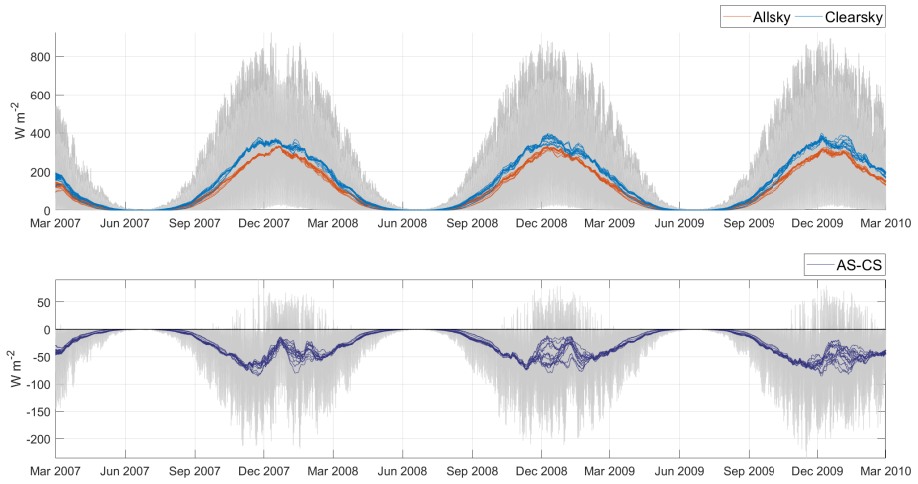

(b) Outgoing SW radiation, SW_{out} at Larsen C ice shelf

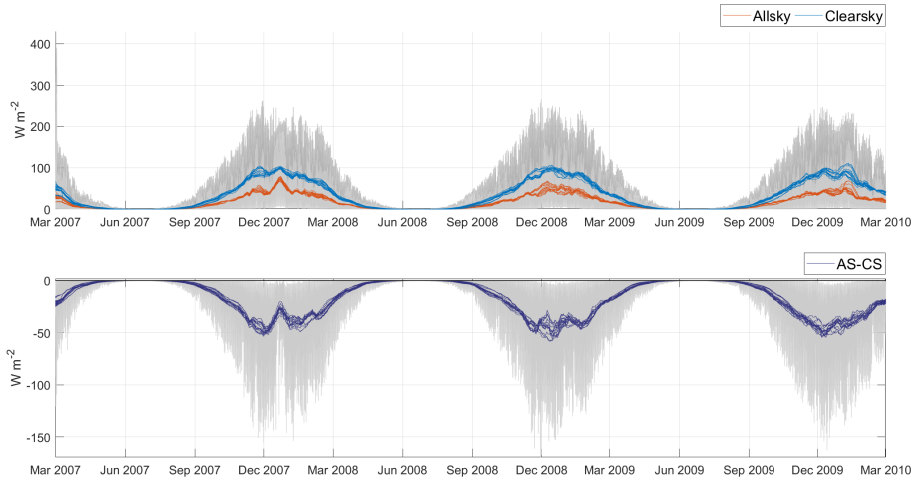

(c) Net SW radiation, SW_{net} at Larsen C ice shelf

Figure 4.1: Timeseries of shortwave (SW) radiation at Larsen C ice shelf. (a) SW_{in}, (b) SW_{out} and (c) SW_{net}. Each simulation gridpoint is shown (n=16) for both all-sky (AS, orange) and clear-sky (CS, blue) scenario (top figures) and the respective cloud effect (purple, bottom figures) with a 15-day moving average. Shaded in grey are the 3-hourly timeseries.

SW_{net} (Wm^{-2})	Amery	Filchner-Ronne	Fimbull	Larsen C	Riiser-Larsen	Ross	Shackleton	West	Wilkins & George VI
All-sky	58.2	52.1	49.1	38.5	46.5	49.8	46.1	48.6	42.8
Clear-sky	87.2	92.8	83.9	74.7	83.8	91.4	80.7	78.9	76.2
CRE	-29.0	-40.7	-34.7	-36.2	-37.3	-41.6	-34.6	-30.3	-33.3

Table 4.1: Average net SW (Wm^{-2}) values for summer (DJF) at each ice shelf. Values are averaged over the three simulation years 2007-2010, and spatially averaged. Uncertainties in these fluxes are approximately 2.2 Wm^{-2} for DJF.

LW_{net} (Wm^{-2})	Amery	Filchner-Ronne	Fimbull	Larsen C	Riiser-Larsen	Ross	Shackleton	West	Wilkins & George VI
All-sky	-55.4	-43.5	-47.3	-33.1	-42.5	-42.9	-44.6	-48.3	-40.7
Clear-sky	-88.0	-89.6	-92.4	-84.7	-89.5	-90.6	-91.9	-90.4	-86.9
CRE	32.6	46.1	45.0	51.6	47.0	47.8	47.3	42.2	46.2

Table 4.2: Table of average net LW (Wm^{-2}) values for summer (DJF) at each ice shelf. Values are averaged over the three simulation years 2007-2010, and spatially averaged. Uncertainties in these fluxes are approximately 6.5 Wm^{-2} for DJF.

4.1.2. Longwave Radiation

See Figure 4.2 for (a) the incoming LW radiation LW_{in}, (b) outgoing LW radiation LW_{out} and (c) net LW radiation LW_{net} at the surface. Both AS and CS scenario are plotted.

LW_{in} and LW_{out} fluxes are strongest in summer and smallest in winter. For LW_{in} this is because the summer atmosphere is warmer (conform Equation 2.2). For LW_{out}, values in summer are higher as the temperature of the snow (surface) increases and more radiation is emitted. The seasonal cycle of LW_{out} is more pronounced than for LW_{in} and is bounded by the temperature of the snowpack, which approaches maximum 0°C in summer and thus limits further increases of outgoing LW radiation. As a result of consequently more outgoing radiation than incoming, $LW_{out} > LW_{in}$, LW_{net} is negative throughout the year for both AS and CS scenario. In other words: the AIS experiences LW cooling throughout the year and more strongly in summer.

Both LW_{in} and LW_{out} are smaller in the clear-sky scenario than in the all-sky scenario. As a result, the cloud effect on LW_{net} is positive, indicating that clouds have a net LW warming effect: CRE-LW > 0. This effect is strongest in summer mainly because the differences for LW_{out} are smaller in summer. The snowpack temperature is close to zero for both AS and CS and LW_{out} approaches its upper boundary for both scenarios.

The cloud effect on net LW radiation (CRE-LW) at the Larsen C ice shelf is: $51.6 \pm 6.5 Wm^{-2}$ in DJF, $27.1 \pm 4.6 Wm^{-2}$ in MAM, $20.0 \pm 4.3 Wm^{-2}$ in JJA, $40.1 \pm 6.3 Wm^{-2}$ in SON. Uncertainties of the fluxes are derived from the sensitivity simulations.

There is a larger spatial spread for LW_{out} than for LW_{in} as a result of larger spatial surface temperature differences. This is most noticeable in winter months. The described seasonal cycle in LW_{net} is similar for all ice shelves (appendix A.2), with $LW_{net} < 0$ throughout the year and most radiative heat lost during summer. All ice shelves yield a net cloud LW warming effect. In Table 4.2 the values for DJF are summarized. The averaged CRE-LW ice shelf wide is $46.3 Wm^{-2}$ in DJF, $24.9 Wm^{-2}$ in MAM, $21.6 Wm^{-2}$ in JJA and $31.9 Wm^{-2}$ in SON. This amounts to a yearly ice shelf wide cloud LW warming of CRE-LW = $31.1 Wm^{-2}$. Similarly to the SW radiation budget, values for spring are larger compared to fall due to the solar cycle being stronger in spring.

4.1.3. Cloud Radiative Effect

See Figure 4.3 for the net radiation budget R_{net} and the CRE at the surface of LarsenC, and Figure 4.4 for R_{net} and the CRE at all ice shelves. In Figure 4.3b a snapshot of the CRE at the Larsen C ice shelf from the 15th to the 27th of November 2007 is shown, to illustrate the daily cycle. The CRE is calculated as $CRE = R_{net,AS} - R_{net,CS}$ (Equation 2.4), where the net radiation is $R_{net} = SW_{net} + LW_{net}$ for either the AS or CS scenario.

The net radiation budget is negative throughout most of the year and positive for a short period of time in summer, for both AS and CS, at the Larsen C ice shelf and all other ice shelves. Daily fluctuations are strong in summer, alternating between daily radiative warming ($R_{net} > 0$) and nightly radiative cooling ($R_{net} < 0$). The figures show that the CRE is positive throughout the year as $R_{net,CS} < R_{net,AS}$, indicating net cloud radiative warming. The CRE is much smaller in summer because of the cooling cloud effect on SW radiation that occurs during the day (Figure 4.3b). Figure 4.3a shows that despite SW cloud blocking on average net cloud radiative warming occurs at the Larsen C ice shelf. Figure 4.4 shows that the seasonal variation is similar for

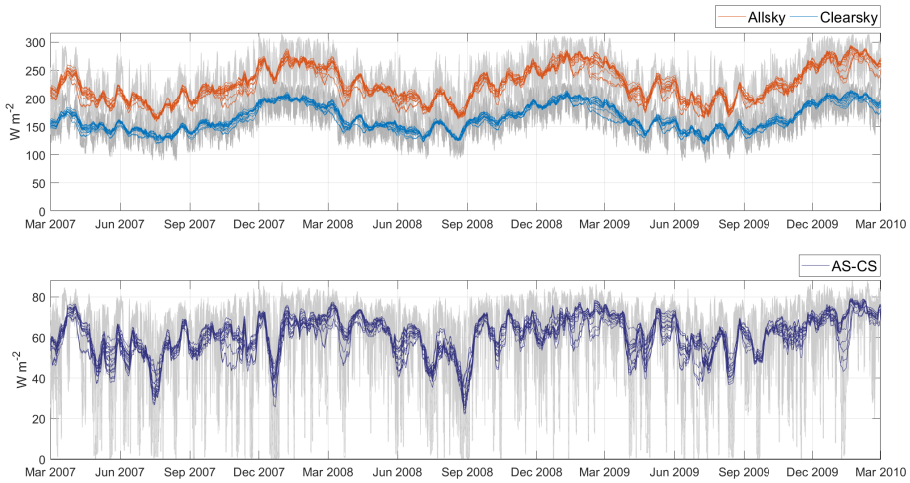

(a) Incoming LW radiation, LW_{in} at Larsen C ice shelf

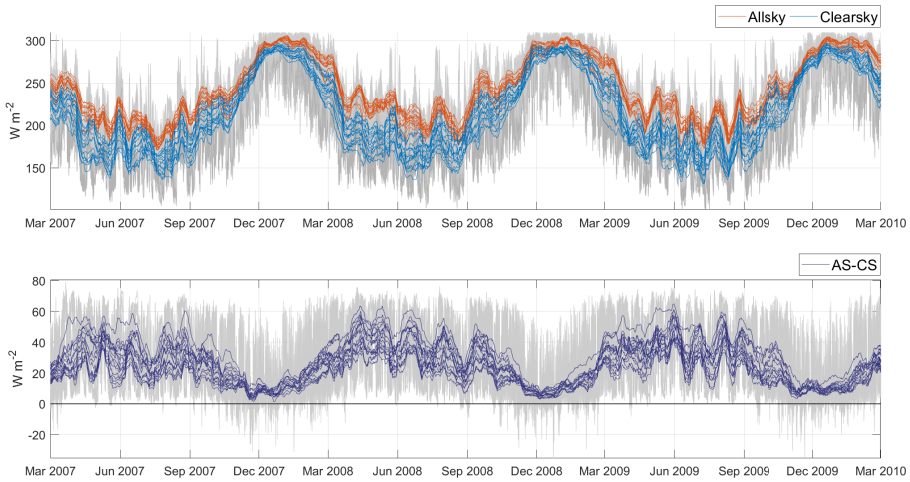

(b) Outgoing LW radiation, LW_{out} at Larsen C ice shelf

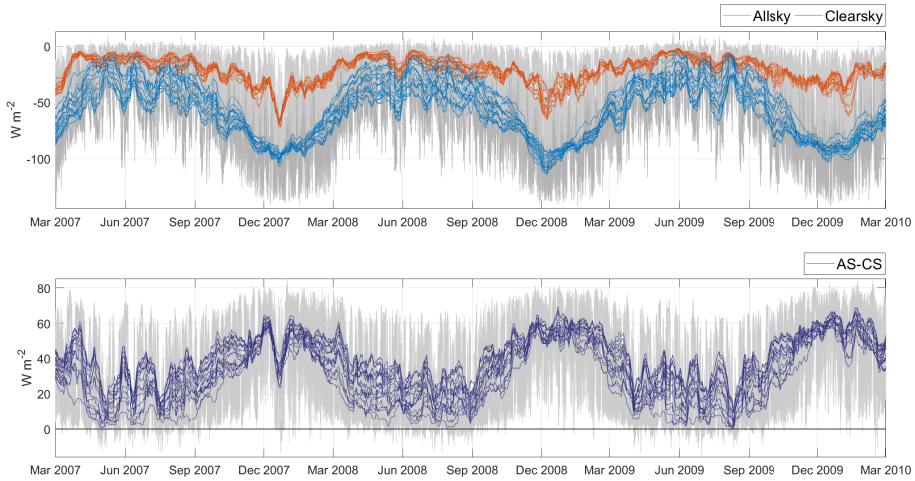

(c) Net LW radiation, LW_{net} at Larsen C ice shelf

Figure 4.2: Timeseries of LW radiation at Larsen C ice shelf. (a) LW_{in}, (b) LW_{out} and (c) LW_{net}. Each simulation gridpoint is shown (n=16) for both all-sky (AS, orange) and clear-sky (CS, blue) scenario (top figures) and the respective cloud effect (AS-CS, purple, bottom figures) with a 15-day moving average. Shaded in grey are the 3-hourly timeseries.

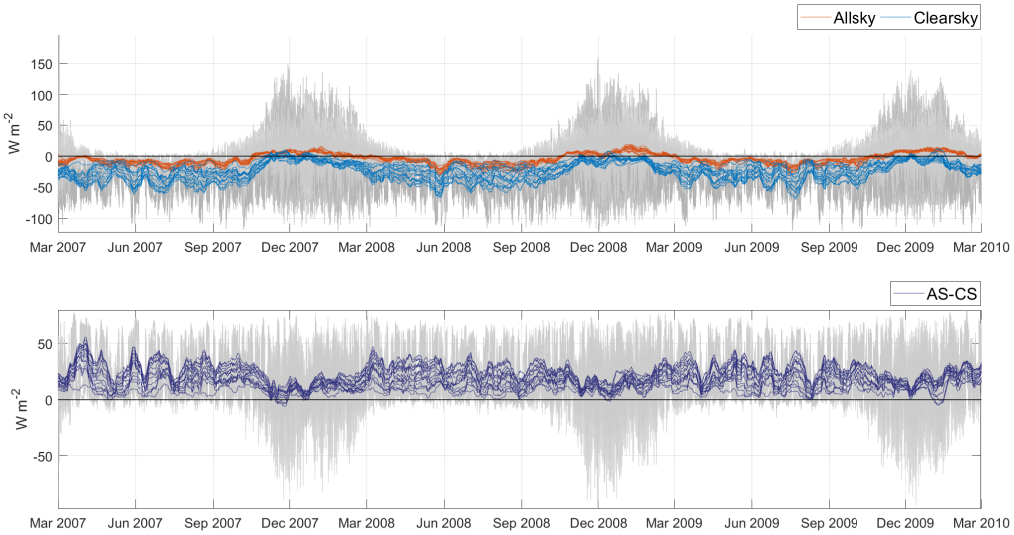

(a) Net radiation at Larsen C ice shelf with 3-hourly timeseries shaded; solid lines are 15-day moving average for all-sky (AS, orange) and clear-sky (CS, blue) (upper figure) and the cloud radiative effect (AS-CS, purple, lower figure)

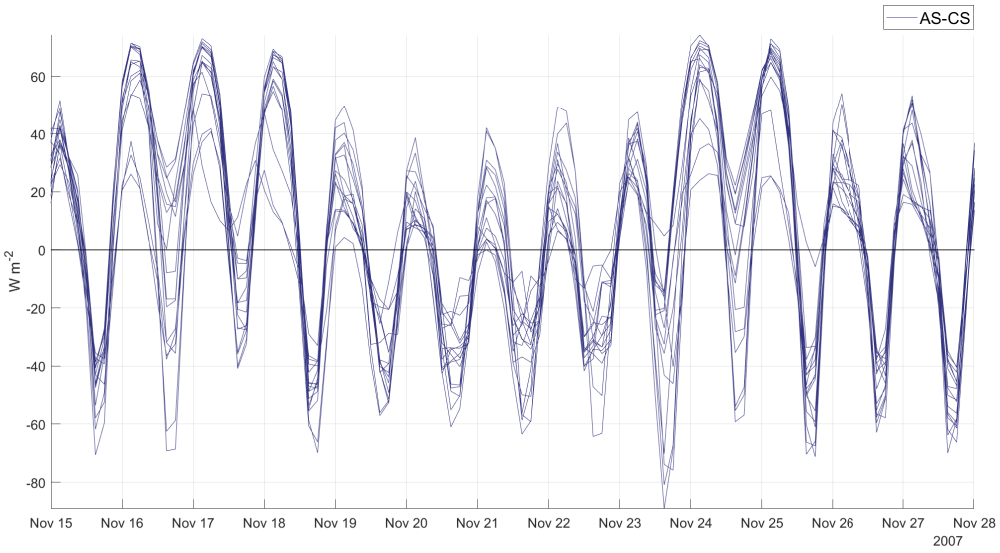

(b) Snapshot of CRE timeseries, from 15 November 2007 to 27 November 2007, 3-hourly values

Figure 4.3: Timeseries of net radiation (R_{net}) and the cloud radiative effect (CRE) at Larsen C ice shelf for (a) the complete timeseries, (b) a snapshot of the CRE to visualize the daily cycle.

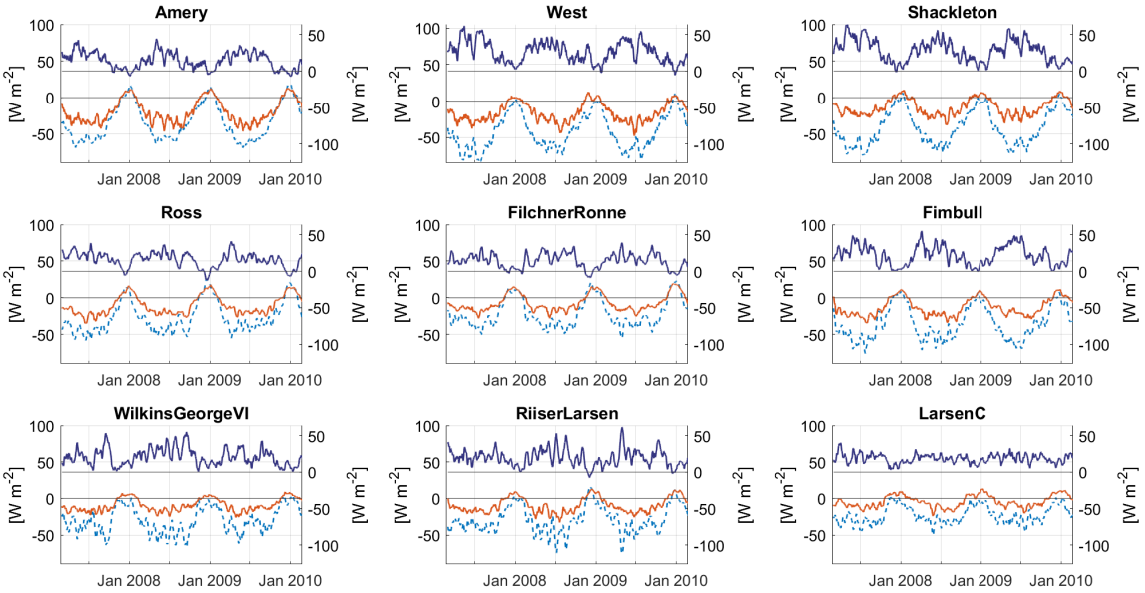

Figure 4.4: Timeseries of the cloud radiative effect (CRE) at all ice shelves. The spatial averaged timeseries is shown, visualized with a 15-day moving average. A large version of this figure is included in Figure A.3.

R_{net} (Wm^{-2})	Amery	Filchner-Ronne	Fimbull	Larsen C	Riiser-Larsen	Ross	Shackleton	West	Wilkins & George VI
All-sky	2.8	8.6	1.8	5.4	4.0	7.0	1.5	0.4	2.1
Clear-sky	-0.8	3.2	-8.5	-10.0	-5.8	0.8	-11.2	-11.5	-10.8
CRE	3.6	5.5	10.3	15.4	9.8	6.2	12.7	11.9	12.9

Table 4.3: Average net radiation R_{net} values and the CRE (Wm^{-2}) for each ice shelf during summer (DJF), averaged spatially. A more extensive table, including all seasons, is included in B.1. Uncertainties in R_{net}, retrieved from sensitivity simulations, are approximately 7.7 Wm^{-2} for DJF.

all ice shelves, but for some ice shelves a negative CRE dominates in summer. A prevailing $CRE < 0$ occurs at Amery, Ross, FilchnerRonne and RiiserLarsen, though not necessarily each year and not necessarily for a long enough period to result in a seasonal average cloud cooling effect. Regardless of the seasonal average, all ice shelves show that the CRE does become negative during the day, showing daytime cloud radiative cooling, for almost every day in November, December and January. Occasionally the daily averaged CRE is negative as well though not for longer periods of time. The minimum CRE is around 16:00 each day, the maximum around 03:00.

The averaged CRE for all ice shelves is $7.1 \pm 7.7 Wm^{-2}$ in DJF, $22.2 \pm 4.7 Wm^{-2}$ in MAM, $21.5 \pm 4.3 Wm^{-2}$ in JJA and $15.0 \pm 6.2 Wm^{-2}$ in SON. This amounts to a yearly ice shelf wide CRE of $16.5 Wm^{-2}$. Values for DJF are given in Table 4.3 and an extended table including all seasons is given in B.1. The CRE has a larger spatial spread during winter, as it correlates more strongly to the LW radiation patterns: during winter (JJA), coastal points have a stronger CRE than inland. These values also clearly show the effect of the solar cycle, reducing the CRE in spring and summer.

Figure 4.5 shows the correlation between the CRE and the cloud optical depth (τ) for each season. This figure shows that thick clouds are generally associated with positive CRE. Thin clouds are associated with the strongest occurring radiative cooling, which can be attributed to a small reflection of LW radiation but an effective blocking of SW radiation. A $CRE < -25 Wm^{-2}$ occurs almost exclusively for $\tau < 20$ (for which LWP or IWP are below $0.15 kgm^{-2}$; not shown). The figure also shows that the CRE saturates for cloud optical depths $\tau > 50$ to be 51.2 Wm^{-2} (DJF), 69.3 Wm^{-2} (MAM), $67.8 Wm^{-2}$ (JJA), 59.6 Wm^{-2} (SON) (99 percentile values). This saturation effect was expected: thicker clouds will not add any extra radiative effects after a certain threshold.

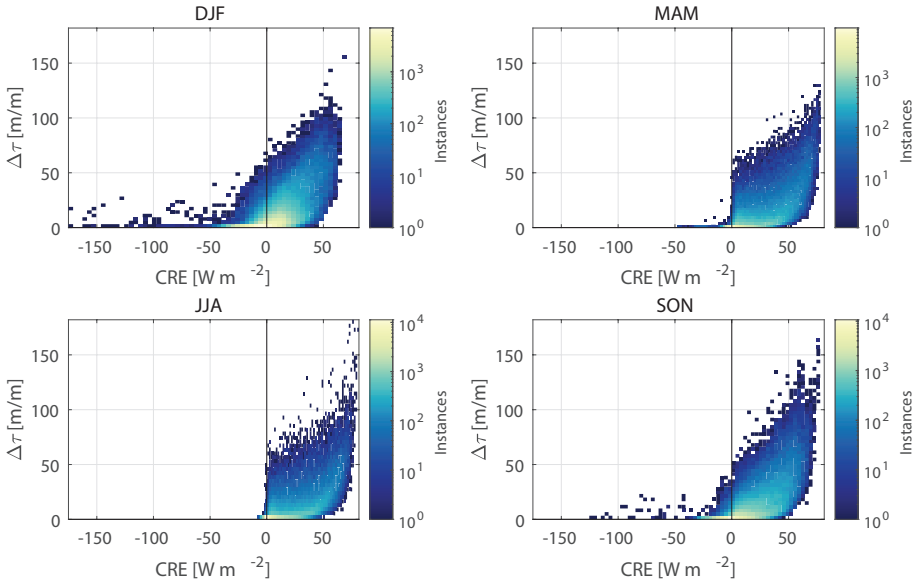

Figure 4.5: Cloud radiative effect (CRE) versus cloud optical depth (τ), separated per season. Daily average values of the three hydrological years 2007-2010 of all ice shelves are included. Colors indicate the number of occurrences for each CRE and τ combination, binned in a grid with width 4.3 Wm^{-2} and height 3.6 m/m.

albedo (-)	Amery	Filchner-Ronne	Fimbull	Larsen C	Riiser-Larsen	Ross	Shackleton	West	Wilkins & George VI
All-sky	0.836	0.837	0.853	0.875	0.853	0.841	0.866	0.860	0.862
Clear-sky	0.804	0.788	0.808	0.815	0.805	0.788	0.814	0.816	0.810
CRE	0.032	0.048	0.045	0.060	0.049	0.053	0.052	0.043	0.052

Table 4.4: Average all-sky (AS) and clear-sky (CS) albedo values and the CRE-albedo for each ice shelf during summer (DJF), averaged spatially. A more extensive table, including all seasons is included in B.2. Uncertainties of albedo values, retrieved from sensitivity simulations, are approximately 0.003 (-) for DJF.

4.2. Response of Antarctic Ice Shelves to the Cloud Radiative Effect

4.2.1. Albedo

Figure 4.6 and 4.7 show the albedo timeseries for the Larsen C ice shelf and all ice shelves. In Figure 4.6b a snapshot of the albedo evolution at Larsen C ice shelf from the 15th to the 27th of November 2007 is shown, to illustrate the daily cycle.

The figures show that the albedo is highest in winter and decreases in summer, when SW absorption starts to play a role. For the Larsen C ice shelf, the all-sky albedo (AS-albedo) decreases later in the season than the clear-sky albedo (CS-albedo), which can be attributed to the cloudiness of the ice shelf. For other ice shelves the AS-albedo decreases earlier in the season than at Larsen C, more parallel to the CS-albedo evolution. The daily cycle of the CS-albedo is very pronounced, following the daily R_{net} cycle. The daily cycle of the AS-albedo is practically absent during overcast conditions and is present during cloud-free periods (roughly 19 to 23 November in Figure 4.6b), showing a strong influence of clouds on albedo evolution. As a result, the cloud effect on the albedo either displays an evident daily cycle or is small and without daily cycle.

Overall, the cloud effect on the albedo (CRE-alb) is quite large, with impacts of CRE-alb = 0.1 in summer, indicating that it is very sensitive to cloud forcing. The cloud effect on albedo is positive: the albedo is higher in AS conditions. This indicates a stabilizing influence of clouds as for high albedo the SW absorption and subsequently melt production reduce. However, the high value of CRE-alb also indicates that there is a large potential for changes in the albedo-melt feedback.

The CRE-albedo, averaged for all ice shelves, is $0.05\pm0.3\cdot10^{-3}$ in DJF, $0.02\pm0.2\cdot10^{-3}$ in MAM, $0.02\pm0.0\cdot10^{-3}$ in JJA and $0.03\pm0.4\cdot10^{-3}$ in SON. This amounts to a yearly ice shelf wide CRE-albedo of 0.03. Uncertainties in albedo values are retrieved from sensitivity simulations. Table 4.4 gives the average values for DJF at each ice shelf and in Tabel B.2 all seasons and all ice shelves are included.

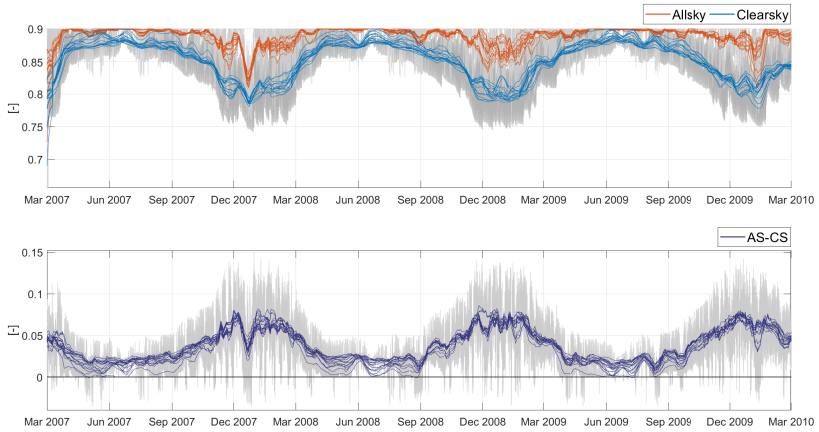

(a) Albedo evolution at Larsen C ice shelf, visualized with a 15-day moving average. 3-hourly timeseries are shown in grey.

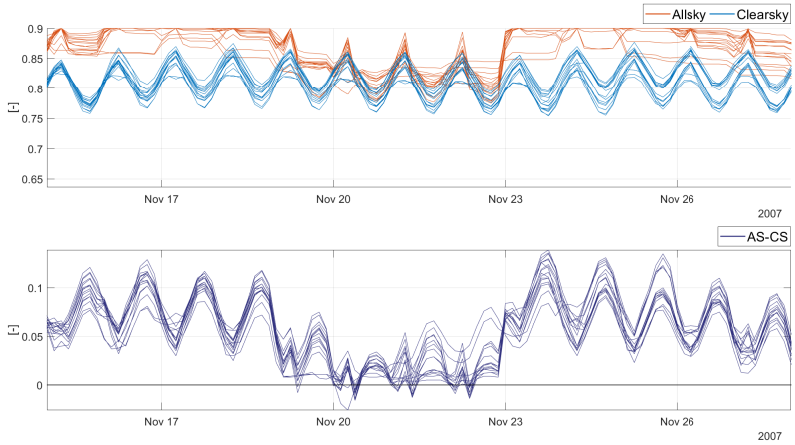

(b) Snapshot of albedo 3hourly timeseries, from 15 November 2007 to 27 November 2007

Figure 4.6: Albedo evolution at Larsen C ice shelf for (a) is the complete timeseries, (b) a snapshot of the 3-hourly timeseries to visualize the daily cycle. Values for all-sky (AS, orange) and clear-sky (CS, blue) (top figure) and the cloud effect on the albedo (AS-CS, purple, bottom figure) are shown.

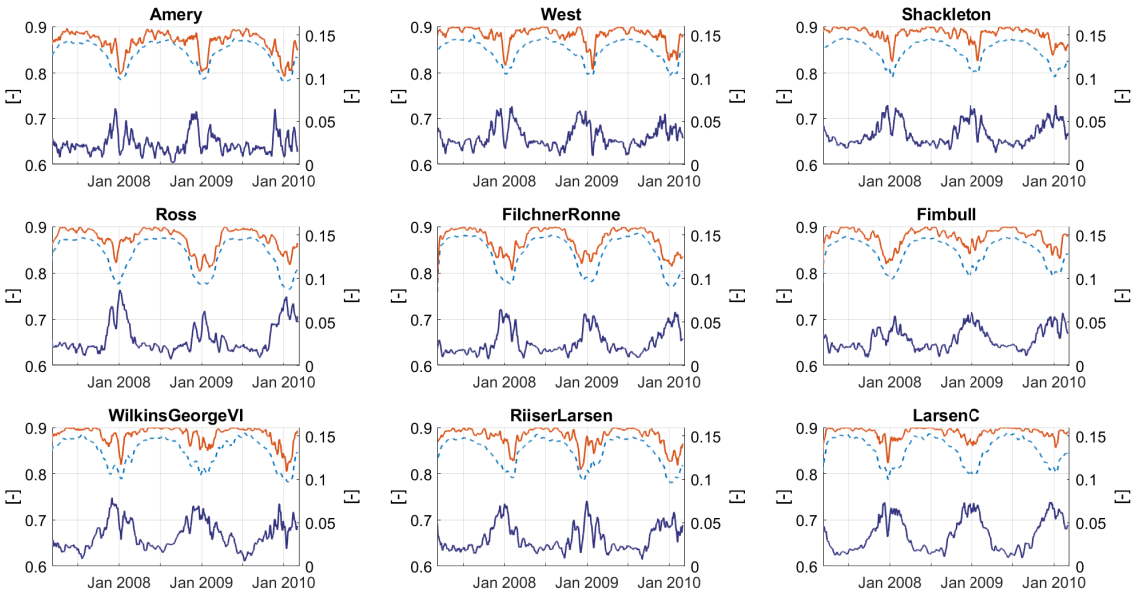

Figure 4.7: Spatial averaged timeseries of albedo per ice shelf, shown for all-sky (AS, orange) and clear-sky (CS, blue, dashed) scenario (left axis) and the cloud effect on the albedo (AS-CS, purple, right axis), visualized with a 15-day moving average. A large print of this figure can be found in A.4

4.2.2. Cold Content

The cold content (CC) is analyzed to account for the general thermal state (warmth) of the snowpack as the CC represents the amount of energy needed to warm the near-surface snow layers to 0°C.It is used in preference to the surface temperature for comparing the cloud effect on the warming of the snow profile. A negative CC corresponds to near-surface snow layer temperatures below freezing (conform equation 3.18).

In Figure 4.8 the CC is shown for the Larsen C ice shelf and in Figure 4.9 for all ice shelves, calculated for the top 0.1 meter layers of snow. Note that the CC has a daily temporal resolution instead of 3-hourly. The figures clearly show that the CC is lowest in winter (i.e. the snowpack is cold), increases in spring for both AS and CS scenario and approaches zero in summer as the snow is brought to its melting temperature.

The cloud effect on CC (CRE-CC) is strongly positive in winter, indicating that the all-sky cold content (AS-CC) is higher (warmer) than the clear-sky cold content (CS-CC), implying a cloud warming effect. The CRE-CC decreases in summer as the near-surface layers of both scenarios are close to melt. The CRE-CC, averaged for all ice shelves, is $-0.63\times10^5\,Jm^{-2}$ in DJF, $3.06\times10^5\,Jm^{-2}$ in MAM, $3.39\times10^5\,Jm^{-2}$ in JJA and $1.30\times10^5\,Jm^{-2}$ in SON. Table 4.5 gives the average values for DJF at each ice shelf and in B.3 all seasons and all ice shelves are included. The ice shelves in East Antarctica (Amery, West and Shackleton) show smaller effect of clouds on the cold content with respect to other ice shelves. This is probably because these ice shelves have generally a lower R_{net} (both AS and CS), see Table B.1. The yearly ice shelf wide CRE-CC is $1.79\times10^5\,Jm^{-2}$, indicating a yearly cloud warming effect on the cold content, but more remarkable is the summer cloud cooling effect on the cold content that is in contrast with the other seasons.

It can be seen that the strong winter cloud warming quickly disappears in spring and does not have a lasting effect on the summer cold content. At the Larsen C ice shelf a negative CRE-CC is found shortly at the end of November, indicating a period of a cloud cooling effect on the CC. At other ice shelves this seasonal behaviour is found for longer periods of time than at the Larsen C ice shelf, resulting in a summer average negative CRE-CC (cloud cooling) at those ice shelves. Generally the impact of clouds on the cold content is the same: clear-sky conditions result in very cold winter snow but relatively warmer snow in summer.

The change of cloud effects on the cold content from warming to cooling during spring indicates that the near-surface layers respond quickly to radiative forcing and especially to SW radiation, for both all-sky and clear-sky scenarios. For the upper 0.1 meter of snow, it is not surprising to find a quick response to atmospheric forcing. Nonetheless, when calculating the cold content over the top 1.0 meter snow layers, the same effects are found: a strong cloud warming effect on the cold content in fall and winter opposing spring and summer cloud cooling effects. With the exception of the Larsen C and Wilkins & George VI ice shelves, which show (slight) cloud warming effects, CRE-CC > 0, in summer. See figure A.6 in the appendix. These spatial differences are further discussed in section 4.4.

To show the value of the CC of the near-surface snow layers with respect to the snow surface temperature, a figure with timeseries of the snow surface temperature for each ice shelf is included in A.7 and a table with seasonal averages per ice shelf in B.4. It is important to notice that the surface temperature does not depict a cloud cooling effect in summer, in contrast to the CRE-CC. The cloud effect on the surface temperature is a strong warming effect in winter (5.6 $°C$ in JJA) and though it is minimal in summer (1.2 $°C$ in DJF), with cooling effects during the day (not shown), the daily averages and seasonal averages are cloud warming effects - a very similar behaviour as the CRE itself. As the surface responds more prompt to atmospheric conditions, this is not surprising. The difference with respect to the cold content lies in the propagation of the radiative forcing through the snow and the changes in snow properties. The fact that the CRE-CC is a cloud cooling effect in summer indicates that the cold content is more responsive to summer daytime cloud radiative cooling than the on average cloud radiative warming.

	Amery	Filchner-Ronne	Fimbull	Larsen C	Riiser-Larsen	Ross	Shackleton	West	Wilkins &-George VI
	$\times10^5$	$\times10^5$	$\times10^5$	$\times10^5$	$\times10^5$	$\times10^5$	$\times10^5$	$\times10^5$	$\times10^5$
All-sky	-1.95	-2.13	-0.84	-0.41	-0.64	-2.77	-1.36	-1.22	-0.65
Clear-sky	-1.32	-1.14	-0.60	-0.86	-0.47	-2.07	-1.38	-1.12	-1.34
CRE	-0.63	-0.99	-0.24	0.45	-0.18	-0.70	0.02	-0.10	0.69

Table 4.5: Average cold content (CC, Jm^{-2}) of top 0.1 meter snow in summer (DJF) at each ice shelf. Values are averaged over the three simulation years 2007-2010, and spatially averaged.

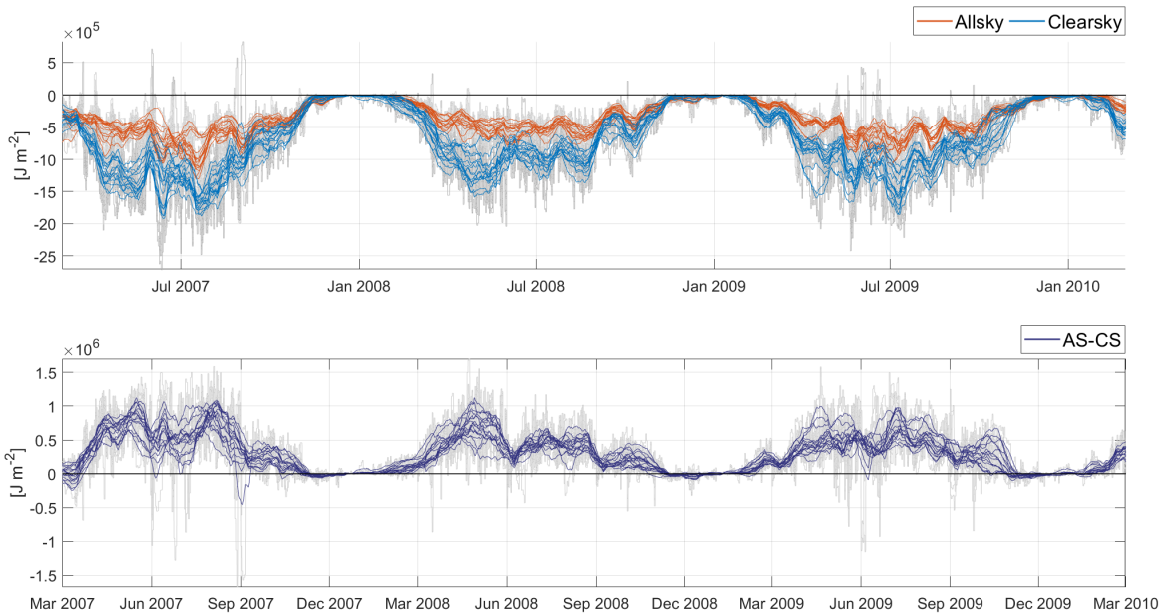

Figure 4.8: Cold content calculated over top 0.1 meter snow at Larsen C ice shelf, shown for all-sky (AS, orange) and clear-sky (CS, blue) scenario (top figure) and the cloud effect on the cold content (AS-CS, purple, bottom figure), visualized with a 15-day moving average. Daily timeseries are shown in grey.

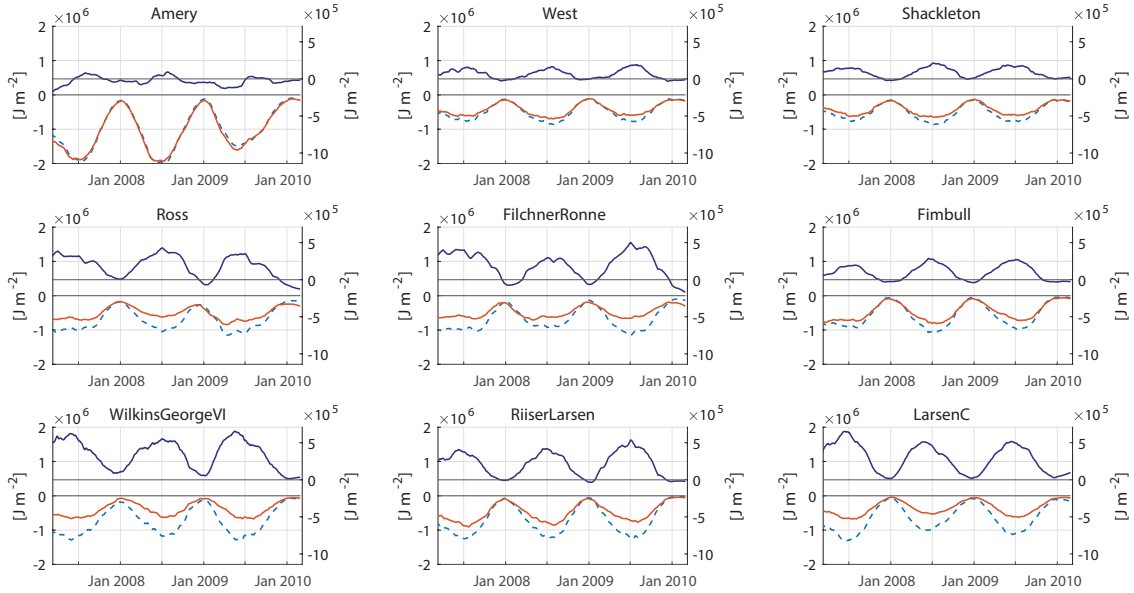

Figure 4.9: Spatial averaged timeseries of cold content (Jm^{-2}) calculated over top 0.1 meter snow per ice shelf. Shown for all-sky (AS, orange) and clear-sky (CS, blue, dashed) scenario (left axis) and the cloud effect on the cold content (AS-CS, purple, right axis), visualized with a 15-day moving average. A large print of this figure can be found in A.5.

4.2.3. Liquid Water Mass

The liquid water (liqW) mass describes the total amount of water in the snowpack at each simulation timestep (cumulative). An increase in liquid water mass is therefore an indicator for melt and is often referred to in these terms; a decrease in liqW indicates refreezing. There is no meltwater runoff simulated on the AIS; all snow that melts refreezes at some point. In Figure 4.10 and 4.11 the liqW mass is shown for the Larsen C ice shelf and all ice shelves. Due to the initialization of the simulations at each season and the cumulative timeseries of liqW, the CS scenario is reset to start with the same liquid water mass as the AS scenario. This is not necessarily a liqW mass of zero but as consequence there is a sharp jump in the clear-sky liqW and the cloud effect on liqW (CRE-liqW), which does become zero. Visualization with a 15-day moving average smooths over this effect, resulting in only a slight 'bump'.

LiqW mass (AS and CS) is shown to increase in summer, i.e. melt occurs. The seasonal cycle starts early in summer, early December for most ice shelves, and most melt occurs before the start of January which refreezes (liqW decrease) afterwards. This is also evident when comparing seasonal average values, see Table B.5: multiple ice shelves yield liqW mass values in spring, all in summer and none in winter. Only for Larsen C and Wilkins & George VI ice shelves on the Antarctic Peninsula and the Shackleton ice shelf, liqW mass is present in fall.

In clear-sky conditions, the liqW mass increases drastically with respect to AS conditions. The CRE-liqW is therefore negative, CRE-liqW < 0, translating as a cloud cooling effect on meltwater production. This is very remarkable, as net cloud radiative warming occurs ($CRE > 0$) in summer. It is also evident that melt season duration is longer for CS conditions, and starts more early in the season. At the end of summer, at the Larsen C ice shelf, the cloud effect on liquid water is positive (cloud warming) as the liquid water mass refreezes faster for CS-scenarios. This is not systematically the case for all ice shelves: only for Larsen C and Wilkins & George VI (WGVI) ice shelves.

Overall, for each ice shelf a cloud cooling effect on liqW mass is found (CRE-liqW < 0) despite cloud radiative warming in summer (CRE > 0) It is not that the melt response to cloud forcing is opposite to the CRE, but rather that it is non-linear and more sensitive to SW radiation. This is revealed when analyzing the daily fluctuations during spring and summer, see Figure 4.12: there is a lot of melt during the day, when $R_{net} > 0$ (for both AS and CS) and refreezing at night (when $R_{net} < 0$). There is a noticeable timelag of a few hours in the melt response to the radiative forcing as well. For the CS scenario, the amplitude of the daily R_{net} cycle is larger than the AS and consequently daytime cloud radiative cooling (CRE < 0) occurs for at least a part of the day. This is why (and when) clear-sky melt rates are much larger than all-sky melt. During the night, a lot of the (enhanced) melt refreezes, though not all. As a result the daily average CS liqW mass is larger than AS liqW mass, a cloud cooling effect, while the daily average CRE is, more often than not, a cloud warming effect. This shows that the short cloud cooling period during the day (where $CRE < 0$) is a strong enough catalyst for significant enhanced melt. From this, it can be stated that the melt response of the snowpack is more sensitive to changes in SW radiation than to changes in LW radiation.

In Figure 4.12 it is shown that melt occurs only for $R_{net} > 0$, but that a positive R_{net} does not necessarily mean that the available energy induces melt. This is also partially determined by the cold content of the snow: melt occurs (during the day) only when $R_{net} > 0$ and if the CC is small enough for R_{net} to supply the needed energy to warm the snowpack to 0°C. In Figure 4.13 the amount of liquid water in the snowpack is plotted with cold content, for the same two month snapshot in November and December 2007 as Figure 4.12. These figures show that the liqW mass increases when the CC is small, and that the AS and CS scenarios diverge because the clear-sky CC is generally much closer to 0 Jm^{-2}, i.e. warmer, than the all-sky CC in combination to the fact that $R_{net,CS} > R_{net,AS}$. Showing that for CS conditions a) there is more energy available during the day and b) less energy is needed to warm the snow to $0°C$, thus combining to *a lot* more melt energy for CS conditions.

In Table 4.6 the DJF seasonal average values for liquid water mass are given at each ice shelf. The ratio of increase from AS to CS is given as well, to clearly indicate that melt increases exorbitantly for CS conditions. The seasonal averaged CRE-liqW for all ice shelves is: $-16.4 \pm 6.1 kgm^{-2}$ for DJF, $0.01 \pm 0.02 kgm^{-2}$ for MAM, $0 \pm 0 kgm^{-2}$ for JJA, $-0.27 \pm 0.03 kgm^{-2}$ for SON. Naturally there is no CRE-liqW mass during winter. On a yearly basis, the cloud effect on liquid water mass is a reducing effect, CRE-liqW = $-4.1 kgm^{-2}$. Uncertainties are derived from the sensitivity simulations. Translating seasonal averages and seasonal uncertainties to a yearly mass component (by multiplying each grid box by its relative area), the CRE-liqW mass is on average CRE-liqW = $-23.9 \pm 10.3 Gtyr^{-1}$, ice shelf wide. Though the liquid water mass is not simulated as a mass loss component, the effect of clouds is not insignificant in magnitude compared to the derived Antarctic ice sheet wide mass loss of $183 \pm 94 Gtyr^{-1}$ between 2008 and 2015 by Gardner et al. [2018].

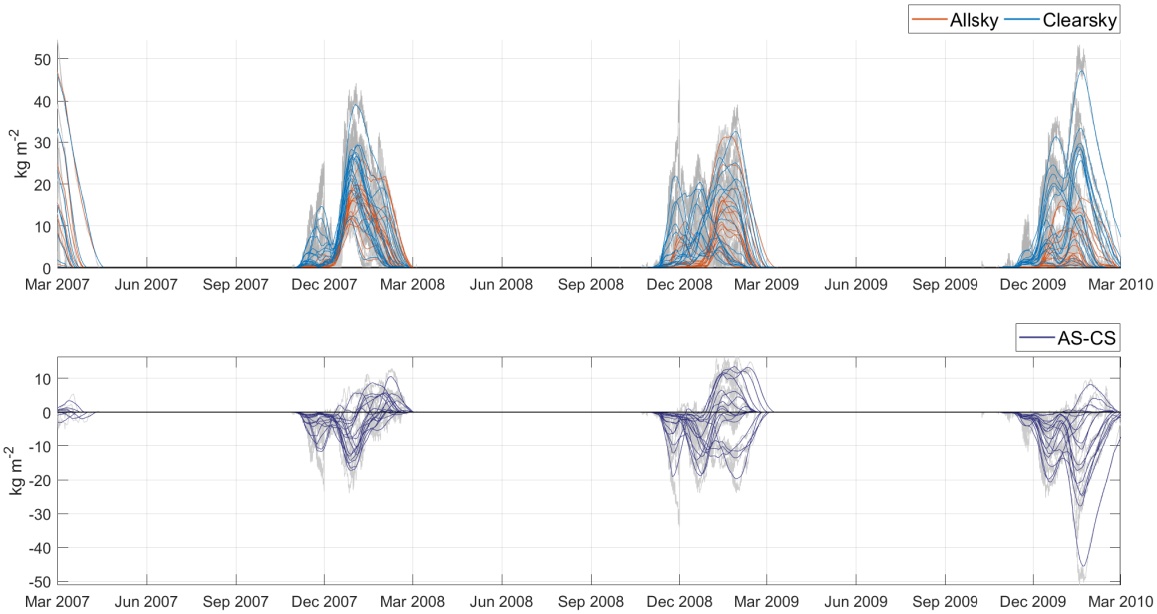

Figure 4.10: Cumulative timeseries of liquid water mass (kgm^{-2}) at Larsen C ice shelf, shown for all-sky (AS, orange) and clear-sky (CS, blue) scenario (top figure) and the cloud effect on the liquid water mass (AS-CS, purple, bottom figure), visualized with a 15-day moving average. 3-hourly timeseries are shown in grey. During the initialization of each seasonal simulation, the cumulative value is set to 0, resulting in the jumps visible at the start of December.

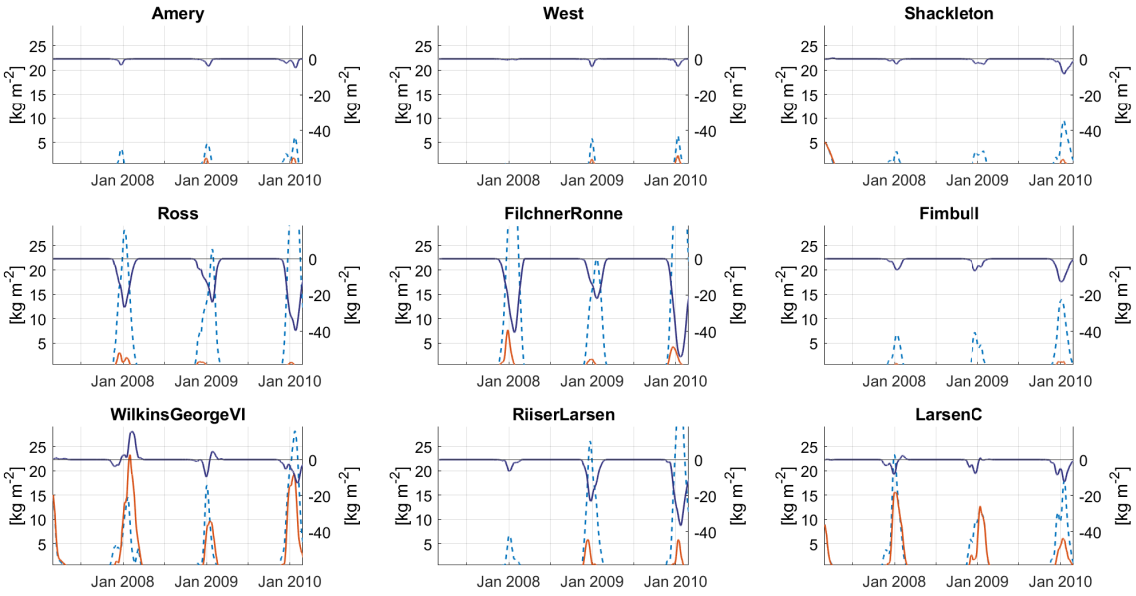

Figure 4.11: Cumulative timeseries of liquid water mass (kgm^{-2}) at all ice shelves. The spatial averaged timeseries is shown for all-sky (AS, orange) and clear-sky (CS, blue, dashed) scenario (left axis) and the cloud effect (AS-CS, right axis), visualized with a 15-day moving average. A larger print of this figure can be found in the appendix figure A.8.

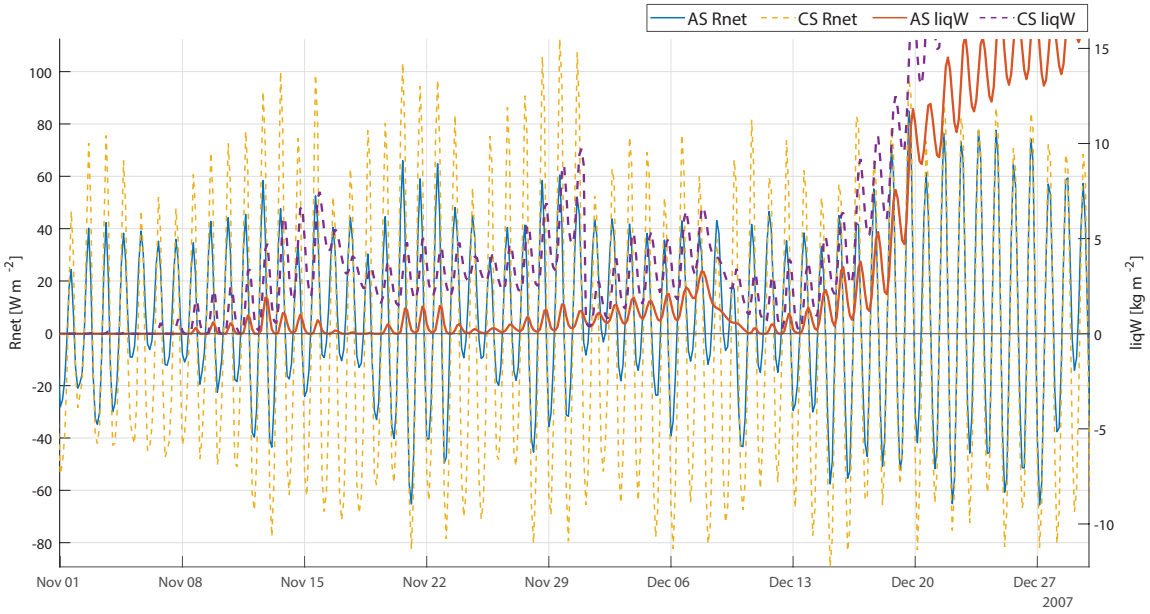

Figure 4.12: Snapshot of the spatial averaged daily cycle of net radiative flux (R_{net}, left axis) and liquid water mass (liqW, right axis) at Larsen C ice shelf for both all-sky (AS, solid lines, blue for R_{net}, orange for liqW) and clear-sky (CS, dashed lines, yellow for R_{net} and purple for liqW).

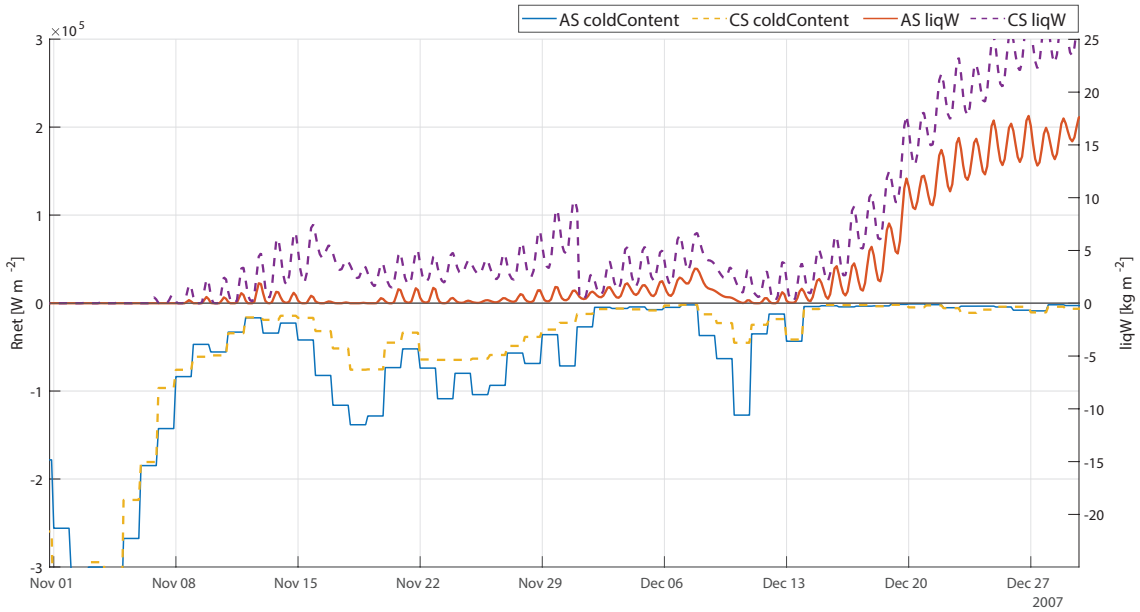

Figure 4.13: Snapshot of the spatial averaged cold content (CC, left axis) and liquid water mass (liqW, right axis) timeseries at Larsen C ice shelf for both all-sky (AS, solid lines, blue for CC, orange for liqW) and clear-sky (CS, dashed lines, yellow for CC and purple for liqW). LiqW mass has a 3-hourly temporal resolution whereas the CC has a daily resolution.

	Amery	Filchner-Ronne	Fimbull	Larsen C	Riiser-Larsen	Ross	Shackleton	West	Wilkins & George VI
All-sky	0.3	1.6	0.4	5.4	1.1	0.7	0.3	0.3	9.0
Clear-sky	1.5	25.7	4.4	8.6	12.3	17.8	2.4	1.1	9.6
CRE	-1.2	-24.1	-4.1	-3.2	-11.2	-17.0	-2.1	-0.8	-0.6
ratio CS/AS	7.9	18.8	11.3	1.5	12.8	38.6	6.6	3.6	1.1

Table 4.6: Average liquid water mass (liqW, kgm^{-2}) values in summer (DJF) at each ice shelf. Values are averaged over the three simulation years 2007-2010, and spatially averaged. Uncertainties are approximately $\pm 6.13 kgm^{-2}$ in DJF.

Notable is that the CRE-liqW differs a lot between ice shelves. The CRE-liqW is especially large for ice shelves with low liqW mass in the AS scenario. Larsen C and Wilkins & George VI ice shelves on the Antarctic Peninsula show a relatively small increase of liqW mass for CS conditions: a ratio of 1.5 and 1.1 with respect to more than tenfold enhanced liqW mass at other ice shelves. This can be explained by the feedback of meltwater on the snow: meltwater warms the snow and increases the cold content, which increases its potential for further melt. At the Larsen C and Wilkins & George VI ice shelves, this feedback warming of the snow by meltwater occurs in both AS and CS scenario. On the other ice shelves, all-sky liqW mass is small, thus the feedback of meltwater warming the snow is almost absent. As the liqW mass increases in the clear-sky scenario due to high daytime R_{net}, the cold content increases and so the meltwater warming feedback enhances melt rates even more compared to all-sky conditions. This also explains why a cloud cooling effect on the CC is found for all ice shelves, the snow being warmer due to increased meltwater heat transfer in clear-sky conditions, except at Larsen C and Wilkins & George VI.

4.2.4. Sensible Heat Flux

The turbulent sensible heat (SH) flux is governed by temperature differences between the atmosphere and the surface ($\Delta T = T_{2m} - T_{sfc}$). See Figure 4.14 for SH values at the Larsen C ice shelf and Figure A.9 in the appendix for each ice shelf. Temporal variability is very similar for all ice shelves.

During winter radiative cooling ($R_{net} < 0$), heat loss is compensated by a SH flux to the surface. For clear-sky scenarios, a larger wintertime SH flux is simulated, agreeing with previous research of Van Den Broeke et al. [2005], enhanced by the stronger LW radiative heat loss and lower snow temperature. Spatial variations are more pronounced in winter, correlated with variations in LW radiation (not shown). In summer, a negative SH occurs during the day for a few occasions as the surface loses heat to the atmosphere. For every occasion this is compensated by a positive SH flux resupplying heat during the night.

4.2.5. Latent Heat Flux and Sublimation

The latent heat (LH) flux describes the turbulent energy lost or gained by phase changes. A $LH < 0$ indicates heat loss, occurring for a phase change that uses energy to take place such as the transition from solid to liquid water (melt) or from solid to gas (sublimation). $LH > 0$ indicates energy that is added to the snowpack during the release of energy of phase changes such as the refreezing of liquid water or during deposition. Sublimation of the snowpack is directly derived from the latent heat flux by SNOWPACK [Lehning et al., 2002a]. Figure 4.15 shows the LH flux at the Larsen C ice shelf, Figure 4.16 the sublimation mass at the Larsen C ice shelf and Figure 4.17 the sublimation mass at all other ice shelves (b). The latent heat flux depends on the vapor pressure of the atmosphere and the surface,

$$LH = \beta(e_A - e_S), \tag{4.1}$$

thereby indirectly depending on the temperature difference of the atmosphere and the surface ($\Delta T = T_{2m} - T_{sfc}$). If ΔT increases, the latent heat flux increases.

Latent heat loss is simulated throughout the year for AS conditions (AS-LH < 0) and subsequently sublimation is simulated throughout the year. This is enhanced during summer, when more excess energy is available and melt occurs, thus losing more energy through phase change processes. For CS conditions, ΔT is relatively higher as the surface is colder than for AS conditions. As a result, the clear-sky LH flux (CS-LH) is higher.

At the Larsen C ice shelf, Figure 4.15, it is shown that the winter CS-LH flux increases so much that the heat flux becomes positive. Consequently, deposition (desublimation) occurs, as can be seen in Figure 4.16. This also occurs evidently at Wilkins & George VI (Figure 4.17) and in lesser extend on a few other ice

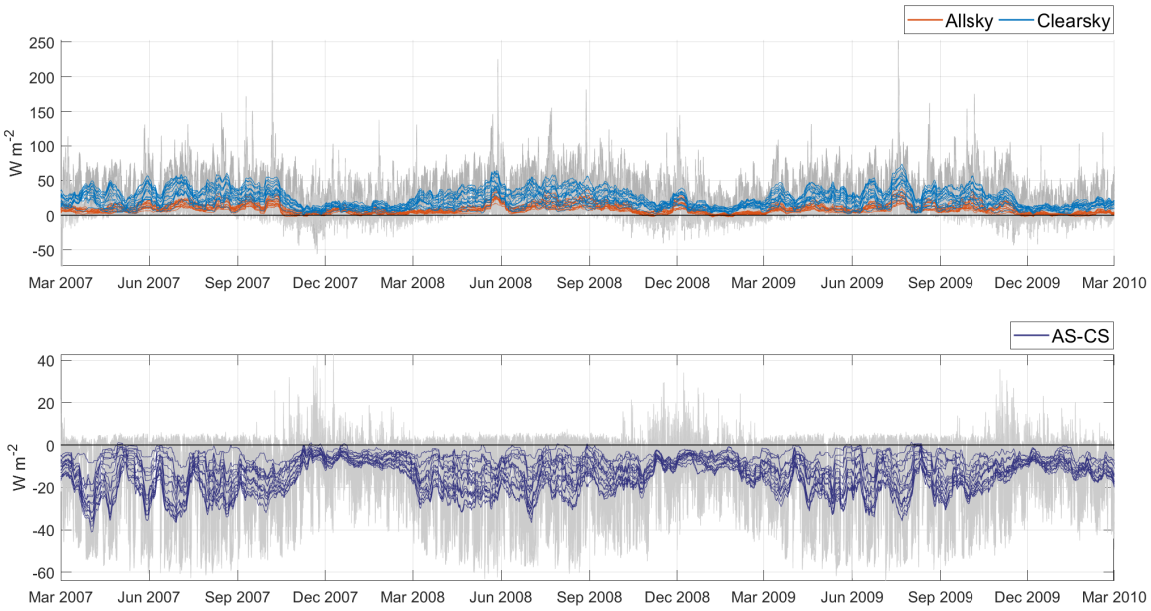

Figure 4.14: Sensible heat flux (SH) at Larsen C ice shelf, shown for all-sky (AS, orange) and clear-sky (CS, blue) scenario (top figure) and the cloud effect on the SH flux (AS-CS, purple, bottom figure), visualized with a 15-day moving average. 3-hourly timeseries are shown in grey.

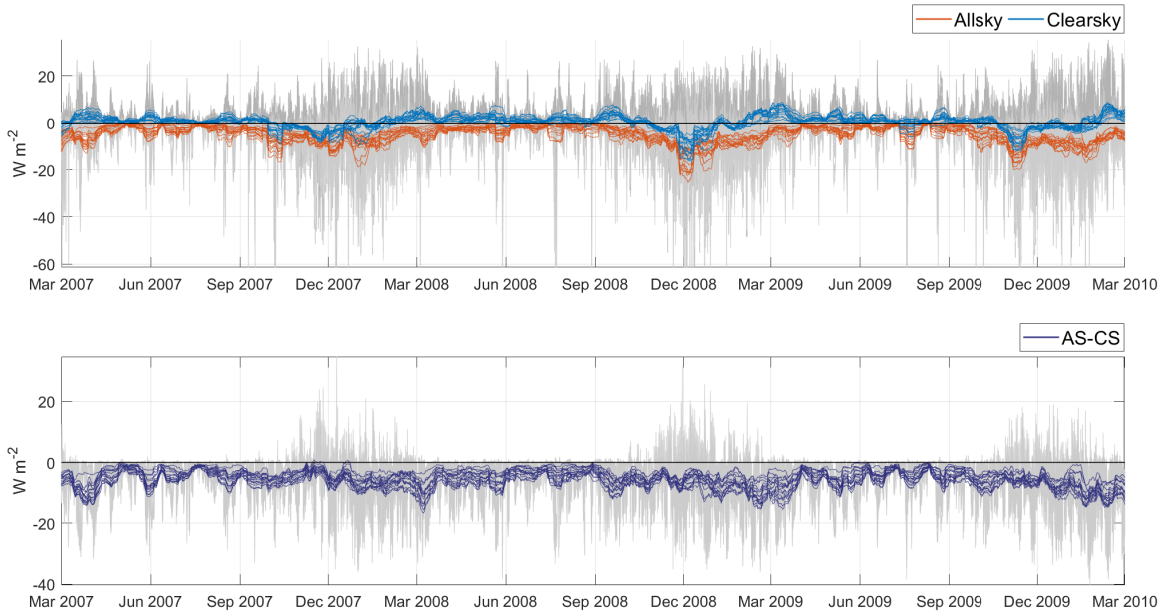

Figure 4.15: Latent heat flux (LH) at Larsen C ice shelf, shown for all-sky (AS, orange) and clear-sky (CS, blue) scenario (top figure) and the cloud effect on the LH flux (AS-CS, purple, bottom figure), visualized with a 15-day moving average. 3-hourly timeseries are shown in grey.

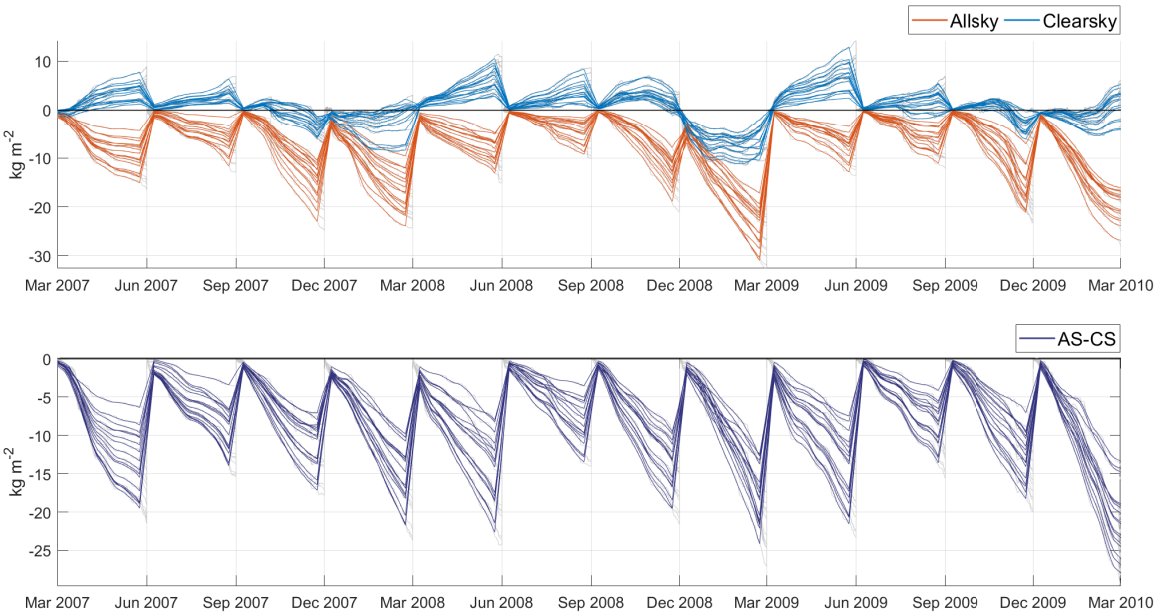

Figure 4.16: Cumulative timeseries of sublimation mass (kgm^{-2}) at Larsen C ice shelf, shown for all-sky (AS, orange) and clear-sky (CS, blue) scenario (top figure) and the cloud effect on the sublimation mass (AS-CS, purple, bottom figure), visualized with a 15-day moving average. 3-hourly timeseries are shown in grey. During the initialization of each seasonal simulation, the cumulative value is set to 0, resulting in the 'saw-tooth' shape of the figure.

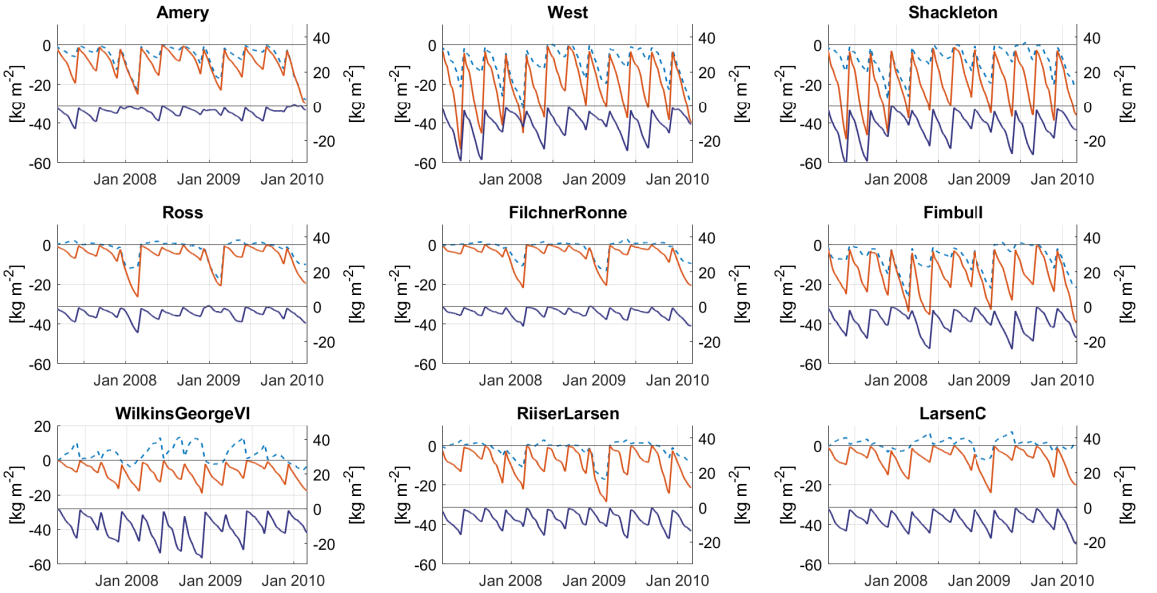

Figure 4.17: Spatially averaged Cumulative timeseries of sublimation mass (kgm^{-2}) at each ice shelf for both all-sky (AS, orange) and clear-sky (CS, blue, dashed) simulations (left axis) and the cloud effect on sublimation mass (AS-CS, purple, right axis) visualized with a 15-day moving average. During the initialization of each seasonal simulation, the cumulative value is set to 0, resulting in the 'saw-tooth' shape of the figure. A large version if this figure is included in appendix A.11.

	Amery	Filchner-Ronne	Fimbull	Larsen C	Riiser-Larsen	Ross	Shackleton	West	Wilkins & George VI
All-sky	-14.5	-12.4	-18.9	-12.0	-14.3	-13.4	-19.0	-20.8	-10.1
Clear-sky	-13.1	-7.2	-13.6	-3.0	-7.8	-9.1	-12.7	-15.3	-2.3
CRE	-1.4	-5.1	-5.3	-9.0	-6.5	-4.3	-6.3	-5.6	-7.8

Table 4.7: Average sublimated mass (kgm^{-2}) values in summer (DJF) at each ice shelf. Values are averaged over the three simulation years 2007-2010, and spatially averaged. Uncertainties are approximately $\pm 4.1 (kgm^{-2})$ in DJF.

shelves. Nevertheless, this seems to be the exception: most ice shelves show a CS-LH < 0 accompanied with sublimation throughout the year. For every ice shelf, the all-sky LH flux is more negative than the clear-sky LH flux, translating to more heat loss by phase changes and thus more sublimation in all-sky conditions.

In Table 4.7 average values for DJF sublimation mass are given. The seasonal averaged cloud effect on sublimation (CRE-subl) for all ice shelves is: $-5.1 \pm 4.1 kgm^{-2}$ for DJF, $-5.8 \pm 2.1 kgm^{-2}$ for MAM, $-4.4 \pm 1.1 kgm^{-2}$ for JJA, and $-4.3 \pm 2.2 kgm^{-2}$ for SON, with very little inter-seasonal variations. On a yearly basis, the CRE-subl is -4.9 kgm^{-2}. Since sublimation is a mass-loss term, sign convention translates such that a CRE-subl < 0 indicates that clouds enhance sublimation, i.e. mass loss. Uncertainties are derived from the sensitivity simulations.

Converting seasonal averages and seasonal uncertainties to a yearly mass component (by multiplying each grid by its relative area), the cloud effect on sublimation mass is $-34.7 \pm 15.6 Gt/yr$. This indicates higher mass loss values for AS conditions, a cloud warming effect. It is in the same order of magnitude as the cloud effect on liquid water mass.

4.3. Spatial variations of Cloud Radiative Effect

The cloud radiative effect (CRE) shows a spatial pattern where the largest values for $CRE > 0$ occur at the coastal zones of each ice shelf, showing strongest cloud warming effects. The spatial pattern of the CRE, Figure 4.18, is consequent for each season, though with more contrasts in fall (MAM) and winter (JJA) due to stronger spatial differences in LW_{net} during those months. Gridpoints of the Ross and Filchner-Ronne ice shelf located very close to the grounding line show a smaller CRE in every season, and in DJF the seasonal average CRE is negative at those gridpoints, indicating a seasonal average cloud cooling. Though with small cooling effects with values of CRE ≈ -1 to $-2 Wm^{-2}$, this is not very remarkable.

That the spatial pattern of cloud radiative warming resembles the spatial pattern of seasonal averaged cloud optical depth, shown in figure A.12b for DJF, is self-evident. Cloud radiative warming occurs more strongly for areas with more frequent cloud cover or more optical thick clouds, or both. Spatial patterns of cloud ice and liquid water path are very similar (figure A.12c and d) and therefore do not provide any information to distinguish cloud effects for IWP or LWP. The spatial pattern of the CRE furthermore correlates with warmer atmospheric temperatures and higher wind speeds (also provided in Figure A.12). This agrees with the SEB study of Van Den Broeke et al. [2005] that associated strong winds on the ice shelf with overcast conditions, and thus indirectly with strong cloud radiative effects.

4.4. Spatial variations of Surface Response to Cloud Radiative Effect

Figure 4.19 compares spatial patterns of the CRE (a) and RACMO wind speeds (b) in DJF to the cloud effect on albedo (c), cloud effect on cold content (d), cloud effect on liquid water mass (e) and the cloud effect on sublimation mass (f). Spatial patterns of other RACMO atmospheric parameters in DJF (atmospheric temperature, cloud optical depth, cloud ice and liquid water path, wind speeds and relative humidity) are included in appendix A.12.

Spatial correlation between CRE and snow parameters is generally high: coastal zones of each ice shelf are subject to the strongest cloud radiative warming (CRE > 0) and yield the strongest cloud warming effect on the albedo and sublimation or the smallest cloud cooling effect on the cold content and liquid water mass.

For the albedo, figure 4.19c, a strong positive cloud effect indicates that in these areas the all-sky albedo is relatively much higher than the clear-sky albedo. It can be stated that these areas are more prone to changes in albedo values due to changes in cloud forcing. Similarly, a strong positive cloud effect on the sublimation mass, figure 4.19f, indicates that these areas have more sublimated mass for all-sky conditions with respect to clear-sky and have higher potential for changes in sublimation values due to changes in cloud forcing.

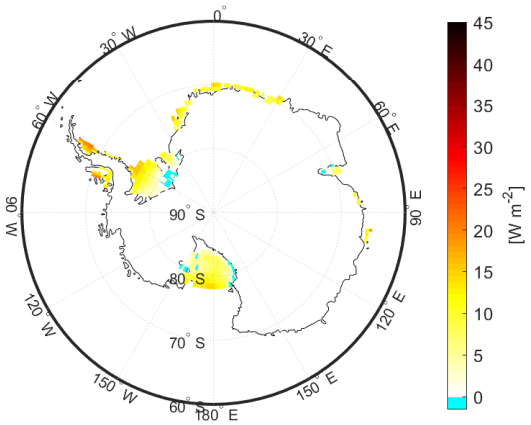

(a) DJF

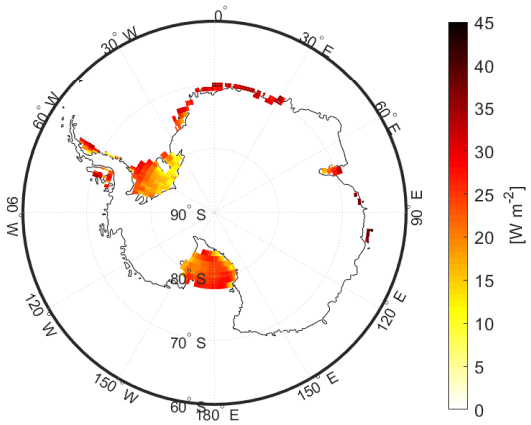

(b) MAM

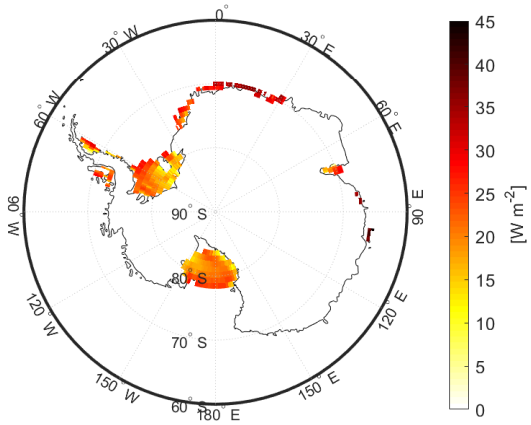

(c) JJA

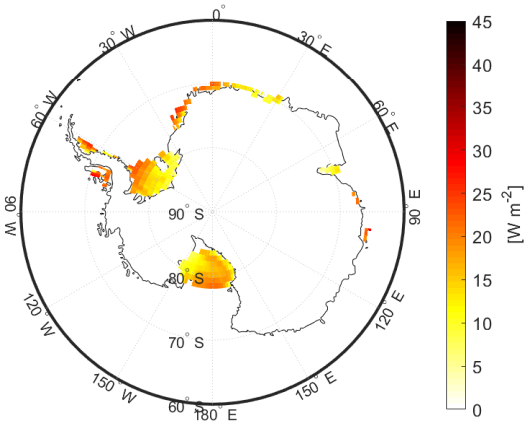

(d) SON

Figure 4.18: Cloud radiative effect (CRE, Wm^{-2}) averaged for (a) summer (DJF), (b) fall (MAM), (c) winter (JJA) and (d) spring (SON). Colorbar values are the same for all figures, though not all have values below 0.

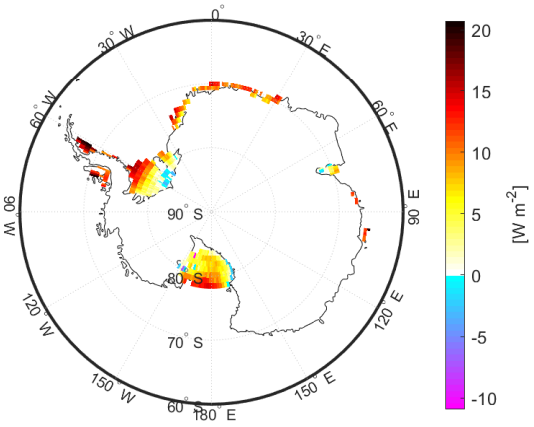

(a) CRE, Cloud Radiative Effect (Wm^{-2})

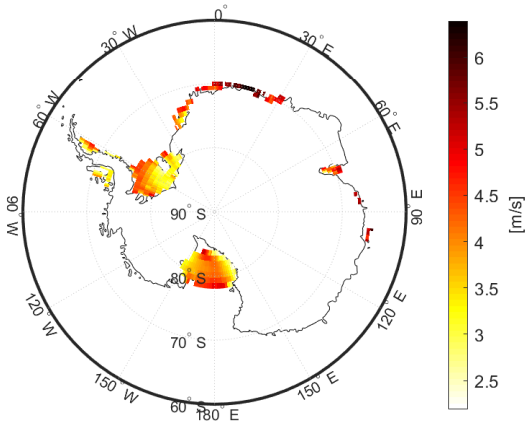

(b) Wind speed (ms^{-1})

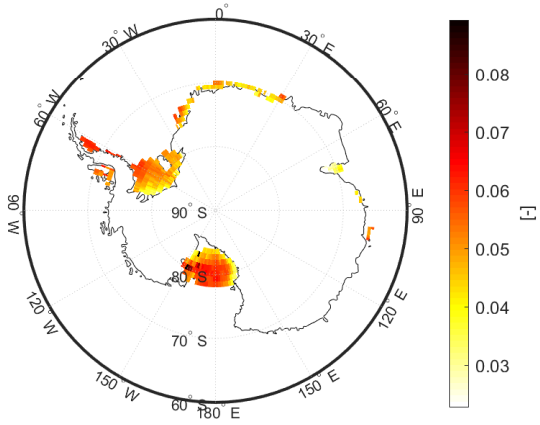

(c) CRE-albedo, cloud effect on albedo (-)

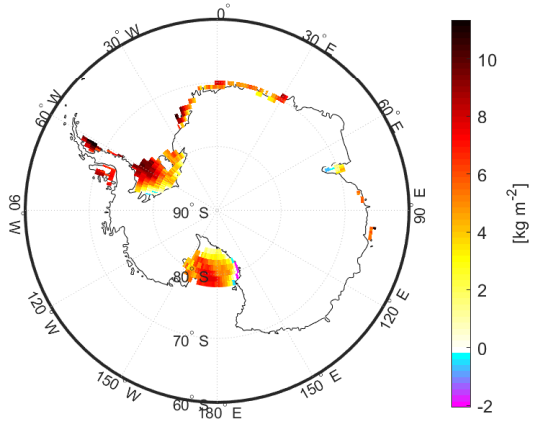

(d) CRE-subl, cloud effect on sublimation mass (kgm^{-2})

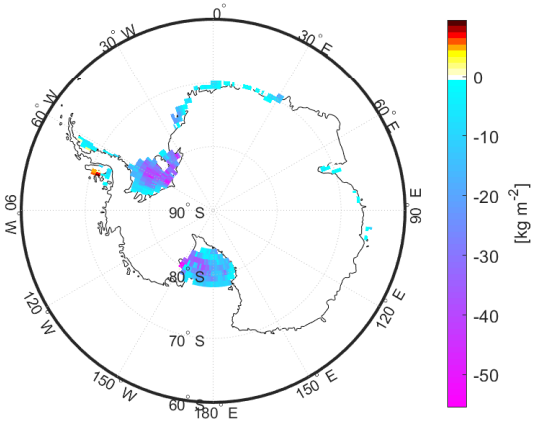

(e) CRE-liqW, cloud effect on liquid Water Mass (kgm^{-2})

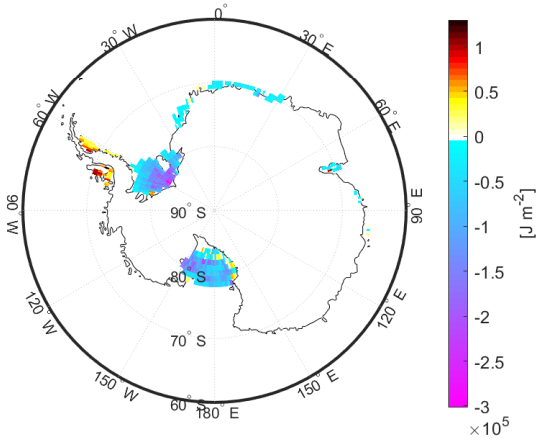

(f) CRE-CC, cloud effect on cold content (Jm^{-2})

Figure 4.19: Spatial variations of (a) the cloud radiative effect (CRE), (b) wind speed and the cloud effect on each snow parameter (c to f) for summer (DJF) seasonal average values. High positive values indicate cloud enhancement of that parameter. For this reason the cloud effect on sublimation is visualized with a switched sign convention, to match colorbars intuitively (positive values in this figure indicating that the all-sky scenario has more sublimation; i.e. more mass loss).

Where the CRE is relatively high, the cloud effect on the cold content is relatively high as well. For most ice shelves this means that the CRE-CC is less negative, or in other words: in areas with relatively strong cloud radiative warming, the cloud cooling effect on the cold content is smallest. At the Larsen C and Wilkins & George VI ice shelves a summer cloud warming effect on the CC is found in contrast to cloud cooling on the other ice shelves, which is likely not only attributed to the strong CRE at these ice shelves but also to the much higher atmospheric temperatures that characterise the Antarctic Peninsula (Figure A.12a). Note that a cloud cooling effect on the cold content only occurs in summer (recall Figure 4.9); during other seasons a CRE > 0 corresponds to a cloud warming effect on the cold content (CRE-CC > 0) with similar spatial patterns (not shown).

The cloud effect on liquid water mass is negative (cloud cooling effect) as a result of daily negative CRE (cloud cooling) values which are not directly represented in the seasonal averaged figure. Relatively more frequent or stronger daytime cloud cooling is indirectly represented by a relatively small, but positive, seasonal averaged CRE value. Under the circumstances of strong daytime cooling, i.e. an averaged low CRE, the cloud effect on liqW is a strong cloud cooling effect (CRE-liqW < 0). Spatial patterns agree to this: the figure shows that areas with weak cloud radiative warming correspond to areas with very strong cloud cooling effects on liquid water mass. Or vice versa, the areas with strongest cloud radiative warming show smallest cloud cooling effects on liquid water mass. Furthermore, note that the cloud effect on liquid water mass at the Antarctic Peninsula is a cloud cooling effect, indicating more melt for clear-sky forcing, in contrast to both a positive CRE and CRE-CC, which translates to generally warmer near-surface snow layers. This underlines the strong sensitivity of melt to (daytime) clear-sky forcing during the small window in summer where the cold content is close to zero (for both scenarios) and the difference in radiation between the scenarios is dominant over the difference in cold content.

Difference in spatial correlation to the CRE are found for the interior of Ross and Filchner-Ronne ice shelves, which show a stronger sensitivity to cloud radiative forcing than their surroundings that have similar forcing. This change is likely correlated to the spatial wind patterns: areas that are subject to seasonal averaged high wind speeds show a (relative) stronger sensitivity to cloud radiative forcing. This yields a relatively stronger CRE-albedo and CRE-sublimation. The spatial correlation of CRE to CRE-liqW and CRE-CC are lower, because of their dependence on daytime CRE values instead of daily or seasonally averaged CRE values.

4.5. Sensitivity of Surface Response to Cloud Radiative Effect

4.5.1. Sensitivity to Initial Albedo

Each season, the AS and CS scenario are both initialized on the same snow profile and diverge from there on. To investigate the sensitivity of the simulation to initial snow conditions, and more specifically the albedo-SW feedback, AS and CS simulations have been performed on a snow profile with a lower initial albedo. This is done by increasing the grain radius to 5 mm. The new simulations are compared to the AS and CS simulations with the 'normal' initialization, which are henceforth referred to as the 'baseline'.

The results, shown in Figure 4.20, show that the imposed albedo bias is quite persistent: there is no visible gradual recovery to the baseline conditions (for both AS and CS) up until a snowfall event takes place. After a precipitation event the surface albedo is either partially or completely increased to baseline values (for both the AS and CS scenario).For AS conditions, the sensitivity simulation shows a stronger daily fluctuation than the AS-baseline. This can be explained due to the albedo being lower and being more sensitive to the daily R_{net} cycle than the AS baseline. For the CS scenario, both the sensitivity simulation albedo and the baseline albedo fluctuate clearly throughout the day (and thus the bias is more constant).

It is remarkable how long the imposed albedo bias propagates through time: the bias is for both AS as CS prevalent until a snowfall event. There is no perfectly objective method to quantify the longevity of the imposed albedo bias, as for each season snowfall events occur at different times. To give an approximation, the number of days the albedo bias is above 0.02 (difference to baseline) is on average 13 days with an average albedo bias in those days of 0.06 (-) for the CS scenario and 0.02 (-) for the AS scenario. The AS scenario has a lower average bias compared to the baseline partly because the new simulation fluctuates throughout the day giving minimum and maximum biases, and partly showing the stabilizing effect of clouds on the albedo. However, this stabilizing effect appears only to result in a reduction of the bias quantity and not to impact the longevity of the bias. This is important to notice, as it has a lot of influence on the impact on other parameters.

For the days that the bias occurs, the differences for other parameters are computed (baseline to sensitivity simulation), averaged for all seasons. Differences for R_{net} are -2.6 Wm^{-2} for AS and -23.9 Wm^{-2}

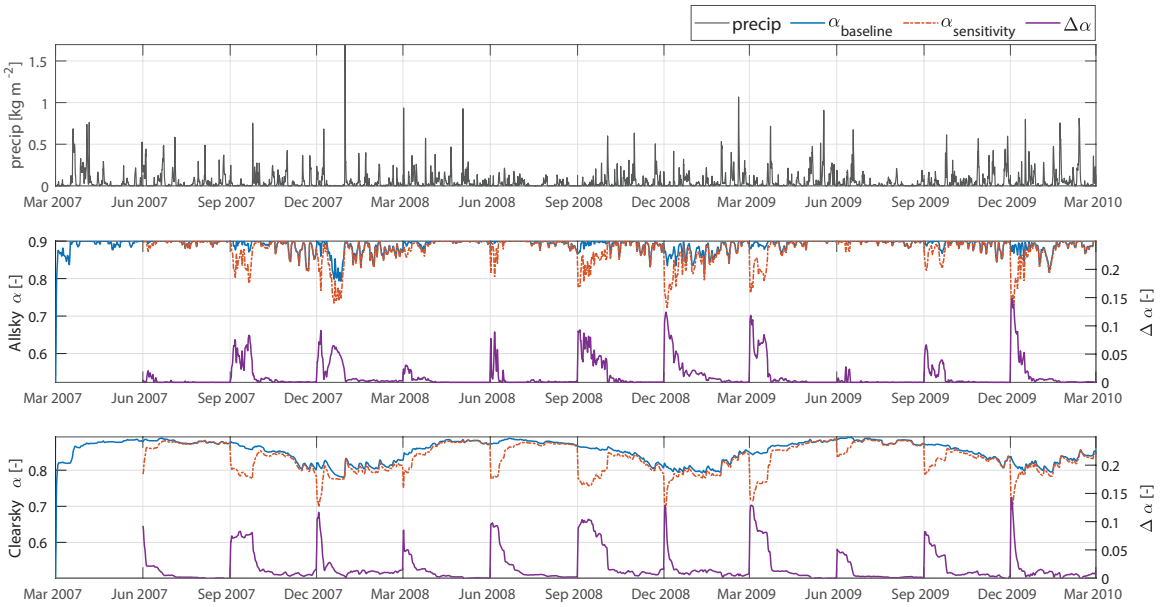

Figure 4.20: Sensitivity simulations for initial albedo. Introduced bias for sensitivity simulation (orange, dashed) versus the normal, baseline (blue, solid) simulation on the Larsen C ice shelf (left axis), spatial and daily averaged values. Top figure is precipitation (same for any simulation scenario), middle figure represents sensitivity and baseline all-sky scenario, bottom figure represents sensitivity and baseline clear-sky scenario. Difference between sensitivity and baseline simulations (right axis) show the longevity of the induced initial albedo bias, abruptly or slowly reducing due to precipitation.

for CS scenario. The sensitivity simulation with lower albedo has a higher R_{net}, as it absorbs more SW radiation. Note that the impact is 10 times larger for the CS scenario, caused by the strong enhanced SW absorption. The difference for liqW (only DJF en MAM) is -1.15 kgm^{-2} for AS, and -5.3 kgm^{-2} for CS, indicating that a lower albedo enhances melt greatly and again more so in CS conditions. The difference in sublimation is 0.31 kgm^{-2} for AS and 2.6 kgm^{-2} for CS conditions. To no surprise, this is of similar magnitude as the uncertainty in simulated sublimation values as sublimation does not depend directly on albedo changes.

Overall, the impact of the albedo bias is very large, except for sublimation. This emphasizes that the performed SNOWPACK simulations are very sensitive to (initial) albedo values. Also, the effects are much larger for CS scenario than AS scenario, indicating the strong stabilizing effects clouds have through the surface albedo or, in other words, the strength of the albedo-SW feedback.

4.5.2. Sensitivity to Radiative Flux Perturbations

Sensitivity simulations are done with perturbed all-sky LW and SW fluxes (both +10 Wm^{-2} and -10Wm^{-2} for each input timestep). The 'enhanced' and 'reduced' simulations are compared to the baseline all-sky simulations.

The impacts of the LW and SW perturbations on the LW_{net},SW_{net} ,R_{net}, albedo, liqW mass and sublimation mass are calculated and given in Table 4.8. Differences are calculated per simulated season for $LW_{enhanced}$ to $LW_{baseine}$ and $LW_{baseline}$ to $LW_{reduced}$, and these differences are averaged as both cover a flux change of $10Wm^{-2}$. Analogous for SW sensitivity. The summed value of the differences due to LW and SW perturbations gives an indication for the uncertainty of the simulations due to slight changes in SW and LW fluxes.

The $\pm10Wm^{-2}$ perturbations and their impacts on SW_{net} and LW_{net} are similar to the initial errors of the RACMO LW and SW fluxes. RACMO incoming LW flux has a bias of 8 Wm^{-2} and a LW_{net} bias of 4.5 Wm^{-2}. RACMO incoming SW flux has a bias of -5 Wm^{-2}, which is lower than the perturbed SW fluxes, but the RACMO SW_{net} bias of -2.17 Wm^{-2} is similar to the impact of the SW perturbation. These results indicate that uncertainties in initial fluxes propagate roughly linearly through SNOWPACK.

For R_{net}, albedo and liqW, the impact of LW perturbations is much larger than the impact of SW perturbations. This is remarkable, as albedo and liqW are mostly governed by changes of SW radiation.

	$\|\Delta LW_{net}\|$ (Wm^{-2})				$\|\Delta SW_{net}\|$ (Wm^{-2})			
	DJF	MAM	JJA	SON	DJF	MAM	JJA	SON
LW-perturb.	6.0	4.3	4.0	5.5	0.8	0.02	0.00	0.1
SW-perturb.	0.46	0.34	0.30	-0.8	1.40	0.78	0.60	1.00
total	6.5	4.6	4.3	6.3	2.2	0.8	0.6	1.1

(a) Sensitivity of fluxes to LW and SW perturbations

	$\|\Delta R_{net}\|$ (Wm^{-2})				$\|\Delta albedo\|$ $(\times 10^{-3})$			
	DJF	MAM	JJA	SON	DJF	MAM	JJA	SON
LW-perturb.	6.8	4.3	4.0	5.6	2.4	0.1	0.0	0.3
SW-perturb.	0.9	0.4	0.3	0.6	0.6	0.1	0.0	0.1
total	7.7	4.7	4.3	6.2	3.0	0.2	0.0	0.4

(b) Sensitivity of net radiation (R_{net}) and albedo to LW and SW perturbations

	$\|\Delta liqW\|$ (kgm^{-2})				$\|\Delta sublimation\|$ (kgm^{-2})			
	DJF	MAM	JJA	SON	DJF	MAM	JJA	SON
LW-perturb.	4.8	0.01	0	0.02	3.6	1.9	1.0	2.0
SW-perturb.	1.3	0.01	0	0.01	0.48	0.20	0.07	0.20
total	6.1	0.02	0	0.03	4.1	2.1	1.1	2.2

(c) Sensitivity of liquid water mass (liqW) and sublimation mass to LW and SW perturbations

Table 4.8: Impact of shortwave (SW) and longwave (LW) perturbations on different parameters, indicating the uncertainties with which each parameter is simulated in SNOWPACK.

Retrieved uncertainties are generally not too large to doubt the results discussed in previous sections. This can be said for LW_{net}, SW_{net}, R_{net}, albedo and sublimation; though R_{net} magnitudes might switch from positive to negative values in DJF due to their uncertainties. However, the liquid water mass shows an uncertainty that is larger than most retrieved liquid water mass values (regarding SON and DJF), which could greatly influence the observed magnitudes of the cloud effect on melt: the perturbed LW fluxes result in a 2.5 times greater liquid water mass). This puts the observed large enhanced melt for CS conditions into perspective: as SNOWPACK is apparently very sensitive for simulating different melt values the CRE-liqW is somewhat less alarming.

5

Discussion and Conclusions

5.1. Discussion

5.1.1. Limitations due to CloudSat-CALIPSO

The use of CSC observations restricted the time period for this study to 2007-2010, which is a short period to study climatological effects. The results therefore give an indication on what to expect for cloud radiative impacts on AIS conditions, but there is no real certainty in long term trends as atmospheric variability spans decades. The sensitivity to cloud radiative forcing that can be retrieved from this study, however, is enough to be able to determine the expectation that clear skies induce more melt with confidence. It is too small a time frame to say if this is a pattern that has been occurring in past years or will occur in next years, and it is too small a time frame to determine the past influence of cloud radiative impacts on ice shelf disintegration. it would be of interest to expand this study to a longer time frame, which is possible without the use of the hybrid dataset and relate the cloud radiative impact to past AIS conditions.

5.1.2. Spatial Resolution

The spatial resolution of the 1°by 1°lat/lon grid is still quite coarse. It is not possible to capture small scale topographic influences. A high spatial resolution is important for resolving the impact of the topography on the atmospheric motion in detail, realistically simulating topography-related processes such as katabatic winds and orographically forced precipitation [Genthon and Krinner, 2001]. These processes have been captured in the scope of small spatial studies such as Kuipers Munneke et al. [2012], Van Den Broeke et al. [2004], Van den Broeke et al. [2006]. They have found that clear-sky conditions coinciding with warm katabatic winds enhance the available energy for melt. General spatial patterns shown in this study agree with this response but it is not sure if this is for the same reasons. A possibility for future research would be to use the high resolution model runs of RACMO2 at 5.5km on the Antarctic Peninsula, Dronning Maud Land, the West Antarctic coast and Adèlie Land, instead of the 27 km AIS wide RACMO runs used now. This would enable to compare high resolution topography related processes to the obtained large scale patterns on an equal base. This would better align the greater spatial AIS area considered in this study with small scale, observation based studies.

5.1.3. Hybrid Dataset

Due to the insufficient performance of the hybrid dataset, simulations in this study are not observation based. There is presently not another option to incorporate observations without cutting down on temporal resolution (if the choice would be to use CSC observations) or spatial resolution (if the study would be based on AWS observations). Nevertheless, it has been shown that the RACMO model performs well enough to suit the purposes of the study and it is good to see climate models progressing so well in their cloud representation.

5.1.4. Limitations of Simulations

The SNOWPACK model is a sophisticated snow model and has been evaluated to perform very well for AIS conditions [Groot Zwaaftink et al., 2013]. Simulations are performed offline and therefore there is no

coupling between snow surface evolution and atmosphere. This enables to separate the response of the snow to different radiative forcing alone and thus suits the purposes of this study. Nevertheless, changing just the cloud radiation does impose false conditions in the theoretical clear-sky scenario. For example, precipitation is not changed and so (warm) rain adds energy to the snowpack [Lehning et al., 2002a], introducing an energy source to the radiative CS conditions which would not be present in realistic CS conditions. Also, snow and/or rain change the amount of radiation that reaches the surfaces by multiple scattering and reflections. The magnitude of these effects is expected to be smaller than the cloud radiative effect and the warming or cooling by clouds, but nevertheless might be significant. Future studies might provide insight in the impact of precipitation on the surface energy budget, which could be interesting especially as liquid precipitation (and liquid clouds) likely increases in the coming years with the warming atmosphere [Van De Berg et al., 2005].

Furthermore, performing simulations for each season provides a general seasonal quantification of the CRE. However, ongoing feedback processes in the snowpack of the CS scenario are cut-off when the snow profile is reset to an AS-initialized snowpack. This effect is noticeable for the liquid water mass and sublimation mass. However, the sublimation and melt rate of CS conditions can be seen to quickly recover to its previous rates and it is expected that the eventual seasonal CS quantification is not altered too greatly through its initialization. However, it would benefit the research if simulations were performed on different time scales to investigate this influence. Proposed are a) short-time simulations (one day to a few days) to investigate the duration of the 'recovery' after initialization, and b) simulations that span the complete melt season (e.g. November until March) to quantify how much the melt would increase for CS-scenarios more accurately.

5.1.5. Uncertainties due to Modelled Cloud Properties

The cloud representation of RACMO2.4 still encloses large biases, especially in the coastal areas and especially for LWP values (up to 0.060 kgm^{-2}) [Van Wessem et al., 2018]. Roughly stated: RACMO simulates clouds that are optically too thick, reducing biases in radiative fluxes and thus are RACMO's fluxes right for the wrong reasons. As for this study the best approximation of fluxes was required, this effect was not problematic, but nevertheless remains a problem that needs to be improved.

Furthermore, clouds are represented in RACMO as mixed clouds, which has significant influence on radiative cloud effects. Compared to layered or non-mixed clouds, mixed clouds have a strong radiative effect. Therefore, with the aim to observe the sensitivity of the surface to cloud radiative forcing, this assumption results more likely in an overestimation of cloud radiative effects than an underestimation and it is not likely that a response feedback to cloud radiative forcing will be missed. Nevertheless, it is not possibility to assign cloud effects specifically to certain types of clouds. This has not yet been a concern of this study, but might be an interesting study subject for future research. It is currently also not possible to assign an uncertainty value of fluxes introduced by the uniform cloud microphysics, as that would need to include an extensive analysis of observed cloud vertical profiles compared to their representation in RACMO. This would also be a subject for another study. In the expectation that regional climate models will improve their representation of cloud microphysics in the future, the different influence of layered clouds on the AIS surface might be studied and compared to current findings.

5.1.6. Uncertainties in Radiative Fluxes

CloudSat-CALIPSO 2B-FLXHR-LIDAR product uncertainties are 10 Wm^{-2} for LW radiation at the surface (upwelling and downwelling) and 3 to 13 Wm^{-2} for SW surface radiation upwelling and downwelling respectively [Henderson et al., 2013]. These values are uncertainties on globally and anually averaged fluxes.

RACMO2.4 has been evaluated to AWS's and CSC. For LW_{net}, the bias of monthly values compared to AWSs is approximately 4.5 Wm^{-2}; compared to CSC the downwelling LW radiation at coastal areas has a bias of approximately 8 Wm^{-2} [Van Wessem et al., 2018]. The net SW radiation has a bias of -2.17 Wm^{-2} for monthly values compared to AWSs and a downwelling SW bias of approximately -5 Wm^{-2} compared to CSC at low elevation areas. Simulated cloud radiative effects on LW_{net} and SW_{net} are much larger than these uncertainties and therefore uncertainties do impact quantitative cloud radiative effects but do not impact the qualitative conclusions.

Uncertainties for simulated net radiative fluxes in SNOWPACK are retrieved from sensitivity simulations and are approximately 7.7 Wm^{-2} (DJF), 4.7 Wm^{-2} (MAM), 4.3 Wm^{-2} (JJA) and 6.2 Wm^{-2} (SON), based on $\pm 10 Wm^{-2}$ flux perturbations. The uncertainties of the output fluxes of SNOWPACK are therefore similar to their input. Uncertainties propagate to other SNOWPACK output parameters, but are generally not very

large with respect to their observed values. Only the liquid water mass shows an uncertainty that is larger than most retrieved liquid water mass values. This influences the observed magnitudes of the cloud effect on melt significantly. However, the notion that clear-sky conditions enhance melt can be made with quite some certainty. On the one hand uncertainties in longwave radiation input can increase or decrease liquid water mass with a factor 2.5 (at Larsen C), on the other hand the melt response is shown to enhance melt in similar rates for a small decreases in albedo.

Lastly, the Neural Networks are a potential source of uncertainty for the radiative fluxes used for simulations. Fortunately, they are shown to perform exceptionally well. The errors of the SW clear-sky fluxes obtained by the NN to the CSC clear-sky fluxes are between -0.09 to 0.08 Wm^{-2} (99 percentile) which is a factor 10 to 100 smaller than the uncertainty of CSC SW fluxes themselves (3 to 13 Wm^{-2}). The uncertainty of RACMO SW fluxes is a factor 10 to 50 larger than the error introduced by the NN. The error for LW clear-sky fluxes obtained by NN compared to CSC LW clear-sky fluxes is -0.112 to 0.095 Wm^{-2} (99 percentile), also introducing an error at least 10 times smaller than the existing LW flux uncertainty (10 Wm^{-2}). However, keep in mind that the neural network yielded largest errors for small CF_{LW}, where CF_{LW} was overestimated resulting in underestimated clear-sky LW fluxes. This would yield too high CRE values. If the CRE should in reality be lower than calculated currently, the cloud effect on sublimation mass loss would be dampened and the cloud effect on liquid water would be enhanced; only further confirming the discussed impacts.

5.2. Conclusions

5.2.1. The Cloud Radiative Effect

Results show that the CRE is positive throughout the year, indicating an overall cloud warming effect. The seasonal variability shows its maximum in fall and minimum in summer. Averages of the Antarctic ice shelves per season are $7.1 \pm 7.7 Wm^{-2}$ in DJF, $22.2 \pm 4.7 Wm^{-2}$ in MAM, $21.5 \pm 4.3 Wm^{-2}$ in JJA and $15.0 \pm 6.2 Wm^{-2}$ in SON. The seasonal variability is determined by the solar cycle which is largest in spring and summer. Overall, a yearly ice shelf wide cloud radiative warming, CRE = $16.5 Wm^{-2}$, is found. However, it has been shown that spring and summer CRE values are of more importance than the general yearly values. Though clouds have a net radiative warming for each season there is a pronounced daily cycle that shows cloud radiative cooling (CRE < 0) during spring and summer daytime. This daytime cloud cooling has been shown to have a powerful impact on the surface snow conditions. Strong cloud cooling (CRE < $-25 Wm^{-2}$) occurs exclusively for optically thinner clouds ($\tau < 20$) and cloud radiative warming is shown to saturate at 69 Wm^{-2}, for a cloud optical depth of $\tau \approx 50$.

Spatial variations show a stronger CRE near the coasts of the ice shelves, correlating with higher wind speeds and warmer atmospheric temperatures and thereby agreeing with previous local studies.

5.2.2. Cloud Radiative Impact on Antarctic Ice Shelves

Though the CRE is positive on average, increasing the available energy at the surface, it is shown that melt rates are lower for all-sky conditions, a cloud cooling effect. This is through a non-linear response of the snow surface to the CRE, as melt is shown to depend more strongly on SW radiation and respond more to daytime cloud radiative cooling. During spring and summer, daytime cloud radiative cooling triggers a decrease of albedo, resulting in enhanced SW radiation absorption and increased melt rates for clear-sky conditions. This albedo-SW feedback is not balanced during the nighttime cloud warming. Thus, though clouds result in an average radiative warming effects they are a stabilizing factor for melt rates mainly by increasing the surface albedo and thereby obstructing the albedo-SW feedback.

Not only is this non-linear response interesting to find, it can also be a very strong effect: clear skies result on multiple ice shelves in more than tenfold the amount of liquid water mass. These increases are so big because meltwater rates are enhanced by the warming of the snow due to the presence of meltwater, increasing the cold content and increasing the near-surface layers potential for further melt. This is mostly effective at ice shelves with small melt rates in all-sky conditions, where the cold content is yet much lower and this warming feedback has not yet occurred. On ice shelves that have significant melt for both all-sky and clear-sky conditions (Larsen C and Wilkins & George VI ice shelves), the meltwater warming feedback is present either way and does not further enhance melt rates.

Though uncertainties in simulated liquid water mass are large, the qualitative result is quit evident. On the one hand uncertainties in longwave radiation input can increase or decrease liquid water mass with a factor

2.5 (at the Larsen C ice shelf), on the other hand the melt response is shown to increase in similar magnitude for a decreases in albedo of approximately 0.06; the latter not being an unusual occurrence due to the CRE. The simulated values result in an increase of liquid water mass in clear-sky conditions of $23.9 \pm 10.3 Gtyr^{-1}$. This is a meaningful amount, not as mass loss component but because its potential to cause hydro-fracturing and ice shelf instability.

The melt response of the Antarctic ice shelves to the CRE is in agreement with previous findings of Hofer et al. [2017], whom showed that clear skies are responsible for enhanced meltwater runoff at the GrIS (indicating a cloud cooling effect). The cloud cooling effect enhancing melt rates was also found for a short-term response of the GrIS to the CRE by Van Tricht et al. [2016b] and Izeboud et al.. However, they also found that a long-term cloud warming effect was dominant over this response and was responsible for enhanced meltwater runoff by a decrease in albedo and enhanced SW absorption; in this way preconditioning the snow for melt. This long-term effect could not be resolved for this study. Nevertheless, it has been shown that the strong winter cloud warming quite quickly reduces during spring time, suggesting that there is no lasting long-term cloud warming. It might be possible that current findings are in fact also determining the GrIS response to cloud forcing, but were overlooked. It would be possible to more equally compare results when exactly similar simulation schemes are used in future tests, such as have been suggested in the discussion.

To continue with other impacts of cloud radiation: sublimation occurs throughout the year more for all-sky conditions. The cloud radiative enhanced sublimation mass loss is with $34.7 \pm 15.6 Gtyr^{-1}$ a more direct effect on the surface mass balance than the liquid water mass, which has an undetermined effect on ice shelf instability. Because of this, the yearly average mass values of these components are not to be compared one to one. Sublimation is relatively less sensitive to cloud radiative forcing than melt, but it is more consistent for each season.

Lastly, spatial variations of cloud radiative impact on ice shelves are shown to be closely related to the strength of the CRE, which correlates to cloud cover, cloud optical depth and atmospheric temperature. Difference in spatial correlation to the CRE are found for the interior of Ross and Filchner-Ronne ice shelves, showing a stronger sensitivity to cloud radiative forcing for areas with higher wind speeds.

5.2.3. Consequences for Future Climate Scenarios

Though clouds on average have a radiative warming effect, the daytime cloud cooling effect in spring and summer is crucial for melt over the Antarctic ice shelves for both melt season start and duration as for the total liquid water mass that is produced. Hence, changes in future summer cloud conditions are an important factor for ice shelf (in)stability. If clouds were to reduce in cloud cover or thickness in spring and summer such that they result in more frequent clear skies or more frequent thin clouds, melt is expected to increase drastically. Or, if the (summer) partitioning of the cloud microphysics would shift to more liquid containing clouds, the CRE is expected to increase. This in turn could stabilize melt conditions. More frequent occurring liquid clouds are a likely expectation with the warming atmosphere, but as these clouds could stabilize melt conditions they could also increase sublimated mass.

Moreover, for generally warmer conditions the cold content decreases and thereby the potential for melt increases. Such that all-sky conditions that currently do not provide enough R_{net} for melt, might provide enough energy for melt then and thereupon gradually lose their (radiative) stabilizing ability.

Concluding, it is hard to state an expectation for future cloud radiative impacts as future cloud scenarios are not well predicted. The findings of this study pose the need to better predict this, as clouds have a potential for large impacts on the AIS mass balance that might be reassuring or alarming.

5.2.4. Recommendations

Future research can provide more insight in the observed cloud radiative impacts, as the current temporal limit of three years is not long enough to signal a trend. It would be interesting to perform a case study to investigate the past effect of cloud radiation on ice shelf instability through its impact on melt: can clear-sky enhanced melt be linked directly to ice shelf collapse in the past? Or otherwise it would be interesting to expand this study to a longer time period, to better understand cloud radiative impacts in the past.

A major contributor to better predict cloud radiative impacts for future AIS stability would be to have a better understanding of what cloud regimes are expected for future scenarios. If this would be available, a more specific quantification of cloud radiative impacts of different cloud types on the Antarctic is required as well: how much radiative warming or cooling can be related to each cloud type and subsequently how much melt and/or sublimation can be expected.

A

Figures

This appendix includes 9-tile figures for analyzed timeseries at all ice shelves. Figures are included for: SW_{net} radiation (A.1), LW_{net} radiation (A.2), the total radiation budget R_{net} (A.3), albedo evolution (A.4), cold content (A.5), liquid water mass (A.8), sensible heat flux (A.9), latent heat flux (A.10) and sublimation mass (A.11). Some of the figures have already been included in Chapter 4 and are only included here as a larger representation to improve interpretability. For some of the parameters Chapter 4 only includes figures at the Larsen C ice shelf and therefore the extended figures for all ice shelves are shown here.

Lastly, this appendix includes spatial figures (A.12) of different RACMO atmospheric variables at the ice shelves in summer (DJF).

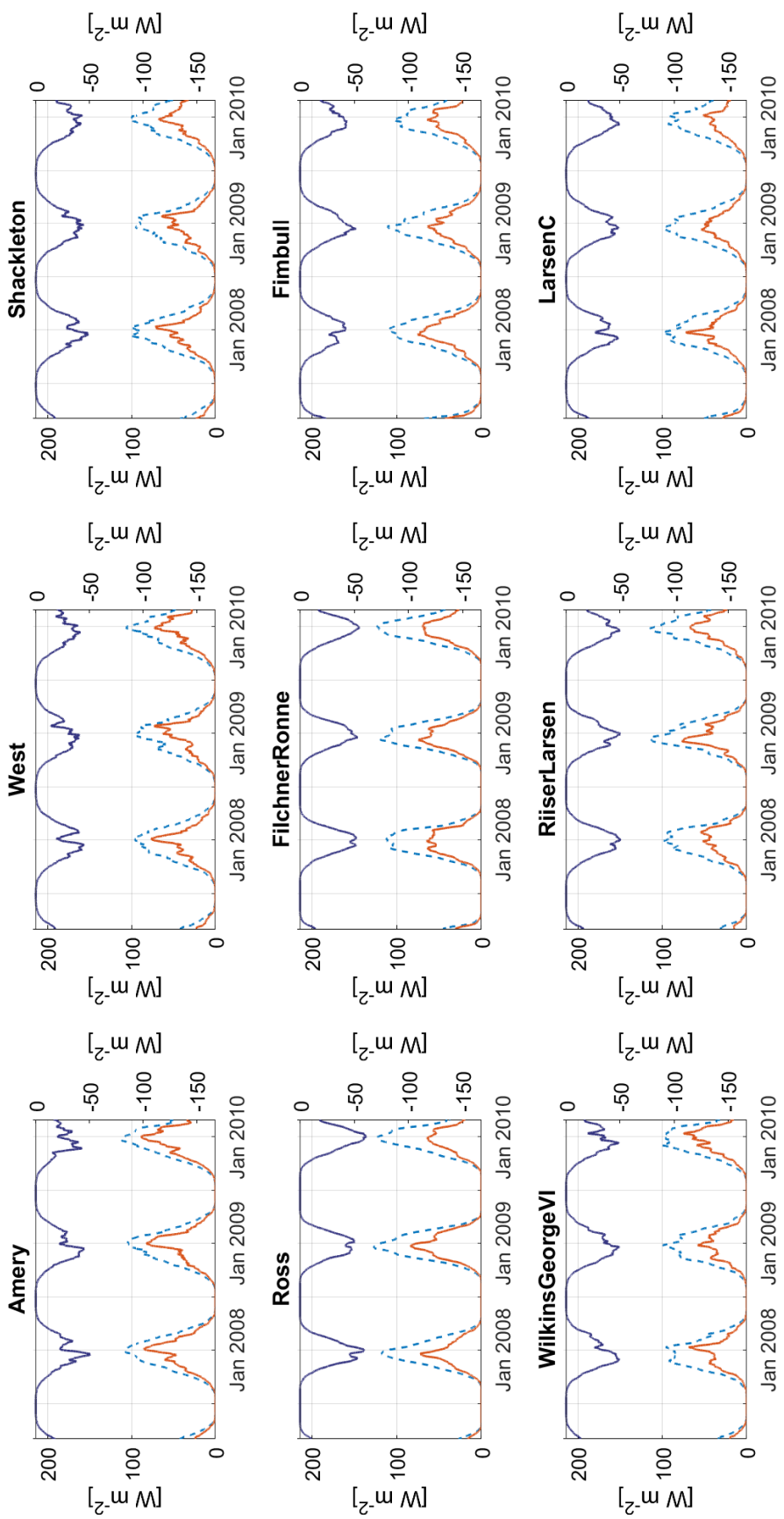

Figure A.1: Spatial averaged timeseries of net SW radiation (SW_{net}, Wm^{-2}) per ice shelf, shown for all-sky (AS, orange, solid) and clear-sky (CS, blue, dashed) scenario (left axis) and the cloud effect on SW_{net} (purple, right axis), visualized with a 15-day moving average.

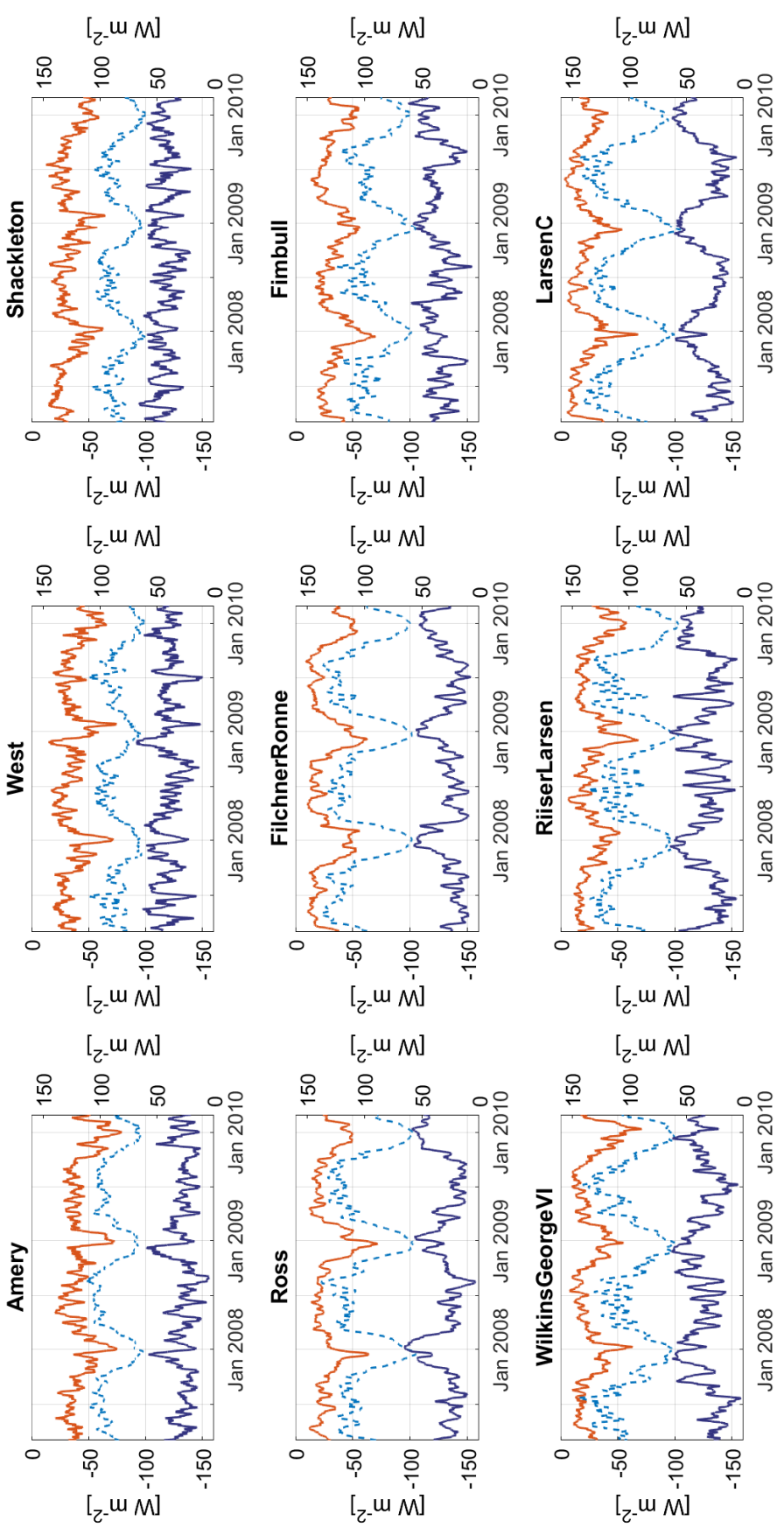

Figure A.2: Spatial averaged timeseries of net LW radiation (LW_{net}, Wm^{-2}) per ice shelf, shown for all-sky (AS, orange, solid) and clear-sky (CS, blue, dashed) scenario (left axis) and the cloud effect on LW_{net} (AS-CS, purple, right axis), visualized with a 15-day moving average.

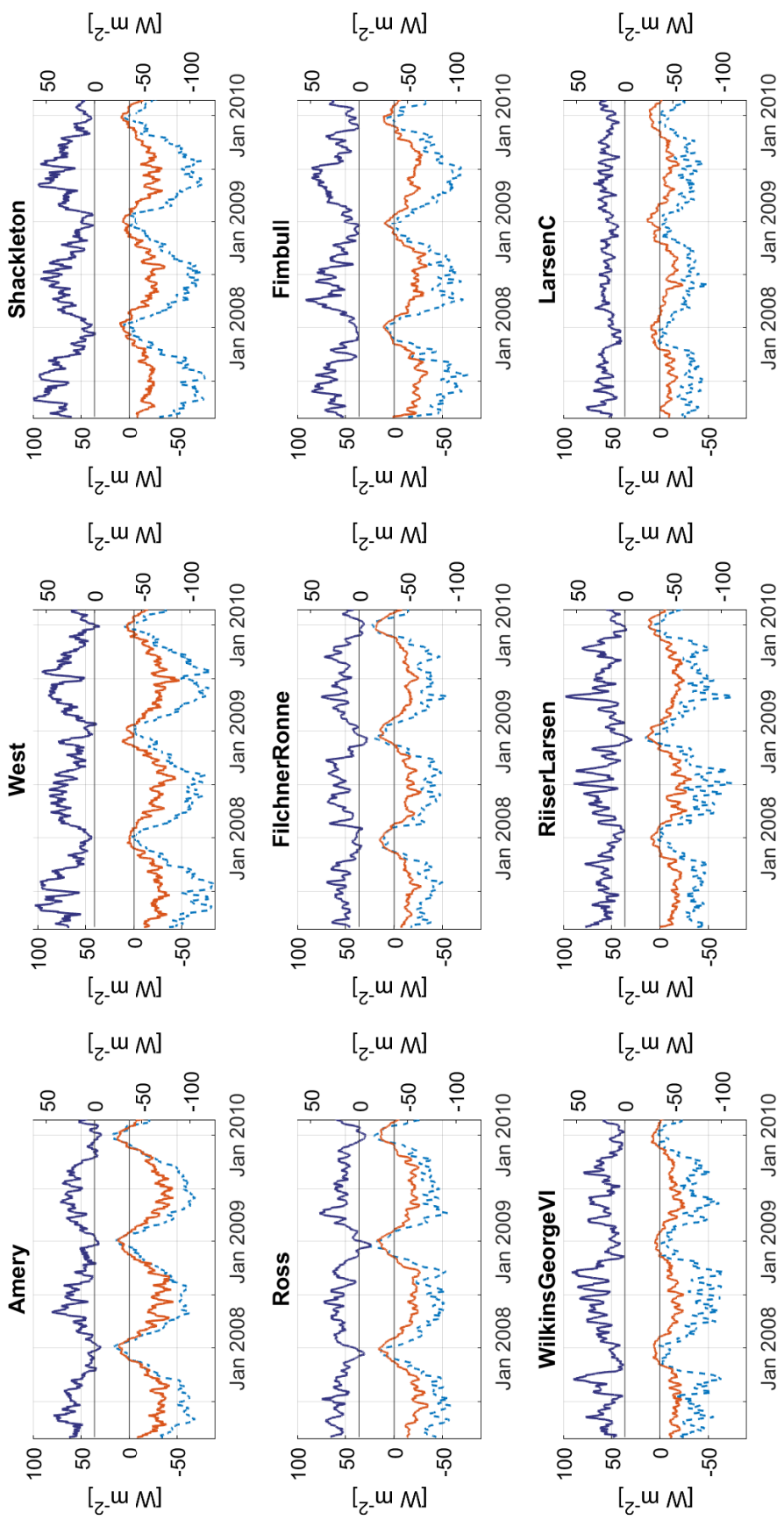

Figure A.3: Spatial averaged timeseries of net radiation (R_{net}, Wm^{-2}) per ice shelf, shown for all-sky (AS, orange, solid) and clear-sky (CS, blue, dashed) scenario (left axis) and the cloud effect on R_{net} (AS-CS, purple, right axis), visualized with a 15-day moving average.

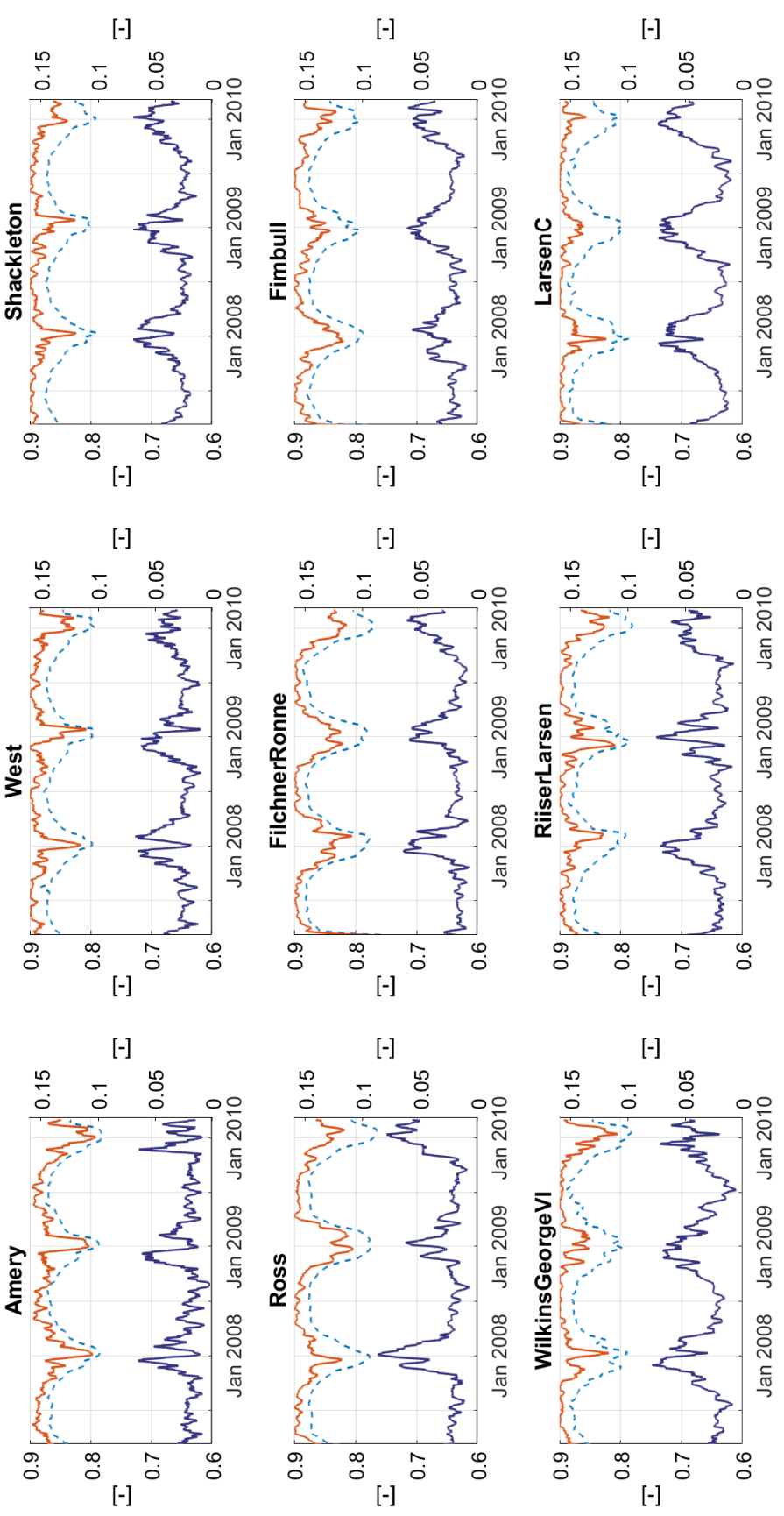

Figure A.4: Spatial averaged timeseries of albedo (-) per ice shelf, shown for all-sky (AS, orange, solid) and clear-sky (CS, blue, dashed) scenario (left axis) and the cloud effect on the albedo (AS-CS, purple, right axis), visualized with a 15-day moving average.

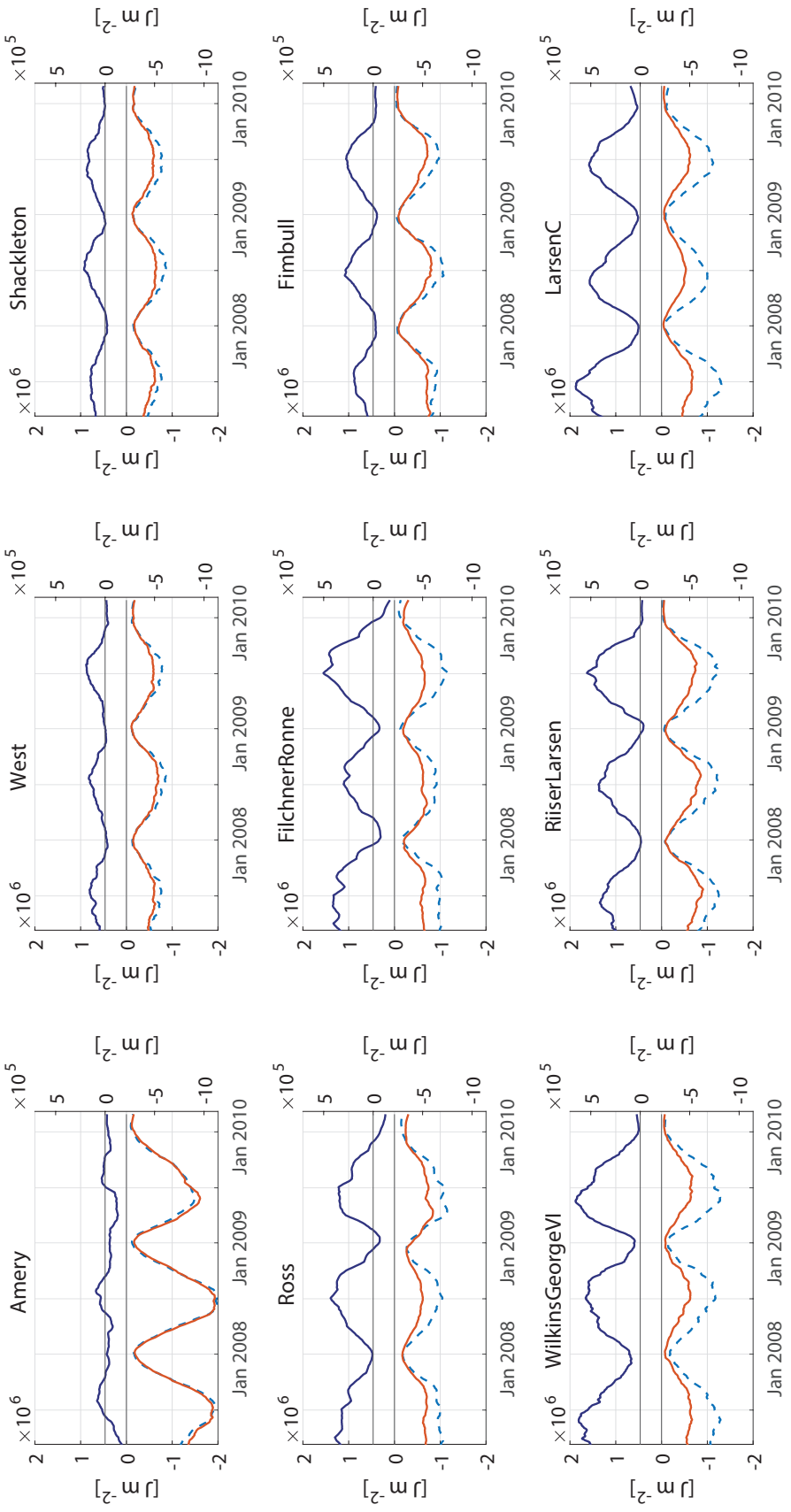

Figure A.5: Spatial averaged timeseries of cold content (CC, Jm^{-2}) in top 0.1 meter snow at all ice shelves, shown for all-sky (AS, orange, solid) and clear-sky (CS, blue, dashed) scenario (left axis) and the cloud effect on the CC (AS-CS, purple, right axis), visualized with a 15-day moving average.

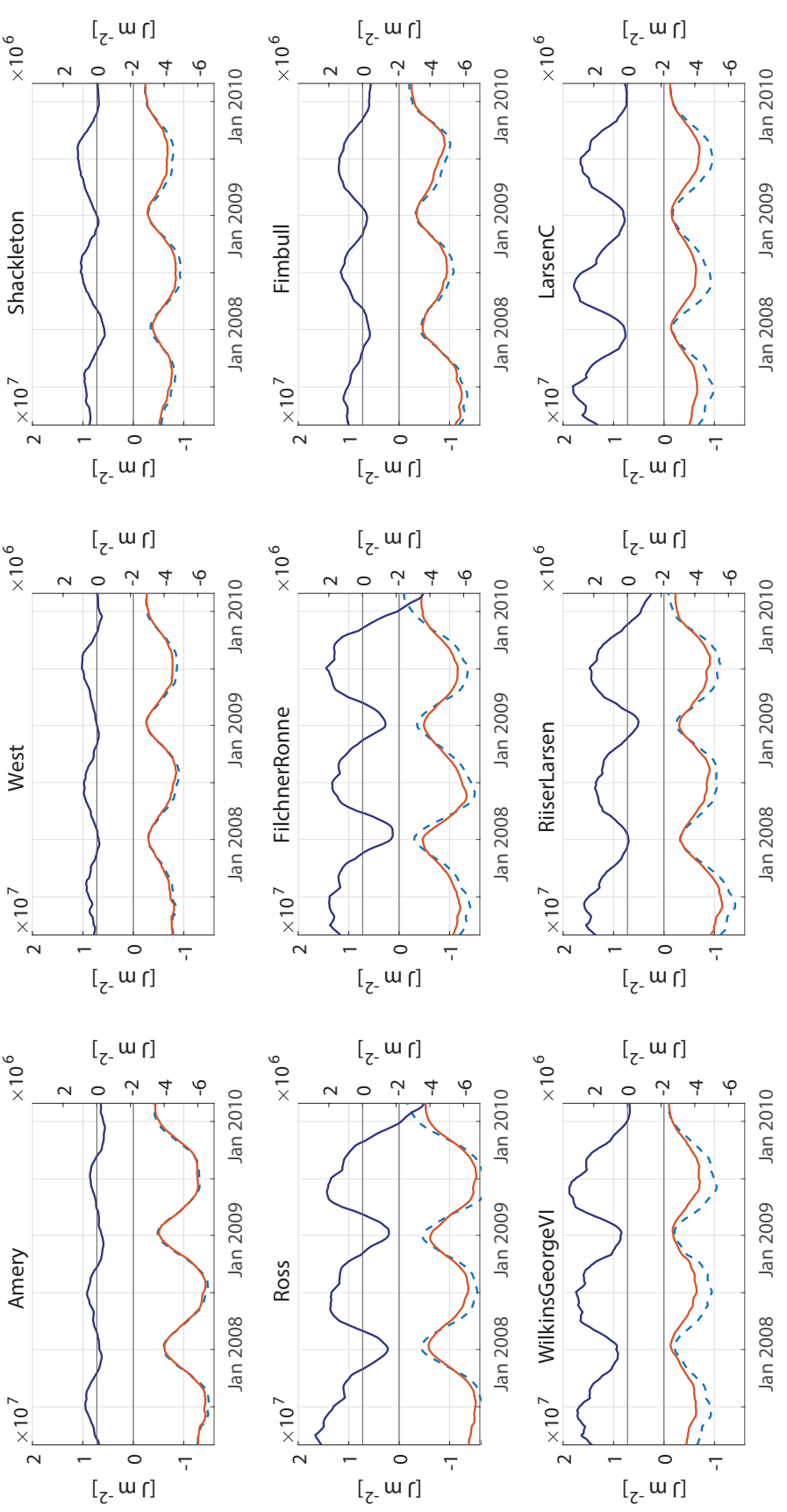

Figure A.6: Spatial averaged timeseries of cold content (CC, Jm^{-2}) in top 1 meter snow at all ice shelves, shown for all-sky (AS, orange, solid) and clear-sky (CS, blue, dashed) scenario (left axis) and the cloud effect on the CC (AS-CS, purple, right axis), visualized with a 15-day moving average.

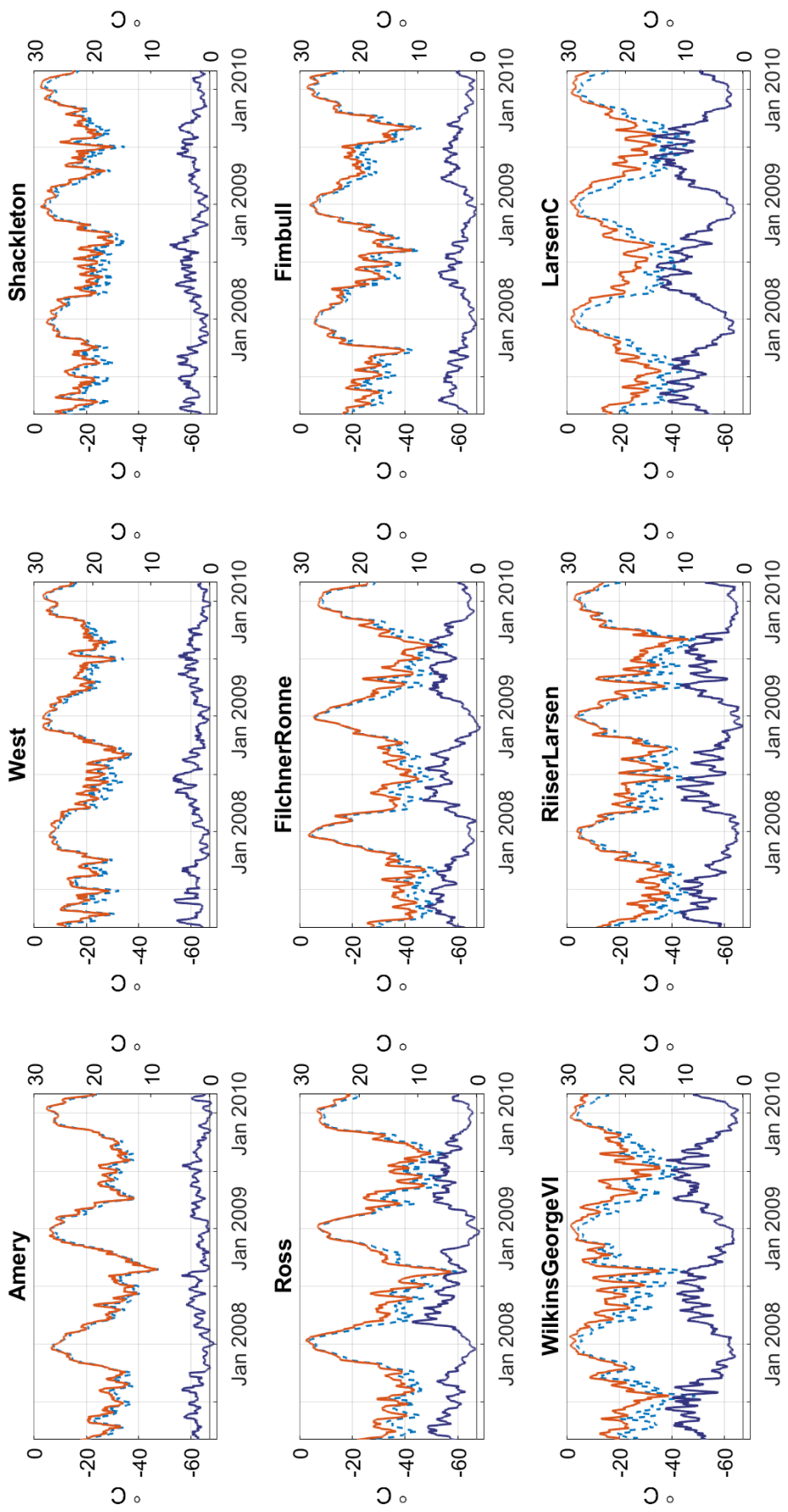

Figure A.7: Spatial averaged timeseries of surface temperature ($^{\circ}C$) at all ice shelves, shown for all-sky (AS, orange, solid) and clear-sky (CS, blue, dashed) scenario (left axis) and the cloud effect on the surface temperature (AS-CS, purple, right axis), visualized with a 15-day moving average.

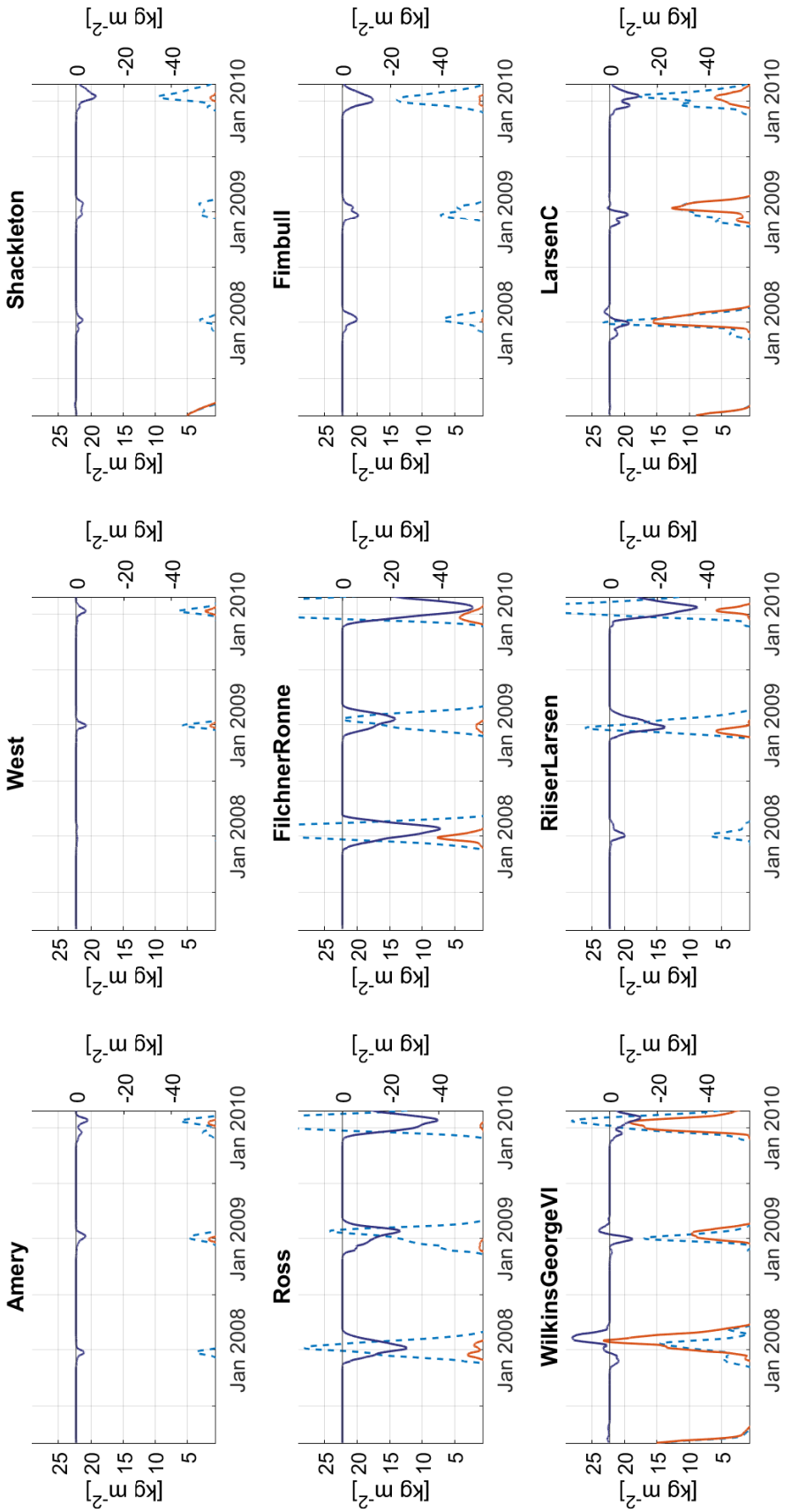

Figure A.8: Spatial averaged cumulative timeseries of liquid water mass (liqW, kgm^{-2}) at all ice shelves, shown for all-sky (AS, orange, solid) and clear-sky (CS, blue, dashed) scenario (left axis) and the cloud effect on the liqW mass (AS-CS, purple, right axis), visualized with a 15-day moving average.

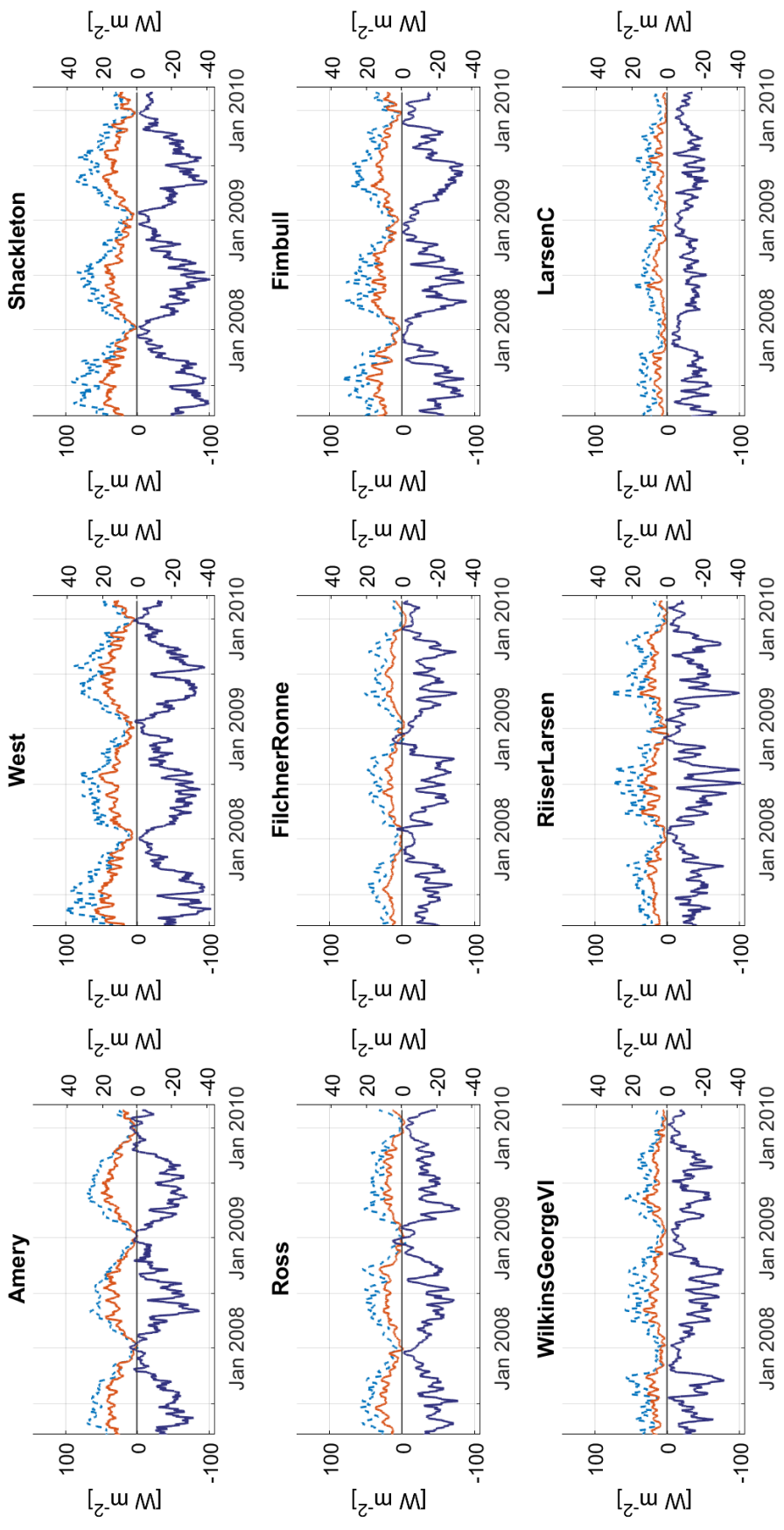

Figure A.9: Spatial averaged timeseries of sensible heat flux (SH, Wm^{-2}) at all ice shelves, shown for all-sky (AS, orange, solid) and clear-sky (CS, blue, dashed) scenario (left axis) and the cloud effect on the SH flux (AS-CS, purple, right axis), visualized with a 15-day moving average.

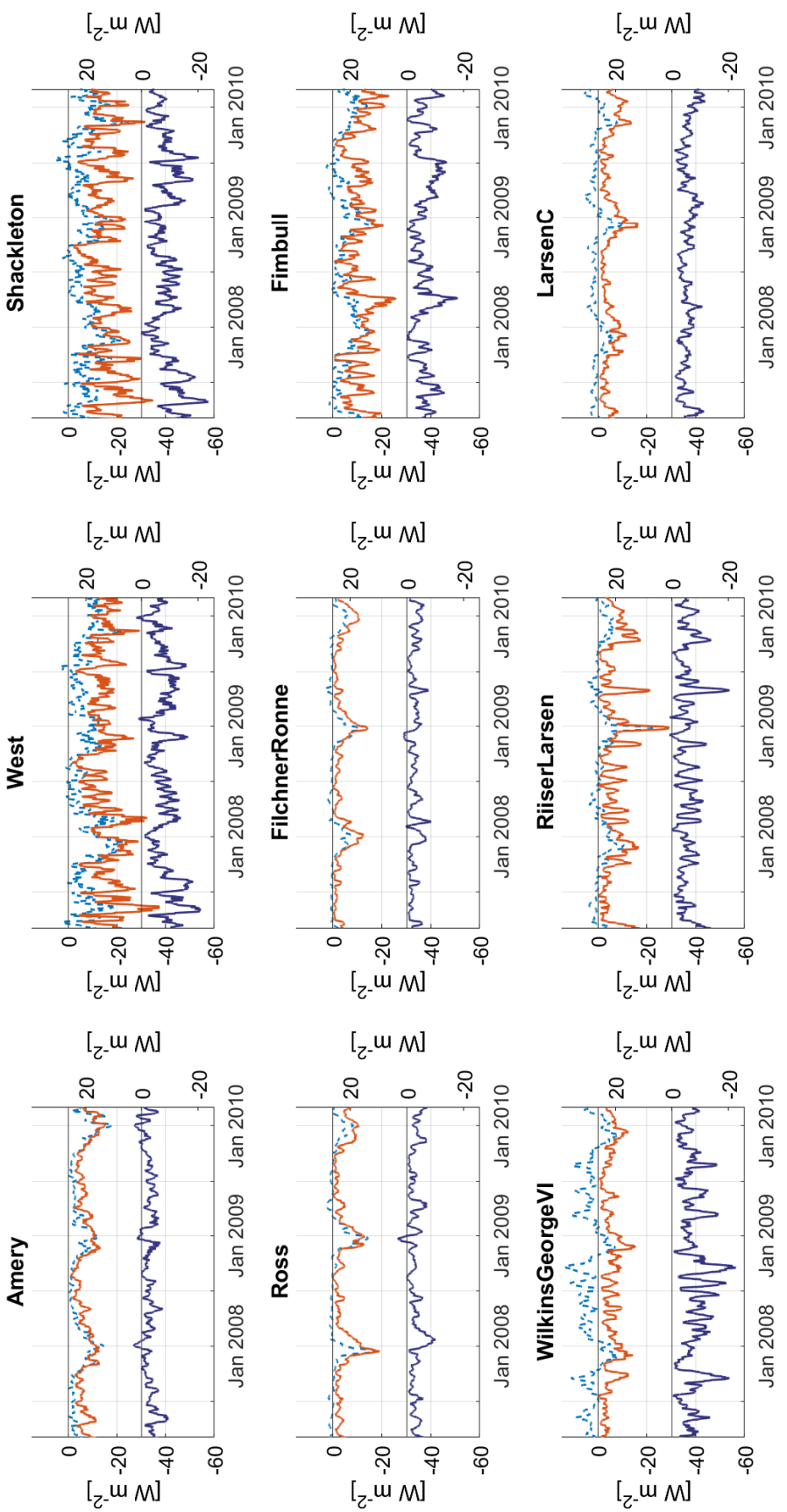

Figure A.10: Spatial averaged timeseries of latent heat flux (LH, Wm^{-2}) at all ice shelves, shown for all-sky (AS, orange, solid) and clear-sky (CS, blue, dashed) scenario (left axis) and the cloud effect on the LH flux (AS-CS, purple, right axis), visualized with a 15-day moving average.

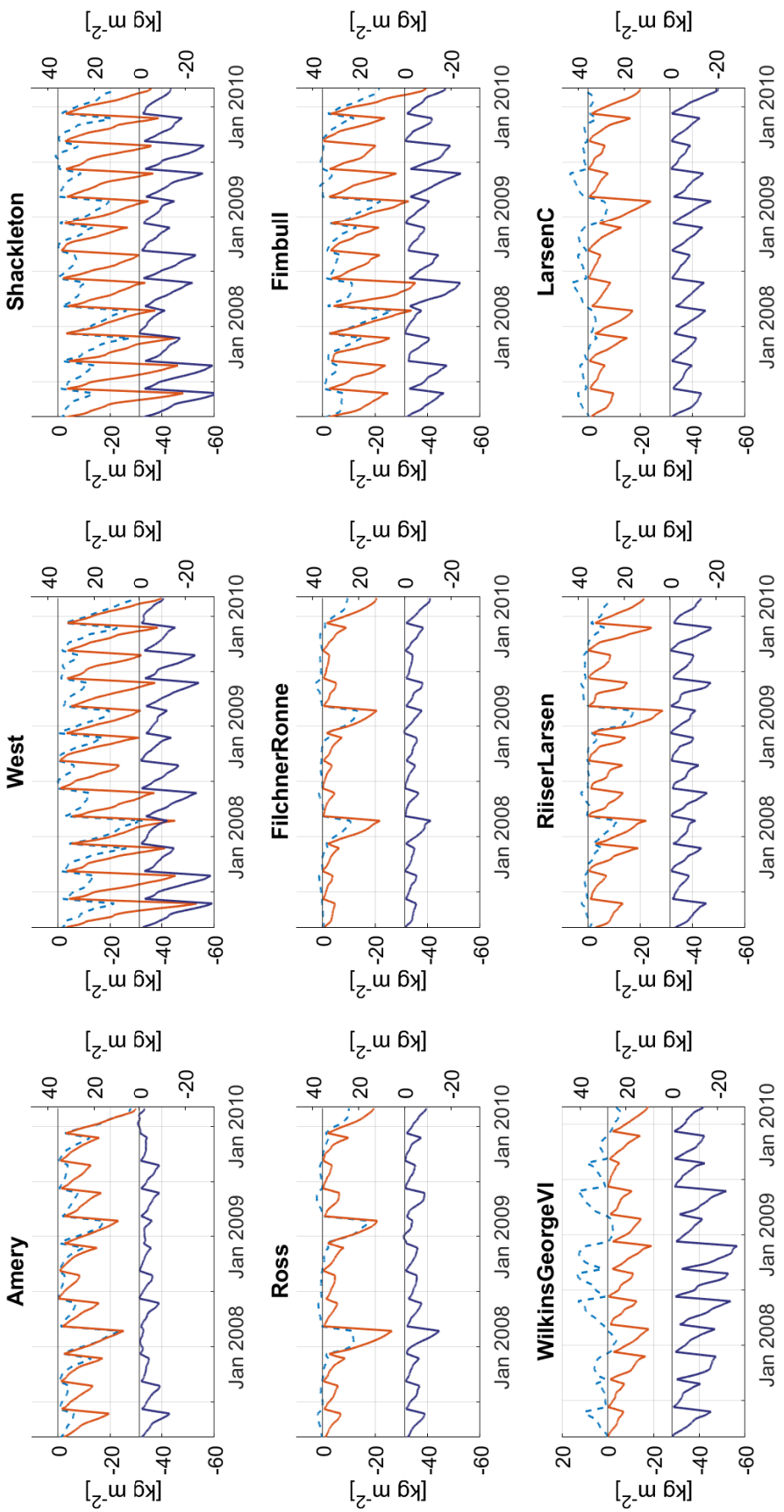

Figure A.11: Spatial averaged cumulative timeseries of sublimation mass (kgm^{-2}) at all ice shelves, shown for all-sky (AS, orange, solid) and clear-sky (CS, blue, dashed) scenario (left axis) and the cloud effect on the sublimation mass (AS-CS, purple, right axis), visualized with a 15-day moving average.

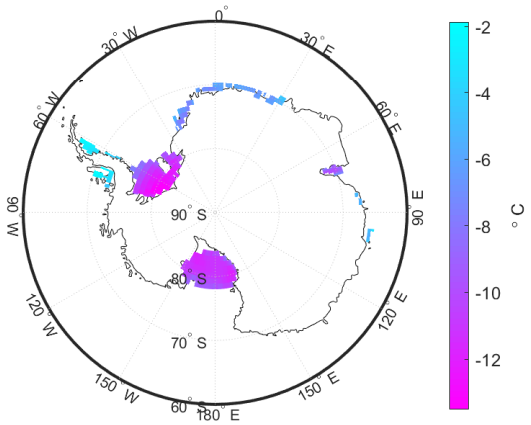

(a) T2m, atmospheric temperature ($^{\circ}C$) in DJF

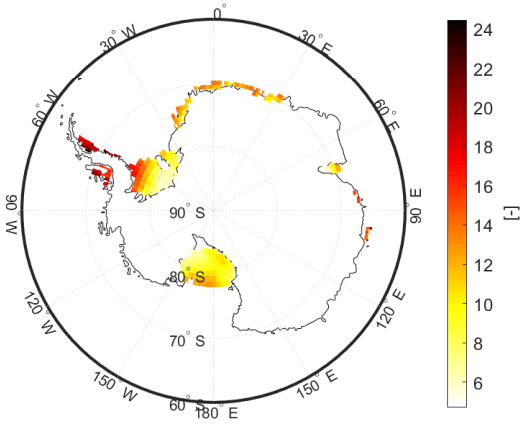

(b) τ, cloud optical depth (m/m) in DJF

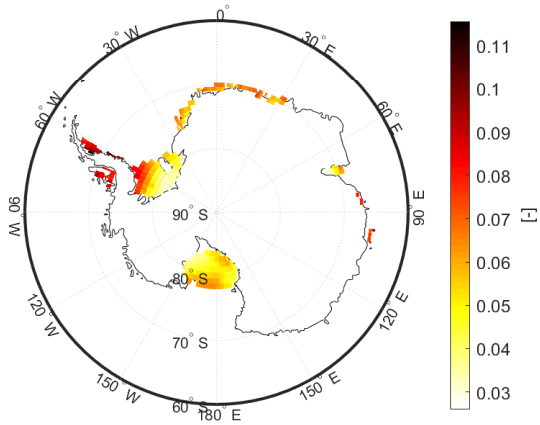

(c) IWP, cloud ice water path (kgm^{-2}) in DJF

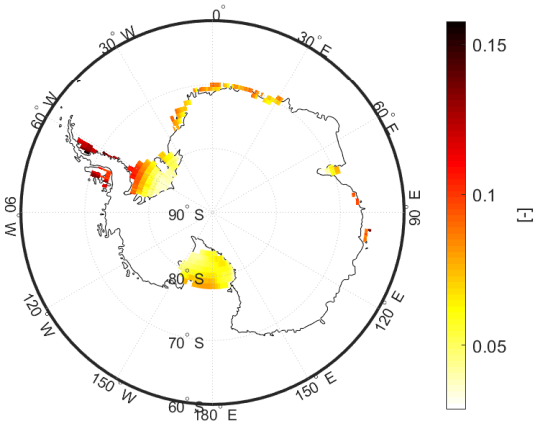

(d) LWP, cloud liquid water path (kgm^{-2}) in DJF

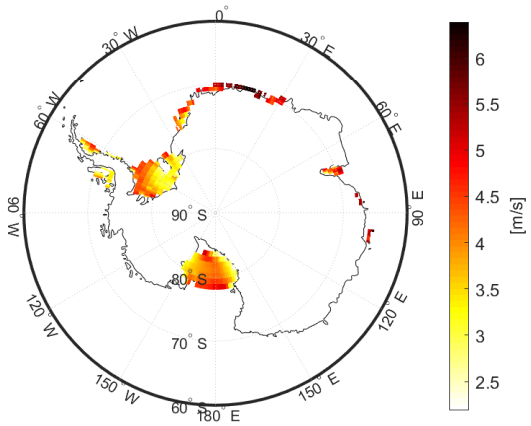

(e) ff10m, wind speed (m/s) in DJF

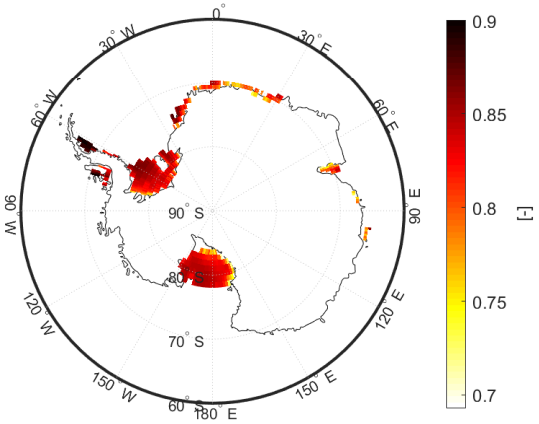

(f) rh2m, Relative Humidity (-) in DJF

Figure A.12: Spatial patterns of RACMO atmospheric variables that provide input for the SNOWPACK model. Average values in summer (DJF) for the three simulation years 2007-2010.

B

Tables

This appendix includes tables for quantified parameters at all ice shelves for all seasons. In Chapter 4 values are included for all ice shelves but only in summer (DJF). Tables included are: seasonal average net radiation (B.1), seasonal average albedo (B.2), seasonal average cold content (B.3), seasonal average liquid water mass (B.5) and seasonal average sublimation mass (B.6).

R_{net} (Wm^{-2})	Amery	Filchner-Ronne	Fimbull	Larsen C	Riiser-Larsen	Ross	Shackleton	West	Wilkins & George VI
All-sky	2.8	8.6	1.8	5.4	4.0	7.0	1.5	0.4	2.1
Clear-sky	-0.8	3.2	-8.5	-10.0	-5.8	0.8	-11.2	-11.5	-10.8
CRE	3.6	5.5	10.3	15.4	9.8	6.2	12.7	11.9	12.9

(a) DJF. Uncertainties in R_{net} are approximately $\pm 7.7 Wm^{-2}$

R_{net} (Wm^{-2})	Amery	Filchner-Ronne	Fimbull	Larsen C	Riiser-Larsen	Ross	Shackleton	West	Wilkins & George VI
All-sky	-27.9	-13.7	-18.5	-7.2	-13.9	-17.3	-19.6	-21.4	-15.5
Clear-sky	-51.6	-31.7	-49.8	-29.2	-39.0	-39.9	-57.5	-58.5	-41.9
CRE	23.7	18.0	31.4	21.9	25.1	22.6	37.8	37.1	26.4

(b) MAM. Uncertainties in R_{net} are approximately $\pm 4.7 Wm^{-2}$

R_{net} (Wm^{-2})	Amery	Filchner-Ronne	Fimbull	Larsen C	Riiser-Larsen	Ross	Shackleton	West	Wilkins & George VI
All-sky	-34.8	-17.2	-24.7	-12.1	-19.5	-21.4	-23.8	-29.3	-15.4
Clear-sky	-56.5	-36.3	-56.2	-31.5	-42.9	-41.2	-63.8	-64.9	-37.9
CRE	21.8	19.0	31.5	19.5	23.4	19.9	40.0	35.6	22.6

(c) JJA. Uncertainties in R_{net} are approximately $\pm 4.3 Wm^{-2}$

R_{net} (Wm^{-2})	Amery	Filchner-Ronne	Fimbull	Larsen C	Riiser-Larsen	Ross	Shackleton	West	Wilkins & George VI
All-sky	-16.8	-6.5	-11.0	-2.6	-8.2	-10.2	-10.4	-13.4	-7.8
Clear-sky	-25.2	-20.6	-25.7	-20.2	-27.8	-25.0	-32.4	-33.8	-29.3
CRE	8.4	14.1	14.7	17.6	19.6	14.8	21.9	20.3	21.5

(d) SON. Uncertainties in R_{net} are approximately $\pm 6.2 Wm^{-2}$

Table B.1: Average net Radiation (R_{net}, Wm^{-2}) values for (a) summer (DJF), (b) fall (MAM), (c) winter (JJA) and (d) spring (SON) at each ice shelf. Values are averaged over the three simulation years 2007-2010 and spatially averaged.

	Amery	Filchner-Ronne	Fimbull	Larsen C	Riiser-Larsen	Ross	Shackleton	West	Wilkins & George VI
All-sky	0.836	0.837	0.853	0.875	0.853	0.841	0.866	0.860	0.862
Clear-sky	0.804	0.788	0.808	0.815	0.805	0.788	0.814	0.816	0.810
CRE	0.032	0.048	0.045	0.060	0.049	0.053	0.052	0.043	0.052

(a) DJF. Uncertainties are approximately ±0.003(−)

	Amery	Filchner-Ronne	Fimbull	Larsen C	Riiser-Larsen	Ross	Shackleton	West	Wilkins & George VI
All-sky	0.877	0.879	0.885	0.893	0.889	0.886	0.891	0.891	0.893
Clear-sky	0.856	0.859	0.860	0.868	0.865	0.862	0.862	0.862	0.865
CRE	0.021	0.020	0.025	0.025	0.024	0.024	0.029	0.028	0.028

(b) MAM. Uncertainties are approximately ±0.0002(−)

	Amery	Filchner-Ronne	Fimbull	Larsen C	Riiser-Larsen	Ross	Shackleton	West	Wilkins & George VI
All-sky	0.885	0.896	0.893	0.897	0.895	0.893	0.895	0.893	0.897
Clear-sky	0.867	0.879	0.872	0.880	0.874	0.873	0.871	0.871	0.878
CRE	0.018	0.016	0.021	0.017	0.021	0.020	0.025	0.022	0.019

(c) JJA. Uncertainties are approximately ±0.000(−)

	Amery	Filchner-Ronne	Fimbull	Larsen C	Riiser-Larsen	Ross	Shackleton	West	Wilkins & George VI
All-sky	0.868	0.873	0.877	0.889	0.883	0.873	0.886	0.884	0.884
Clear-sky	0.843	0.851	0.845	0.848	0.850	0.846	0.849	0.849	0.843
CRE	0.025	0.022	0.032	0.042	0.033	0.027	0.038	0.035	0.042

(d) SON. Uncertainties are approximately ±0.0004(−)

Table B.2: Average albedo (-) values for (a) summer (DJF), (b) fall (MAM), (c) winter (JJA) and (d) spring (SON) at each ice shelf. Values are averaged over the three simulation years 2007-2010 and spatially averaged.

	Amery	Filchner-Ronne	Fimbull	Larsen C	Riiser-Larsen	Ross	Shackleton	West	Wilkins & George VI
	$\times 10^5$	$\times 10^5$	$\times 10^5$	$\times 10^5$	$\times 10^5$	$\times 10^5$	$\times 10^5$	$\times 10^5$	$\times 10^5$
All-sky	-1.95	-2.13	-0.84	-0.41	-0.64	-2.77	-1.36	-1.22	-0.65
Clear-sky	-1.32	-1.14	-0.60	-0.86	-0.47	-2.07	-1.38	-1.12	-1.34
CRE	-0.63	-0.99	-0.24	0.45	-0.18	-0.70	0.02	-0.10	0.69

(a) DJF

	Amery	Filchner-Ronne	Fimbull	Larsen C	Riiser-Larsen	Ross	Shackleton	West	Wilkins & George VI
	$\times 10^5$	$\times 10^5$	$\times 10^5$	$\times 10^5$	$\times 10^5$	$\times 10^5$	$\times 10^5$	$\times 10^5$	$\times 10^5$
All-sky	-6.51	-6.33	-6.21	-4.27	-5.84	-6.75	-5.08	-5.25	-4.38
Clear-sky	-9.56	-9.42	-7.70	-9.00	-9.25	-10.4	-6.18	-5.78	-9.94
CRE	3.06	3.09	1.48	4.72	3.41	3.66	1.11	0.53	5.57

(b) MAM

	Amery	Filchner-Ronne	Fimbull	Larsen C	Riiser-Larsen	Ross	Shackleton	West	Wilkins & George VI
	$\times 10^5$	$\times 10^5$	$\times 10^5$	$\times 10^5$	$\times 10^5$	$\times 10^5$	$\times 10^5$	$\times 10^5$	$\times 10^5$
All-sky	-7.00	-6.23	-7.45	-6.18	-8.36	-6.77	-6.41	-6.51	-6.89
Clear-sky	-10.4	-9.88	-9.98	-11.1	-12.6	-9.97	-8.29	-8.36	-12.1
CRE	3.39	3.65	2.53	4.97	4.24	3.20	1.89	1.85	5.22

(c) JJA

	Amery	Filchner-Ronne	Fimbull	Larsen C	Riiser-Larsen	Ross	Shackleton	West	Wilkins & George VI
	$\times 10^5$	$\times 10^5$	$\times 10^5$	$\times 10^5$	$\times 10^5$	$\times 10^5$	$\times 10^5$	$\times 10^5$	$\times 10^5$
All-sky	-4.50	-4.71	-4.175	-3.07	-4.31	-4.26	-3.92	-4.06	-3.52
Clear-sky	-5.79	-6.55	-4.28	-4.39	-5.24	-5.39	-4.44	-4.33	-5.73
CRE	1.30	1.84	0.11	1.32	0.93	1.13	0.52	0.28	2.21

(d) SON

Table B.3: Average cold content (CC, Jm^{-2}) of top 0.1 meter snow for (a) summer (DJF), (b) fall (MAM), (c) winter (JJA) and (d) spring (SON) at each ice shelf. Values are averaged over the three simulation years 2007-2010 and spatially averaged.

	Amery	Filchner-Ronne	Fimbull	Larsen C	Riiser-Larsen	Ross	Shackleton	West	Wilkins & George VI
All-sky	-10.6	-11.6	-7.8	-4.0	-8.1	-11.2	-6.7	-7.3	-4.5
Clear-sky	-11.5	-13.1	-8.9	-7.6	-9.9	-12.7	-8.2	-8.6	-7.7
CRE	0.9	1.5	1.2	3.6	1.8	1.5	1.5	1.2	3.2

(a) DJF

	Amery	Filchner-Ronne	Fimbull	Larsen C	Riiser-Larsen	Ross	Shackleton	West	Wilkins & George VI
All-sky	-27.1	-34.6	-21.1	-20.0	-23.8	-32.5	-17.2	-17.6	-16.5
Clear-sky	-29.4	-40.7	-25.2	-30.5	-31.2	-38.7	-20.3	-20.6	-24.8
CRE	2.3	6.1	4.0	10.6	7.4	6.2	3.1	3.1	8.3

(b) MAM

	Amery	Filchner-Ronne	Fimbull	Larsen C	Riiser-Larsen	Ross	Shackleton	West	Wilkins & George VI
All-sky	-32.2	-39.3	-27.5	-27.7	-31.2	-39.9	-20.2	-22.2	-23.7
Clear-sky	-34.6	-45.4	-31.5	-38.4	-38.1	-44.7	-24.2	-25.5	-33.1
CRE	2.4	6.1	4.0	10.7	6.8	4.8	4.1	3.3	9.4

(c) JJA

	Amery	Filchner-Ronne	Fimbull	Larsen C	Riiser-Larsen	Ross	Shackleton	West	Wilkins & George VI
All-sky	-25.2	-28.9	-22.3	-16.4	-21.7	-28.6	-16.5	-17.7	-13.8
Clear-sky	-26.5	-32.0	-24.4	-22.1	-25.1	-32.0	-18.8	-19.4	-18.1
CRE	1.2	3.1	2.1	5.7	3.4	3.4	2.2	1.8	4.3

(d) SON

Table B.4: Average snow surface temperature (T_{sfc} in $^{\circ}C$) for (a) summer (DJF), (b) fall (MAM), (c) winter (JJA) and (d) spring (SON) at each ice shelf. Values are averaged over the three simulation years 2007-2010 and spatially averaged.

	Amery	Filchner-Ronne	Fimbull	Larsen C	Riiser-Larsen	Ross	Shackleton	West	Wilkins & George VI
All-sky	0.3	1.6	0.4	5.4	1.1	0.7	0.3	0.3	9.0
Clear-sky	1.5	25.7	4.4	8.6	12.3	17.8	2.4	1.1	9.6
CRE	-1.2	-24.1	-4.1	-3.2	-11.2	-17.0	-2.1	-0.8	-0.6

(a) DJF. Uncertainties are approximately $\pm 6.13 (kgm^{-2})$

	Amery	Filchner-Ronne	Fimbull	Larsen C	Riiser-Larsen	Ross	Shackleton	West	Wilkins & George VI
All-sky	0.0	0.0	0.0	0.5	0.0	0.0	0.5	0.0	1.2
Clear-sky	0.0	0.0	0.0	0.5	0.0	0.0	0.4	0.0	1.0
CRE	0.0	0.0	0.0	0.0	0.0	0.0	0.0	0.0	0.2

(b) MAM. Uncertainties are approximately $\pm 0.02 (kgm^{-2})$

	Amery	Filchner-Ronne	Fimbull	Larsen C	Riiser-Larsen	Ross	Shackleton	West	Wilkins & George VI
All-sky	0.0	0.0	0.0	0.0	0.0	0.0	0.0	0.0	0.0
Clear-sky	0.0	0.0	0.0	0.0	0.0	0.0	0.0	0.0	0.0
CRE	0.0	0.0	0.0	0.0	0.0	0.0	0.0	0.0	0.0

(c) JJA. Uncertainties are approximately $\pm 0 (kgm^{-2})$

	Amery	Filchner-Ronne	Fimbull	Larsen C	Riiser-Larsen	Ross	Shackleton	West	Wilkins & George VI
All-sky	0.0	0.1	0.0	0.1	0.1	0.1	0.0	0.0	0.1
Clear-sky	0.1	0.2	0.1	0.6	0.3	0.5	0.0	0.0	0.5
CRE	-0.1	-0.2	-0.1	-0.6	-0.2	-0.5	0.0	0.0	-0.4

(d) SON. Uncertainties are approximately $\pm 0.12 (kgm^{-2})$

Table B.5: Average liquid water mass (liqW, kgm^{-2}) values for (a) summer (DJF), (b) fall (MAM), (c) winter (JJA) and (d) spring (SON) at each ice shelf. Values are averaged over the three simulation years 2007-2010 and spatially averaged.

	Amery	Filchner-Ronne	Fimbull	Larsen C	Riiser-Larsen	Ross	Shackleton	West	Wilkins & George VI
All-sky	-14.5	-12.4	-18.9	-12.0	-14.3	-13.4	-19.0	-20.8	-10.1
Clear-sky	-13.1	-7.2	-13.6	-3.0	-7.8	-9.1	-12.7	-15.3	-2.3
CRE	-1.4	-5.1	-5.3	-9.0	-6.5	-4.3	-6.3	-5.6	-7.8

(a) DJF. Uncertainties are approximately $\pm 4.1 (kgm^{-2})$

	Amery	Filchner-Ronne	Fimbull	Larsen C	Riiser-Larsen	Ross	Shackleton	West	Wilkins & George VI
All-sky	-9.4	-2.8	-17.8	-5.3	-7.6	-3.7	-20.0	-22.4	-5.2
Clear-sky	-4.4	0.5	-5.3	3.3	0.9	1.1	-5.3	-8.1	7.0
CRE	-5.0	-3.3	-12.5	-8.6	-8.5	-4.7	-14.6	-14.3	-12.2

(b) MAM. Uncertainties are approximately $\pm 2.1 (kgm^{-2})$

	Amery	Filchner-Ronne	Fimbull	Larsen C	Riiser-Larsen	Ross	Shackleton	West	Wilkins & George VI
All-sky	-6.4	-1.8	-13.2	-3.2	-4.9	-3.0	-20.0	-17.8	-4.0
Clear-sky	-2.1	0.6	-2.4	1.8	0.7	0.4	-4.6	-5.0	4.5
CRE	-4.2	-2.4	-10.8	-4.9	-5.6	-3.4	-15.4	-12.8	-8.5

(c) JJA. Uncertainties are approximately $\pm 1.1 (kgm^{-2})$

	Amery	Filchner-Ronne	Fimbull	Larsen C	Riiser-Larsen	Ross	Shackleton	West	Wilkins & George VI
All-sky	-7.1	-3.5	-11.3	-6.4	-8.1	-3.9	-18.1	-17.2	-8.9
Clear-sky	-4.6	-0.1	-5.8	0.6	-1.6	-0.9	-8.5	-9.1	5.0
CRE	-2.5	-3.4	-5.5	-7.0	-6.6	-3.0	-9.6	-8.1	-13.9

(d) SON. Uncertainties are approximately $\pm 2.2 (kgm^{-2})$

Table B.6: Average sublimated mass (kgm^{-2}) values for (a) summer (DJF), (b) fall (MAM), (c) winter (JJA) and (d) spring (SON) at each ice shelf. Values are averaged over the three simulation years 2007-2010 and spatially averaged.

Bibliography

R. A. Anthes, E.-Y. Hsie, and Y.-H. Kuo. Description of the Penn State/NCAR Mesoscale Model Version 4 (MM4). Technical Report NCAR/TN-282+STR, National Center for Atmospheric Research, Boulder, Colorado, May 1987.

K. J. Arrow, L. Hurwicz, and H. Uzawa. Constraint qualifications in maximization problems. *Naval Research Logistics Quarterly*, 8:175–191, 1961.

R. Bindschadler, H. Choi, A. Wichlacz, R. Bingham, J. Bohlander, K. Brunt, H. Corr, R. Drews, H. Fricker, M. Hall, R. Hindmarsh, J. Kohler, L. Padman, W. Rack, G. Rotschky, S. Urbini, P. Vornberger, and N. Young. Getting around Antarctica: new high-resolution mappings of the grounded and freely-floating boundaries of the Antarctic ice sheet created for the International Polar Year. *The Cryosphere*, 5(3):569–588, 2011. doi: 10.5194/tc-5-569-2011.

R. Bintanja and M. R. Van den Broeke. The influence of clouds on the radiation budget of ice and snow surfaces in Antartica and Greenland in summer. *International Journal of Climatology*, 16:1281–1296, 1996.

S. Bony, R. Colman, V. M. Kattsov, R. P. Allan, C. S. Bretherton, J.-L. Dufresne, A. Hall, S. Hallegatte, M. M. Holland, W. Ingram, D. A. Randall, D. J. Soden, G. Tselioudis, and M. J. Webb. How well do we understand and evaluate climate change feedback processes? *J. Climate*, 19:3445–3482, 2006. doi: 10.1175/JCLI3819.1.

O. Boucher, D. Randall, P. Artaxo, C. Bretherton, G. Feingold, P. Forster, V.-M. Kerminen, Y. Kondo, H. Liao, U. Lohmann, P. Rasch, S.K. Satheesh, S. Sherwood, B. Stevens, and X.Y. Zhang. Clouds and aerosols. In [T.F. Stocker, D. Qin, G.-K. Plattner, M. Tignor, S.K. Allen, J. Boschung, A. Nauels, Y. Xia, V. Bex, and P.M. Midgley], editors, *Climate Change 2013: The Physical Science Basis. Contribution of Working Group I to the Fifth Assessment Report of the Intergovernmental Panel on Climate Change*. Cambridge University Press, 2013.

W. L. Chapman and J. E. Walsh. A synthesis of Antarctic temperatures. *Journal of Climate*, 20(16):4096–4117, 2007. doi: 10.1175/JCLI4236.1.

A. H.-D. Cheng and D. T. Cheng. Heritage and early history of the boundary element method. *Engineering Analysis with Boundary Elements*, 29(3):268 – 302, 2005. ISSN 0955-7997. doi: https://doi.org/10.1016/j.enganabound.2004.12.001.

P. U. Clark, J. D. Shakun, S. A. Marcott, A. C. Mix, M. Eby, S. Kulp, A. Levermann, G. A. Milne, P. L. Pfister, B. D. Santer, D. P. Schrag, S. Solomon, T. F. Stocker, B. H. Strauss, A. J. Weaver, R. Winkelmann, D. Archer, E. Bard, A. Goldner, K Lambeck, R. T. Pierrehumbert, and G.-K. Plattner. Consequences of twenty-first-century policy for multi-millennial climate and sea-level change. *Nature Climate Change*, 6:360–369, February 2016. doi: https://doi.org/10.1038/nclimate2923.

CloudSat DPC. CloudSat data processing centre. URL `http://www.cloudsat.cira.colostate.edu/`.

A.J. Cook and D.G. Vaughan. Overview of areal changes of the ice shelves on the Antarctic Peninsula over the past 50 years. *The Cryosphere*, 4(1):77–98, 2010.

Cooperative Institute for Research in the Atmosphere. CloudSat Standard Data Products Handbook, April 2008.

Judith A. Curry, Julie L. Schramm, William B. Rossow, and David Randall. Overview of Arctic cloud and radiation characteristics. *Journal of Climate*, 9(8):1731–1764, 1996. doi: 10.1175/1520-0442(1996)009<1731:OOACAR>2.0.CO;2.

R. M. DeConto and D. Pollard. Contribution of Antarctica to past and future sea-level rise. *Nature*, 531:591, 2016. doi: 10.1038/nature17145.

E.G Dutton. Basic and other measurements of radiation at station South Pole (2007-01 to 2010-02). Climate Monitoring & Diagnostics Laboratory, Boulder, PANGAEA, 2008, 2009, 2010. doi: 10.1594/PANGAEA.706268.

J. Ettema, M. R. van den Broeke, E. van Meijgaard, W. J. van de Berg, J. E. Box, and K. Steffen. Climate of the greenland ice sheet using a high-resolution climate model—part 1: evaluation. *The Cryosphere*, 4:511–527, 2010.

M. G. Flanner and C. S. Zender. Linking snowpack microphysics and albedo evolution. *Journal of Geophysical Research*, 111(D12208), 2006. doi: doi:10.1029/2005JD006834.

P. Fretwell, H. D. Pritchard, D. G. Vaughan, J. L. Bamber, N. E. Barrand, R. Bell, C. Bianchi, R. G. Bingham, D. D. Blankenship, G. Casassa, G. Catania, D. Callens, H. Conway, A. J. Cook, H. F. J. Corr, D. Damaske, V. Damm, F. Ferraccioli, R. Forsberg, S. Fujita, Y. Gim, P. Gogineni, J. A. Griggs, R. C. A. Hindmarsh, P. Holmlund, J. W. Holt, R. W. Jacobel, A. Jenkins, W. Jokat, T. Jordan, E. C. King, J. Kohler, W. Krabill, M. Riger-Kusk, K. A. Langley, G. Leitchenkov, C. Leuschen, B. P. Luyendyk, K. Matsuoka, J. Mouginot, F. O. Nitsche, Y. Nogi, O. A. Nost, S. V. Popov, E. Rignot, D. M. Rippin, A. Rivera, J. Roberts, N. Ross, M. J. Siegert, A. M. Smith, D. Steinhage, M. Studinger, B. Sun, B. K. Tinto, B. C. Welch, D. Wilson, D. A. Young, C. Xiangbin, and A. Zirizzotti. Bedmap2: improved ice bed, surface and thickness datasets for Antarctica. *The Cryosphere*, 7 (1):375–393, 2013. doi: 10.5194/tc-7-375-2013.

H. A. Fricker and L. Padman. Thirty years of elevation change on Antarctic Peninsula ice shelves from multimission satellite radar altimetry. *Journal of Geophysical Research-Oceans*, 117, Feb 2012. doi: 10.1029/2011jc007126. n/a.

A. S. Gardner and M. J. Sharp. A review of snow and ice albedo and the development of a new physically based broadband albedo parameterization. *Journal of Geophysical Research*, 115:1–15, 2010.

A. S. Gardner, G. Moholdt, T. A. Scambos, M. Fahnstock, S. Ligtenberg, M. R. Van den Broeke, and J. Nilsson. Increased West Antarctic and unchanged East Antarctic ice discharge over the last 7 years. *The Cryosphere*, 12(2):521–547, 2018. doi: 10.5194/tc-12-521-2018.

H. P. Gavin. The Levenberg-Marquardt algorithm for nonlinear least squares curve-fitting problems. Technical report, Department of Civil and Environmental Engineering, Duke University, January 2019.

C. Genthon and G. Krinner. Antarctic surface mass balance and systematic biases in general circulation models. *Journal of Geophysical Research: Atmospheres*, 106(D18):20653–20664, 2001. doi: 10.1029/2001JD900136.

E. Gilbert. Stop being such a melt: the effect of cloud microphysics on the surface energy balance of Larsen C, November 2018. URL `https://climategreat.wordpress.com/`.

N. F. Glasser and T. A. Scambos. A structural glaciological analysis of the 2002 Larsen B ice-shelf collapse. *Journal of Glaciology*, 54(184):3–16, 2008. doi: 10.3189/002214308784409017.

C. A. Greene, D. E. Gwyther, and D. D. Blankenship. Antarctic Mapping Tools for Matlab. *Computers Geosciences*, 104:151–157, 2017. doi: 10.1016/j.cageo.2016.08.003.

C. D. Groot Zwaaftink, A. Cagnati, A. Crepaz, C. Fierz, G. Macelloni, M. Valt, and M. Lehning. Event-driven deposition of snow on the Antarctic Plateau: analyzing field measurements with SNOWPACK. *The Cryosphere*, 7(1):333–347, 2013. doi: 10.5194/tc-7-333-2013.

M. T. Hagan and M. B. Menhaj. Training feedforward networks with the Marquardt algorithm. *IEEE Transactions on Neural Networks*, 5(6):989–993, Nov 1994. ISSN 1045-9227. doi: 10.1109/72.329697.

J. Heaton. *Introduction to Neural Networks with Java*. Heaton Research, Inc, second edition, 2008.

D. Henderson, T. S. L'Ecuyer, D. Vane, G. L. Stephens, and D. Reinke. Level 2B Fluxes and Heating Rates and 2B Fluxes and Heating Rates w/ Lidar Process Description and Interface Control Document, November 2011.

D.S. Henderson, T. S. L'Ecuyer, G. Stephens, P. Partain, and M. Sekiguchi. A multisensor perspective on the radiative impacts of clouds and aerosols. *Journal of Applied Meteorology and Climatology*, 52(4):853–871, 2013. doi: 10.1175/JAMC-D-12-025.1.

O. Hoegh-Guldbergand, D. Jacob, M. Taylor, M. Bindi, S. Brown, I. Camilloni, A. Diedhiou, R. Djalante, K. Ebi, F. Engelbrecht, J. Guiot, Y. Hijioka, S. Mehrotra, A. Payne, S. I. Seneviratne, A. Thomas, R. Warren, and G. Zhou. Impacts of 1.5°C global warming on natural and human systems. In [V. Masson-Delmotte, P. Zhai, H.O. Portner, D. Roberts, J. Skea, P.R. Shukla, A. Pirani, W. Moufouma-Okia, C. Pean, R. Pidcock, S. Connors, J. B. R. Matthews, Y. Chen, X. Zhou, M. I. Gomis, E. Lonnoy, T. Maycock, M. Tignor, and T. Waterfield], editors, *Global warming of 1.5° C. An IPCC Special Report on the impacts of global warming of 1.5° C above pre-industrial levels and related global greenhouse gas emission pathways, in the context of strengthening the global response to the threat of climate change, sustainable development, and efforts to eradicate poverty.*, page 177. In Press, October 2018.

S. Hofer, A. J. Tedstone, X. Fettweis, and J.L. Bamber. Decreasing cloud cover drives the recent mass loss on the Greenland ice sheet. *Science advances*, 3(e1700584), 2017. doi: 10.1126/sciadv.1700584.

P. R. Holland, H. F. J. Corr, H. D. Pritchard, D. G. Vaughan, R. J. Arthern, A. Jenkins, and M. Tedesco. The air content of Larsen Ice Shelf. , 38:L10503, 2011. doi: 10.1029/2011GL047245.

IPCC. Climate change 2007: Summary for policymakers. In [M.L. Parry, O.F. Canziani, J.P. Palutikof, P.J. van der Linden, and C.E. Hanson], editors, *Impacts, Adaptation and Vulnerability. Contribution of Working Group II to the Fourth Assessment Report of the Intergovernmental Panel on Climate Change*, pages 7–22. Cambridge University Press, 2007.

IPCC. Climate change 2014: Synthesis report. In [R.K. Pachauri and L.A. Meyer], editors, *Contribution of Working Groups I, II and III to the Fifth Assessment Report of the Intergovernmental Panel on Climate Change*. 2014.

M Izeboud, S. Lhermitte, K. van Tricht, J. T. M. Lenaerts, N. van Lipzig, and N. Wever. Greenland ice sheet firn memory determines its response to cloud radiation. submitted.

J. C. King, A. Gadian, A. Kirchgaessner, P. Kuipers Munneke, T. A. Lachlan-Cope, A. Orr, C. Reijmer, M. R. Van den Broeke, J. M. Van Wessem, and M. Weeks. Validation of the summertime surface energy budget of Larsen C Ice Shelf (Antarctica) as represented in three high-resolution atmospheric models. *Journal of Geophysical Research: Atmospheres*, 120(4):1335–1347, 2015. doi: 10.1002/2014JD022604.

M. A. King, R. Coleman, A.-J. Freemantle, H. A. Fricker, R. S. Hurd, B. Legrésy, L. Padman, and R. Warner. A 4-decade record of elevation change of the Amery ice shelf, east antarctica. *Journal of Geophysical Research: Earth Surface*, 114(F1). doi: 10.1029/2008JF001094.

G. König-Langlo. Basic and other measurements of radiation at Neumayer Station (2007-01 to 2010-12). Alfred Wegener Institute, Helmholtz Centre for Polar and Marine Research, Bremerhaven, PANGAEA, 2008, 2009, 2010. doi: 10.1594/PANGAEA.692973.

P. Kuipers Munneke, M. R. Van den Broeke, J. T. M. Lenaerts, M. G. Flanner, A. S. Gardner, and W. J. Van de Berg. A new albedo parameterization for use in climate models over the Antarctic ice sheet. *Journal of Geophysical Research*, 116, 2011. doi: 10.1029/2010JD015113.

P. Kuipers Munneke, M. R. Van den Broeke, J. C. King, T. Gray, and C. H. Reijmer. Near-surface climate and surface energy budget of Larsen C ice shelf, Antarctic Peninsula. *The Cryosphere*, 6(2):353–363, 2012. doi: 10.5194/tc-6-353-2012.

T. S. L'Ecuyer, N. B. Wood, T Haladay, G. L. Stephens, and P. W. Stackhouse Jr. Impact of clouds on atmospheric heating based on the R04 CloudSat fluxes and heating rates data set. *Journal of Geophysical Research: Atmospheres*, 113(D8), 2008. doi: 10.1029/2008JD009951.

M. Lehning, P. Bartelt, B. Brown, and C. Fierz. A physical SNOWPACK model for the swiss avalanche warning: Part III: meteorological forcing, thin layer formation and evaluation. *Cold Regions Science and Technology*, 35(3):169 – 184, 2002a. ISSN 0165-232X. doi: https://doi.org/10.1016/S0165-232X(02)00072-1.

M. Lehning, P. Bartelt, B. Brown, C. Fierz, and P. Satyawali. A physical SNOWPACK model for the swiss avalanche warning: part II. Snow microstructure. *Cold Regions Sci. Technol*, 35:147–167, 2002b.

J. T. M. Lenaerts, M. R. van den Broeke, S. J. Déry, E. van Meijgaard, W. J. van de Berg, Stephen P. Palm, and J. Sanz Rodrigo. Modeling drifting snow in Antarctica with a regional climate model: 1. Methods and model evaluation. *Journal of Geophysical Research: Atmospheres*, 117(D5), 2012. doi: 10.1029/2011JD016145.

J. T. M. Lenaerts, K. Van Tricht, S. Lhermitte, and T. S. L'Ecuyer. Polar clouds and radiation in satellite observations, reanalyses, and climate models. *Geophysical Research Letters*, 44(7):3355–3364, 2017. doi: 10.1002/2016GL072242.

A. Levermann, P. U. Clark, B. Marzeion, G. A. Milne, D. Pollard, V. Radic, and A. Robinson. The multimillennial sea-level commitment of global warming. 110(34):13745–13750, 2013. ISSN 0027-8424. doi: 10.1073/pnas.1219414110.

A. Luckman, D. Jansen, B. Kulessa, E. C. King, P. Sammonds, and D. I. Benn. Basal crevasses in Larsen C ice shelf and implications for their global abundance. *The Cryosphere*, 6(1):113–123, 2012. doi: 10.5194/tc-6-113-2012.

D. Marks, J. Domingo, D. Susong, T. Link, and D. Garen. A spatially distributed energy balance snowmelt model for application in mountain basins. *Hydrological Processes*, 13(12-13):1935–1959, 1999. doi: 10.1002/(SICI)1099-1085(199909)13:12/13<1935::AID-HYP868>3.0.CO;2-C.

G. J. Marshall, A. Orr, N. P. M. van Lipzig, and J. C. King. The Impact of a Changing Southern Hemisphere Annular Mode on Antarctic Peninsula Summer Temperatures. *Journal of Climate*, 19(20):5388–5404, 2006. doi: 10.1175/JCLI3844.1.

A. V. Matus and T. S. L'Ecuyer. The role of cloud phase in Earth's radiation budget. *Journal of Geophysical Research: Atmospheres*, 122(5):2559–2578, 2017. doi: 10.1002/2016JD025951.

B. W. J. Miles, C. R. Stokes, A. Vieli, and N. J. Cox. Rapid, climate-driven changes in outlet glaciers on the Pacific coast of East Antarctica. *Nature*, 500:563, 2013. doi: 10.1038/nature12382.

NASA's Earth Sciences News Team. More glaciers in east antarctica are waking up, December 2018. URL `https://www.nasa.gov/feature/goddard/2018/more-glaciers-in-antarctica-are-waking-up`.

J. Oerlemans and W. H. Knap. A 1 year record of global radiation and albedo in the ablation zone of Morteratschgletscher, Switzerland. *Journal of Glaciology*, 44(147):231–238, 1998. doi: 10.3189/S0022143000002574.

T. Phillips, H. Rajaram, and K. Steffen. Cryo-hydrologic warming: A potential mechanism for rapid thermal response of ice sheets. *Geophysical Research Letters*, 37(20), 2010. doi: 10.1029/2010GL044397.

H. D. Pritchard, S. R. M. Ligtenberg, H. A. Fricker, D. G. Vaughan, M. R. Van den Broeke, and L. Padman. Antarctic ice-sheet loss driven by basal melting of ice shelves. *Nature*, 484:502, 2012. doi: 10.1038/nature10968.

H.D. Pritchard and D.G. Vaughan. Widespread acceleration of tidewater glaciers on the Antarctic Peninsula. *Journal of Geophysical Research*, 112(F03S29), 2007. doi: 10.1029/2006JF000597.

V. Ramanathan, R. D. Cess, E. F. Harrison, P. Minnis, B. R. Barkstrom, E. Ahmad, and D. Hartmann. Cloud-radiative forcing and climate: Results from the earth radiation budget experiment. *Science*, 243(4887):57–63, 1989. ISSN 0036-8075. doi: 10.1126/science.243.4887.57.

D. J. Rasmussen, K. Bittermann, M. K. Buchanan, S. Kulp, B. H. Strauss, R. E. Kopp, and M. Oppenheimer. Extreme sea level implications of 1.5 °C, 2.0 °C, and 2.5 °C temperature stabilization targets in the 21st and 22nd centuries. *Environmental Research Letters*, 13(3):034040, mar 2018. doi: 10.1088/1748-9326/aaac87.

T. A. Scambos, C. Hulbe, M. Fahnestock, and J. Bohlander. The link between climate warming and break-up of ice shelves in the Antarctic Peninsula. *Journal of Glaciology*, 46(154):516–530, 2000. doi: 10.3189/172756500781833043.

T. A. Scambos, J. A. Bohlander, C. A. Shuman, and P. Skvarca. Glacier acceleration and thinning after ice shelf collapse in the Larsen B embayment, Antarctica. *Geophysical Research Letters*, 31, 2004. doi: doi:10.1029/2004GL020670.

A. Shepherd, D. Wingham, D. Wallis, K. Giles, S. Laxon, and A. Venke Sundal. Recent loss of floating ice and the consequent sea level contribution. *Geophyscial Research Letters*, 37:L13503, 2010. doi: 10.1029/2010GL042496.

M. D. Shupe and J. M. Intrieri. Cloud radiative forcing of the Arctic surface: the influence of cloud properties, surface albedo, and solar zenith angle. *Journal of Climate*, 17:616–628, 2004.

G. L. Stephens. Radiation profiles in extended water clouds. II: Parameterization schemes. *Journal of the Atmospheric Sciences*, 35(11):2123–2132, 1978a. doi: 10.1175/1520-0469(1978)035<2123:RPIEWC>2.0.CO;2.

G. L. Stephens. Radiation profiles in extended water clouds. I: Theory. *Journal of the Atmospheric Sciences*, 35(11):2111–2122, 1978b. doi: 10.1175/1520-0469(1978)035<2111:RPIEWC>2.0.CO;2.

G. L. Stephens, D. G. Vane, R. J. Boain, G. G. Mace, K. Sassen, Z. Wang, A. J. Illingworth, E. J. O'connor, W. B. Rossow, S. L. Durden, S. D. Miller, R. T. Austin, A. Benedetti, and C. Mitrescu. The CloudSat mission and the A-train. *Bulletin of the American Meteorological Society*, 83(12):1771–1790, 2002. doi: 10.1175/BAMS-83-12-1771.

The IMBIE team. Mass balance of the Antarctic ice sheet from 1992 to 2017. *Nature*, 558(7709):219–222, 2018. ISSN 1476-4687. doi: 10.1038/s41586-018-0179-y.

L. D. Trusel, K. E. Frey, and S. B. Das. Antarctic surface melting dynamics: Enhanced perspectives from radar scatterometer data. *Journal of Geophysical Research: Earth Surface*, 117(F2), 2012. doi: 10.1029/2011JF002126.

D. D. Turner, A. M. Vogelmann, R. T. Austin, J. C. Barnard, K. Cady-Pereira, J. C. Chiu, S. A. Clough, C. Flynn, M. M. Khaiyer, J. Liljegren, K. Johnson, B. Lin, C. Long, A. Marshak, S. Y. Matrosov, S. A. McFarlane, M. Miller, Q. Min, P. Minimis, W. O'Hirok, Z. Wang, and W. Wiscombe. Thin liquid water clouds: Their importance and our challenge. *Bulletin of the American Meteorological Society*, 88(2):177–190, 2007. doi: 10.1175/BAMS-88-2-177.

M. H. Unsworth and J. L. Monteith. Long-wave radiation at the ground I. Angular distribution of incoming radiation. *Quarterly Journal of the Royal Meteorological Society*, 101(427):13–24, 1975. doi: 10.1002/qj.49710142703.

W. J. Van De Berg, M. R. Van Den Broeke, C. H. Reijmer, and E. Van Meijgaard. Characteristics of the antarctic surface mass balance, 1958–2002, using a regional atmospheric climate model. *Annals of Glaciology*, 41:97–104, 2005. doi: 10.3189/172756405781813302.

M. R. Van den Broeke. Strong equation melting preceded collapse of Antarctic Peninsula ice shelf. *Geophysical Research Letters*, 32(12), 2005. doi: 10.1029/2005GL023247.

M. R. Van Den Broeke, C. H. Reijmer, and R. S. W. Van De Wal. A study of the surface mass balance in dronning maud land, antarctica, using automatic weather station. *Journal of Glaciology*, 50(171):565–582, 2004. doi: 10.3189/172756504781829756.

M. R. Van Den Broeke, C. Reijmer, D. Van As, R. Van de Wal, and J. Oerlemans. Seasonal cycles of Antarctic surface energy balance from automatic weather stations. *Annals of Glaciology*, 41:131–139, 2005. doi: 10.3189/172756405781813168.

M. R. Van den Broeke, C. Reijmer, D. Van As, and W. Boot. Daily cycle of the surface energy balance in Antarctica and the influence of clouds. *International Journal of Climatology*, 26:1587–1605, 2006. doi: DOI:10.1002/joc.1323.

K. Van Tricht, S. Lhermitte, I. V. Gorodetskaya, and N. P. M. van Lipzig. Improving satellite-retrieved surface radiative fluxes in polar regions using a smart sampling approach. *The Cryosphere*, 10(5):2379–2397, 2016a. doi: 10.5194/tc-10-2379-2016.

K. Van Tricht, S. Lhermitte, J. T. M. Lenaerts, I. V. Gorodetskaya, T. S. L'Ecuyer, B. Noel, M. R. Van den Broeke, D. D. Turner, and N. P. M. van Lipzig. Clouds enhance Greenland ice sheet meltwater runoff. *Nature Communications*, 7:10266(10.1038/ncomms10266), 2016b.

J. M. Van Wessem, C. H. Reijmer, J. T. M. Lenaerts, W. J. Van de Berg, M. R. Van den Broeke, and E. Van Meijgaard. Updated cloud physics in a regional atmospheric climate model improves the modelled surface energy balance of Antarctica. *The Cryosphere*, 8(1):125–135, 2014. doi: 10.5194/tc-8-125-2014.

J. M. Van Wessem, W. J. van de Berg, B. P. Y. Noël, E. van Meijgaard, C. Amory, G. Birnbaum, C. L. Jakobs, K. Krüger, J. T. M. Lenaerts, S. Lhermitte, S. R. M. Ligtenberg, B. Medley, C. H. Reijmer, K. van Tricht, L. D. Trusel, L. H. van Ulft, B. Wouters, J. Wuite, and M. R. Van den Broeke. Modelling the climate and surface mass balance of polar ice sheets using RACMO2 – Part 2: Antarctica (1979–2016). *The Cryosphere*, 12(4): 1479–1498, 2018. doi: 10.5194/tc-12-1479-2018.

D.G. Vaughan, J.C. Comiso, I. Allison, J. Carrasco, G. Kaser, R. Kwok, P. Mote, T. Murray, F. Paul, J. Ren, E. Rignot, O. Solomina, K. Steffen, and T. Zhang. Observations: Cryosphere. In [T.F. Stocker, D. Qin, G.-K. Plattner, M. Tignor, S.K. Allen, J. Boschung, A. Nauels, Y. Xia, V. Bex, and P.M. Midgley], editors, *Climate Change 2013: The Physical Science Basis. Contribution of Working Group I to the Fifth Assessment Report of the Intergovernmental Panel on Climate Change*. Cambridge University Press, 2013.

P. Vellinga and S.P. Leatherman. Sea level rise, consequences and politics. *Climatic Change*, 15(175), March 1989. doi: https://doi.org/10.1007/BF00138851.

V. Vitale. Basic measurements of radiation at Concordia Station (2007-01 to 2010-02). Institute of Atmospheric Sciences and Climate of the Italian National Research Council, Bologna, PANGAEA, 2009, 2010. doi: 10.1594/PANGAEA.712070.

W. Wang, C.S. Zender, and D. van As. Temporal characteristics of cloud radiative effects on the greenland ice sheet: Discoveries from multiyear automatic weather station measurements. *Journal of Geophysical Research: Atmospheres*, 123(20):11,348–11,361, 2018. doi: 10.1029/2018JD028540.

D.M. Winker, M.A. Vaughan, A. Omar, Y. Hu, K.A. Powell, Z. Liu, W.H. Hunt, and S.A. Young. Overview of the CALIPSO Mission and CALIOP Data Processing Algorithms. *Journal of Atmospheric and Oceanic Technology*, 26(11):2310–2323, 2009. doi: 10.1175/2009JTECHA1281.1.

T. Yamanouchi. Basic and other measurements of radiation at station Syowa (2007-01-2010-03). National Institute of Polar Research, Tokyo, PANGAEA, 2010. doi: 10.1594/PANGAEA.740944.

C. Zwart. Significance of new-snow properties for snowcover development. Master's thesis, Institute for Marine and Atmospheric Research; University of Utrecht, the Netherlands, 2007.